Universität Hamburg
DER FORSCHUNG | DER LEHRE | DER BILDUNG

Metal-Semiconductor Nanohybrids for Solar-to-Fuel Conversion: A Systematic Study on the Processes Limiting the Photocatalytic Yield

Dissertation
zur Erlangung des Doktorgrades an der Fakultät für Mathematik, Informatik und Naturwissenschaften
(Dr. rer. nat.)

Fachbereich Chemie
Universität Hamburg

vorgelegt von

Sönke Wengler-Rust

Hamburg
Oktober 2024

Dissertation

Titel:	Metal-Semiconductor Nanohybrids for Solar-to-Fuel Conversion: A Systematic Study on the Processes Limiting the Photocatalytic Yield
Titel (deu.):	Metall-Halbleiter Nanohybride zur Umwandlung von Sonnenlicht zu Brennstoff: Eine systematische Studie über die Prozesse, welche die photokatalytische Ausbeute limitieren
Eingereicht von:	Sönke Wengler-Rust
Matrikelnummer:	6424647
Email:	soenke.wr@gmail.com
Arbeitsgruppe:	Prof. Dr. Horst Weller
Institut:	Institut für Physikalische Chemie
Universität:	Universität Hamburg
Datum der Einreichung:	11. Oktober 2024
Erstgutachter:	Prof. Dr. Horst Weller
Zweitgutachter:	Prof. Dr. Alf Mews
Datum der Disputation:	13. Dezember 2024
Prüfungskommission:	Prof. Dr. Horst Weller Prof. Dr. Gabriel Bester Priv. Doz. Dr. Christoph Wutz
Freigabe zur Veröffentlichung:	17. Januar 2025

Diese Arbeit wurde im Zeitraum von Mai 2020 bis Oktober 2024 in der Arbeitsgruppe von Prof. Dr. Horst Weller am Institut für Physikalische Chemie der Universität Hamburg angefertigt.

List of Publications

Journal Articles

- Soenke Wengler-Rust, Yannic U. Staechelin, Holger Lange, Horst Weller. Donor-Specific Surface Interactions Promote the Photocatalytic Activity of Metal-Semiconductor Nanohybrids. *Small* **2024**, *20*, 2401388.

Conference Contributions

- **2023 MRS Spring Meeting**, San Francisco, USA, April 2023.
  Oral presentation: "Scavenger-Dependent Hole Removal Dynamics in Pt-Tipped CdSe/CdS Dot-in-Rod Nanohybrids".
- **NANOHYBRID - Hamburg Conference on Complex Nanostructures**, Hamburg, October 2022.
  Poster: "Anisotropic Metal-Semiconductor Heterostructures for Photocatalytic H_2 Production".
- **Bad Honnef Physics School: Exciting Nanostructures**, Bad Honnef, July 2021.
  Poster: "Anisotropic (Metal-)Semiconductor Heterostructures as Functional Building Blocks and for Photocatalysis".

Contents

List of Abbreviations

BS - beam splitter
c - cubic
CB - conduction band
CLP Regulation - regulation "for Classification, Labeling and Packing"
CMR - carcinogenic, mutagenic, or reprotoxic
COD-DM-Pt - (1,5-cyclooctadiene)dimethylplatinum(II)
Coumarin 153 - 2,3,6,7-tetrahydro-9-trifluoromethyl-1H,5H-quinolizino(9,1-gh)-coumarin
CSS - charge-separated state
DCB - 1,2-dichlorobenzene
DPE - diphenyl ether
DR - dot-in-rod
EDA - electron donating agent
EtOH - ethanol
fs-TA measurement - TA measurement with a femtosecond resolution
FWHM - full width at half maximum
GC - gas chromatograph
GHS - Globally Harmonized System of Classification and Labelling of Chemicals
HAADF STEM - high-angle annular dark field scanning transmission electron microscopy
HDD - 1,2-hexadecanediol
HER - hydrogen evolution reaction
HOMO - highest occupied molecular orbital
HPA - n-hexylphosphonic acid
HRTEM - high resolution transmission electron microscopy
IPA - isopropyl alcohol
IRF - instrument response function
LCAO - linear combination of atomic orbitals
LUMO - lowest unoccupied molecular orbital
MeOH - methanol
MS - mass spectrometer

MSC - magic-sized cluster
MUA - 11-mercaptoundecanoic acid
NC - nanocrystal
NFE - nearly free electron
NP - nanoparticle
NPL - nanoplatelet
NR - nanorod
ns-TA measurement - TA measurement with a nano- to microsecond resolution
OA - oleic acid
OAm - oleylamine
ODPA - n-octadecylphosphonic acid
OPA - optical parametric amplifier
PDF - *The Powder Diffraction File*
PL - photoluminescence
ppm - parts-per-million
QD - quantum dot
RT - room temperature
SHG - second harmonic generation
STH - surface-trapped hole
TAC - time-to-amplitude converter
TCSPC - time-correlated single-photon counting
TEM - transmission electron microscopy
TOP - trioctylphosphine
TOPO - trioctylphosphine oxide
UV - ultraviolet
UV-vis - ultraviolet-visible
VB - valence band
w - wurtzite
XRD - X-ray diffraction
zb - zinc blende

1 Abstract

Colloidal semiconductor-metal nanostructures can be used as photocatalysts for generating hydrogen from water. The use of nanostructures is especially promising due to their large surface-area-to-volume ratio, providing a large catalytically active surface area with small amounts of material. Additionally, due to their synthetically adjustable optoelectronic properties and composition, these nanostructures can serve as model systems for studying the efficiency-limiting parameters of the solar-to-fuel conversion processes. Literature agrees that the photocatalytic activity of the nanostructures critically relies on the separation of the photogenerated charge carriers, which can be altered by tuning the dimensionality and composition of the nanoparticles or by inducing charge scavenging and trapping processes. However, processes occurring at the nanoparticles' surface were only partly considered in the present discussion, *e.g.* electron donating agent-specific surface interactions have not been addressed so far.

To assess the impact of the various parameters limiting the photocatalytic yield, a systematic study was carried out, which correlates the charge carrier dynamics within 11-mercaptoundecanoic acid-capped, Pt-tipped CdSe/CdS dot-in-rods with their photocatalytic activity and colloidal stability. The charge carrier dynamics and photocatalytic activity of the nanoparticles were investigated in parameter studies by conducting transient absorption and time-resolved photoluminescence spectroscopy, as well as steady-state hydrogen production measurements. These measurements were combined with electron microscopy, dynamic light scattering, and static spectroscopy to examine the colloidal stability of the nanoparticles.

Based on this large set of measurements, the study reveals that the photocatalytic activity is critically dependent on processes occurring at the nanoparticles' surface. It was found that electron donating agents interact differently with the nanoparticles' surface, and the two distinct groups of surface-active and diffusion-limited electron donating agents were identified. Besides these electron donating agent-specific surface interactions, the degree of surface passivation by ligands was observed to influence the nanoparticles' photocatalytic activity. The largest photocatalytic activities were determined for nanoparticle agglomerates, forming

upon ligand loss or induced by the presence of surface-active electron donating agents. These results indicate that the agglomeration of nanoparticles does not necessarily diminish the photocatalytic activity due to a loss of accessible surface area but instead may increase it by enabling charge transfer within the formed network. Combining these insights into the processes occurring at the nanoparticles' surface with a detailed acquisition of the synthesis parameters for obtaining Pt-CdSe/CdS nanoparticles with functional components of distinct number and dimensionality, this study enables to produce tailored nanohybrids functioning as building blocks for assembling structured and highly efficient catalyst networks.

2 Zusammenfassung

Kolloidale Halbleiter-Metall Nanostrukturen können als Photokatalysatoren zur Gewinnung von Wasserstoff aus Wasser genutzt werden. Die Verwendung von Nanostrukturen ist besonders vielversprechend, da diese aufgrund ihres großen Oberfläche-zu-Volumen-Verhältnisses eine große, katalytisch aktive Oberfläche bei geringen Mengen an Material aufweisen. Außerdem können die Nanostrukturen durch ihre synthetisch einstellbaren optoelektronischen Eigenschaften und Zusammensetzungen als Modellsysteme zur Untersuchung der Parameter dienen, welche die Effizienz der photokatalytischen Wasserstoffgewinnung limitieren. Die Literatur stimmt darin überein, dass die photokatalytische Aktivität der Nanostrukturen maßgeblich von der Trennung der photogenerierten Ladungsträger abhängt, welche durch Anpassung der Dimensionalität und Zusammensetzung der Nanopartikel oder durch verschiedene Ladungsabfangprozesse beeinflusst werden kann. Allerdings wurden Prozesse, welche an der Oberfläche der Nanopartikel auftreten, in der aktuellen Diskussion bisher nur teilweise berücksichtigt. Beispielsweise wurden die spezifischen Oberflächeninteraktionen verschiedener Elektronendonatoren bisher nicht thematisiert.
Um den Einfluss der zahlreichen Faktoren zu bewerten, welche die photokatalytische Aktivität beeinflussen, wurde eine systematische Studie durchgeführt. Die Studie korreliert die Ladungsträgerdynamiken in CdSe/CdS "Dot-in-rod" Nanopartikeln, welche mit einer Pt-Spitze versehen und durch 11-Mercaptoundecansäure passiviert sind, mit ihrer photokatalytischen Aktivität und kolloidalen Stabilität. Die Ladungsträgerdynamiken und photokatalytische Aktivität wurden in Parameterstudien untersucht, indem Transiente Absorptions- und zeitaufgelöste Photolumineszenzspektroskopie, sowie stationäre Wasserstoffproduktionsmessungen durchgeführt wurden. Diese Messungen wurden mit Elektronenmikroskopie, dynamischer Lichtstreuung und stationärer Spektroskopie zur Überprüfung der kolloidalen Stabilität kombiniert.
Basierend auf diesem großen und vielseitigen Datensatz zeigt die Studie, dass die photokatalytische Aktivität maßgeblich durch Prozesse limitiert ist, welche an der Oberfläche der Nanopartikel stattfinden. So wurde festgestellt, dass die Elektronendonatoren unterschiedlich mit der Oberfläche der Nanopartikel inter-

agieren und die beiden Gruppen von diffusionskontrollierten und oberflächenaktiven Elektronendonatoren wurden identifiziert. Außerdem wurde beobachtet, dass neben diesen spezifischen Oberflächeninteraktionen der Elektronendonatoren der Grad der Oberflächenpassivierung durch Liganden die photokatalytische Aktivität der Nanopartikel beeinflusst. Die größte photokatalytische Aktivität wurde für Agglomerate aus Nanopartikeln bestimmt, welche sich durch den Verlust von Liganden oder induziert durch die Gegenwart der oberflächenaktiven Elektronendonatoren bilden. Diese Ergebnisse zeigen, dass die Agglomeration von Nanopartikeln nicht zwangsläufig zu einer Verringerung der photokatalytischen Aktivität führt, aufgrund der Verkleinerung der zugänglichen Oberfläche. Stattdessen kann sich die Aktivität sogar erhöhen, da ein Ladungstransfer innerhalb des entstandenen Netzwerks ermöglicht wird. Indem diese Studie diese Erkenntnisse über die Oberflächenprozesse mit einer detaillierten Erfassung der Parameter zur Synthese von Pt-CdSe/CdS Nanopartikeln mit funktionellen Komponenten gewünschter Anzahl und Größe kombiniert, ermöglicht sie die Produktion von maßgeschneiderten Nanohybriden, welche als Bausteine zur Erstellung von strukturierten und hocheffizienten Katalysatornetzwerken dienen können.

3 Introduction

In a finite world, a sustainable economy is needed to permanently satisfy the world's growing energy demands. On the path of this fundamental transformation, molecular hydrogen is considered a key component, functioning as an energy storage media, energy vector, and fuel.[1–3] However, since hydrogen is typically a secondary energy carrier, it is essential that the energy for generating the hydrogen gas originates from renewable primary energy carriers like wind, sun, or hydropower for obtaining so-called "green hydrogen".[2;3] In most conventional procedures, electricity is produced from these renewable sources first, which is subsequently used for generating hydrogen. Avoiding the detour *via* electricity, the use of photocatalytic systems, which exploit the energy of sunlight for splitting water and thus generate hydrogen directly, is particularly promising.[4]

Colloidal multi-component nanoparticles (NPs) are especially interesting for photocatalytic applications, as was already stated in early publications on NPs.[5;6] NPs are solid particles with one or more dimensions in the size range of 1 to 100 nm.[7] Research on NPs started in the 1980s with the fundamental works of Ekimov, Brus, and Efros and was continued by Weller, Bawendi, Alivisatos, and others in the following decades.[5;6;8–13] Nowadays, a large body of synthesis procedures allows to produce colloidal NPs of various compositions, sizes, and shapes, combining a large surface-area-to-volume ratio with size-dependent optoelectronic properties. Due to these unique properties, NPs are used in a wide range of fields of application, including optoelectronics,[14–16] catalysis,[17–19] and biomedical applications.[20;21] The importance of the field of research was underlined by the awarding of the Nobel Prize in Chemistry "for the discovery and synthesis of quantum dots", which are fluorescent semiconductor NPs, to Ekimov, Brus, and Bawendi in 2023.[22]

While studying multi-component nanostructures of various shapes and compositions for photocatalytic applications, it was found that efficient charge separation is crucial for obtaining large photocatalytic yields.[23;24] Complex, anisotropic nanostructures combining different materials, like Pt-tipped CdSe/CdS dot-in-rods (DRs), were designed for spatially separating the photogenerated charges

within the NP.[24;25] The influence of the number and dimensionality of the functional components of these nanohybrids (core size, rod length, number and size of metal tips) on the photocatalytic yield was investigated in literature studies.[26–33] Additionally, the photocatalytic yield was found to be strongly dependent on the presence of electron donating agents (EDAs), which scavenge the photogenerated holes from the semiconductor domain.[27;32;34–36] In the presence of alcoholic EDAs at very high pH, photocatalytic yields near unity were obtained, which was ascribed to a "hole shuttle mechanism" enabled by the large concentration of hydroxide anions.[32;34] Based on the strong influence of the EDA on the photocatalytic yield, the hole transfer onto the EDA was identified as the efficiency-limiting step of the overall solar-to-fuel conversion process.[34;37;38] In light of these numerous studies and given the versatility of tunable parameters, colloidal semiconductor-metal NPs may serve as highly efficient catalysts, as well as simple but solid model systems for studying the parameters limiting the efficiency of photocatalytic systems in general.

4 Theory

4.1 Synthesis of Colloidal Nanoparticles

Colloidal NPs can be obtained conveniently and in a reproducible manner *via* liquid-phase synthesis. Various synthesis protocols exist, allowing to produce NPs of tailored sizes, shapes, and compositions, while maintaining a small size distribution.[6;39;40] Colloidal NPs can easily be dispersed in a variety of organic or aqueous solvents. The process of nucleation and growth of the NPs can be described schematically by the LaMer model.[41] This model separates the process into three stages (**Figure 4.1**). In the first stage (I), free monomers are formed,

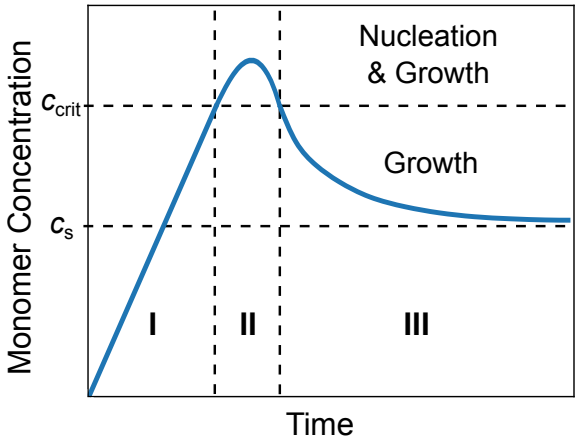

Figure 4.1: Schematic of the three stages (I-III) of nucleation and growth of NPs in the LaMer model. Firstly, free monomers are formed (stage I). Stable nuclei form after the concentration of free monomer exceeds the critical nucleation concentration c_{crit}, resulting in a decrease of the monomer concentration (stage II). Once the latter falls below c_{crit}, the NPs grow exclusively (stage III). The growth proceeds, while the monomer concentration is above the saturation concentration c_s. Figure modified from LaMer *et al.*[41]

either by chemical reaction or thermal decomposition of the precursors. After exceeding the critical nucleation concentration c_{crit}, the monomers undergo a "burst-nucleation" (stage II), which rapidly reduces the monomer concentration.[42] As the concentration of free monomer falls below c_{crit}, nucleation stops,

and the NPs start to grow (stage III). The growth of the formed nuclei is controlled by the diffusion of the monomers and will proceed while the monomer concentration is above the saturation concentration c_s.[42] Due to the energy needed to create a new surface, the growth of existing nuclei is energetically favored over the formation of new ones. The change in the Gibbs free energy ΔG by the formation of a spherical nucleus of radius r can be expressed as

$$\Delta G = 4\pi r^2 \gamma + \frac{4}{3}\pi r^3 \Delta G_V, \tag{4.1}$$

with the surface free energy γ and the free energy per volume ΔG_V.[43] The latter is defined as

$$\Delta G_V = -\frac{k_B T \ln(S)}{V}, \tag{4.2}$$

with the Boltzmann's constant k_B, temperature T, the supersaturation S, and the volume of an atom in the NP V.[42] The radius-dependent surface, volume, and total free energy from Equation (4.1) are plotted schematically in **Figure 4.2**. The free energy decreases for NP radii larger than the critical radius r_{crit}. Therefore, nuclei of radii smaller r_{crit} will dissolve, whereas nuclei of radii larger r_{crit} are stable in suspension and continue to grow.[42] The critical radius can be calculated considering that $\frac{d\Delta G}{dr} = 0$ for $r = r_{crit}$

$$r_{crit} = -\frac{2\gamma}{\Delta G_V} = \frac{2\gamma V}{k_B T \ln(S)} \tag{4.3}$$

and the corresponding critical free energy ΔG_{crit} is

$$\Delta G_{crit} = \frac{16}{3}\pi \frac{\gamma^3}{\Delta G_V^2} = \frac{4}{3}\pi \gamma r_{crit}^2. \tag{4.4}$$

This critical free energy corresponds to the energy barrier the nucleation process must overcome to form stable NPs in suspension. This energy barrier depends on the experimental parameters supersaturation, temperature, and surface free energy (*cf.* Equation (4.4) and Equation (4.2)).[43;44] Therefore, nucleation occurs only at monomer concentrations larger c_{crit}, at sufficiently large temperatures, and in the presence of suitable surfactants, which reduce the surface free energy.[42] In order to guarantee a narrow NP size distribution, the nucleation phase should be short, which is typically implemented by a rapid injection of one precursor into the reaction solution.[11;45] During the growth phase of the NPs, the monomer concentration gradually decreases, causing the critical radius to increase (*cf.* Equation (4.3)). Therefore, small NPs will dissolve, while large

NPs grow, a process called "Ostwald ripening".[46] Depending on the synthesis parameters, this process can lead to a focusing or defocusing of the NPs' size distribution.[47]

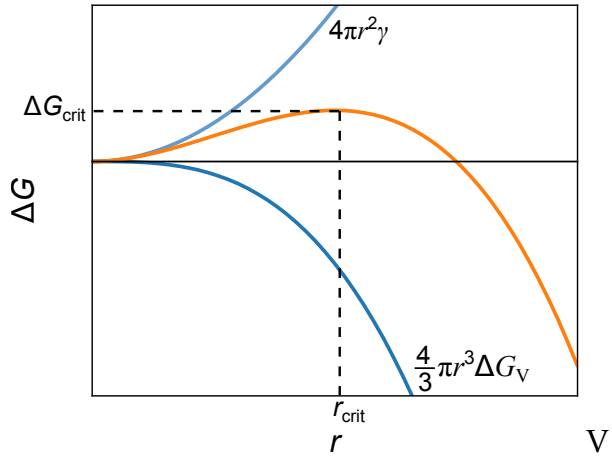

Figure 4.2: Schematic plot of the total free energy ΔG (orange line), with a positive surface contribution (light blue line) and a negative volume contribution (dark blue line), against the NP radius r. A critical free energy ΔG_{crit} is needed for forming stable nuclei of a radius r_{crit} and larger. Figure modified from Finke *et al.*,[48] used under *Creative Commons CC-BY* license.

However, not all NP synthesis procedures aim for a homogeneous nucleation. In "seeded growth" methods, a second material is deposited onto previously synthesized NPs, which function as seeds for nucleation. This heterogeneous nucleation is implemented at milder reaction conditions (lower temperature and supersaturation) to inhibit homogeneous nucleation of the shell material.[49]

4.2 Energetic Structure of Semiconductors

4.2.1 Band Structure

The electronic band structure describes the energetic states in crystalline solids. The band structure can be calculated using quantum mechanical models like the "nearly free electron" (NFE) or the "tight binding" model. The NFE model is based on delocalized electrons that can move almost freely through the crystal lattice. This makes it a suitable approach for describing metals with strongly delocalized electrons.[50] The energetic states are derived from the interactions of the electrons with the periodic core potentials.[51;52] The tight binding model is a bottom-up approach that assumes localized atoms and calculates the band structure from the linear combination of their binding and anti-binding orbitals, which is also

known as the "linear combination of atomic orbitals" (LCAO) method.[50;53] With an increasing number of atoms, more energy states are introduced, eventually resulting in continuous energy bands. **Figure 4.3** illustrates this transition for semiconductor materials: while molecules exhibit discrete energy levels, semiconductor nanocrystals (NCs) show bands of quantized and size-dependent energy levels, and semiconductor bulk materials feature continuous energy bands. Analogous to the highest occupied molecular orbital (HOMO) and the lowest unoccupied molecular orbital (LUMO) of the molecule, the valence band (VB) is completely filled, whereas the conduction band (CB) is unoccupied by electrons, in an undoped semiconductor at 0 K.[5] The VB and CB are separated by a band gap of an energy E_g, which is crystal size-dependent for nanometer-sized crystals.

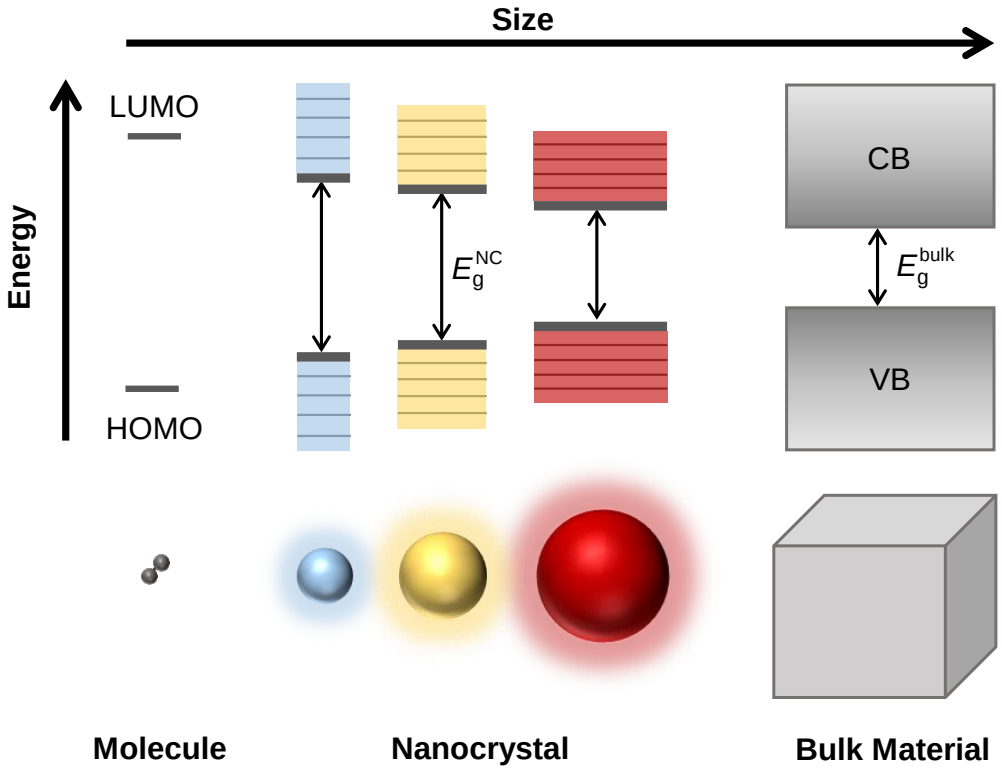

Figure 4.3: Scheme illustrating the energetic states in semiconductors of different size. While molecules exhibit discrete energy levels, bulk material shows continuous energy bands. NCs can be categorized between molecules and bulk material as they exhibit energy bands with discrete energy levels. The VB and CB are separated by a band gap of energy E_g^{bulk} for the bulk and a size-dependent energy E_g^{NC} for the NCs. Figure modified from de Mello Donegá,[54] © 2011 *The Royal Society of Chemistry*, used with permission.

4.2.2 Quantum Confinement in Nanoparticles

In semiconductor NCs, the absorption of light of an energy larger than the band gap can excite an electron from the VB into the CB, creating a hole in the VB. The electron in the CB and the hole in the VB are bound by Coulomb attraction. The resulting bound electron-hole pair is called an exciton (**Figure 4.4**). The size of an exciton can be calculated analogously to the Bohr radius of a hydrogen atom.[55]

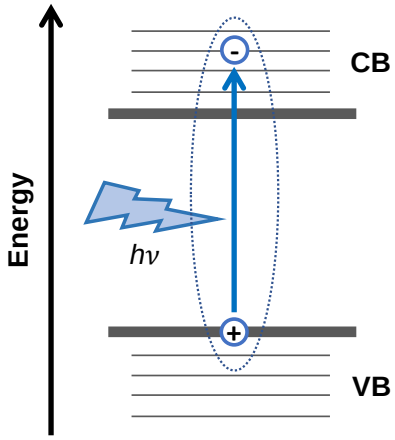

Figure 4.4: Scheme illustrating the formation of an exciton. The absorption of a photon with an energy larger than the band gap excites an electron from the VB into the CB, creating a hole in the VB. Electron and hole form a bound electron-hole pair, an exciton (indicated by the dashed line).

In contrast to the hydrogen atom, where the electron is much lighter than the proton, the exciton's electron and hole have comparable masses. Therefore, the effective masses of both charge carriers must be considered when calculating the exciton Bohr radius a_0

$$a_0 = \frac{4\pi\varepsilon\hbar^2}{e^2}\left(\frac{1}{m_e} + \frac{1}{m_h}\right), \tag{4.5}$$

with the permittivity at optical frequencies ε, the reduced Planck constant $\hbar$, the electron charge e, and the effective masses of the electron m_e and hole m_h. Thus, the electron and hole of the exciton maintain a material-dependent preferred distance in the crystal (*e.g.* 5.6 nm for CdSe or 2.8 nm for CdS).[56;57] If the radius of the NC is of the same order of magnitude as the exciton radius, the exciton is restricted in its movement. This phenomenon is called weak quantum confinement. Strong confinement occurs when the radius of the NC is smaller than that of the exciton.[58] The exciton's confinement in the NC causes a change in the density of electronic states, leading to discrete energy states and a NC size-dependent band gap energy (*cf.* Figure 4.3).[13;58] The size-dependent energetic

states of the NC can be described by the particle-in-a-box model known from elementary quantum mechanics.[13;59] The Brus formula can be applied to calculate the lowest energy eigenvalue of the NC system, which corresponds to the band gap energy of the NC E_g^{NC}

$$E_g^{NC} = E_g^{bulk} + E_{conf} - E_C = E_g^{bulk} + \frac{\hbar^2\pi^2}{2r^2}\left(\frac{1}{m_e} + \frac{1}{m_h}\right) - \frac{1.8e^2}{\varepsilon r}, \qquad (4.6)$$

where E_g^{bulk} is the band gap energy of the bulk material, E_{conf} the confinement and E_C the Coulomb energy.[60] For small radii, the contribution of the confinement term dominates over the Coulomb-term, resulting in an increase of the band gap energy for decreasing NC sizes.[60;61]

4.2.3 Anisotropic NPs

Besides spherical quantum dots (QDs), semiconductor NPs of anisotropic morphologies can also be obtained using well-established liquid-phase syntheses.[40] The growth of the semiconductor domain can be restricted to selected dimensions by using specific synthesis conditions and ligands, resulting in the formation of NPs of various complex shapes like nanorods (NRs),[12;49] tetrapods,[62] or nanoplatelets (NPLs; see Section 4.5.1 for detailed description on the mechanisms, which provoke anisotropic growth).[63] The band gap of the obtained anisotropic NPs is primarily determined by the size of the dimension(s) exerting the strongest quantum confinement on the exciton (**Figure 4.5**). Therefore, in the case of 1D NRs, the band gap energy is mainly governed by the NR's width. Analogously, the band gap energy of 2D NPLs is dictated by their thickness, which can be precisely adjusted to individual monolayers.[64]

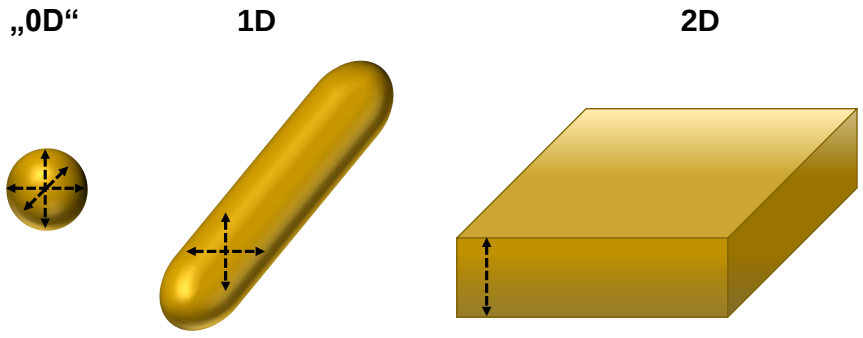

Figure 4.5: Scheme of a "0D" QD, a 1D NR and a 2D NPL. The dashed arrows indicate the dimensions of the strongest quantum confinement.

However, the band gap energy is not completely independent of the size(s) of the extended dimension(s). For example, for semiconductor NRs, it was found that especially in the strong confinement regime, *i.e.* for small NR widths, the length of the NR likewise strongly influences the band gap energy.[58]

4.2.4 Semiconductor Heterostructures

By combining two or more different semiconductor materials in one NP, heterojunctions are formed between the materials. Wet-chemical synthesis allows to create complex heteronanocrystals whose band alignment and optical properties can be tailored to specific applications. Depending on the materials used, a direct, straddling band gap (type I), or a staggered band gap (type II) can be obtained (**Figure 4.6**).[51;59;65;66] In a type I system, the quantum wells of the VB and CB are

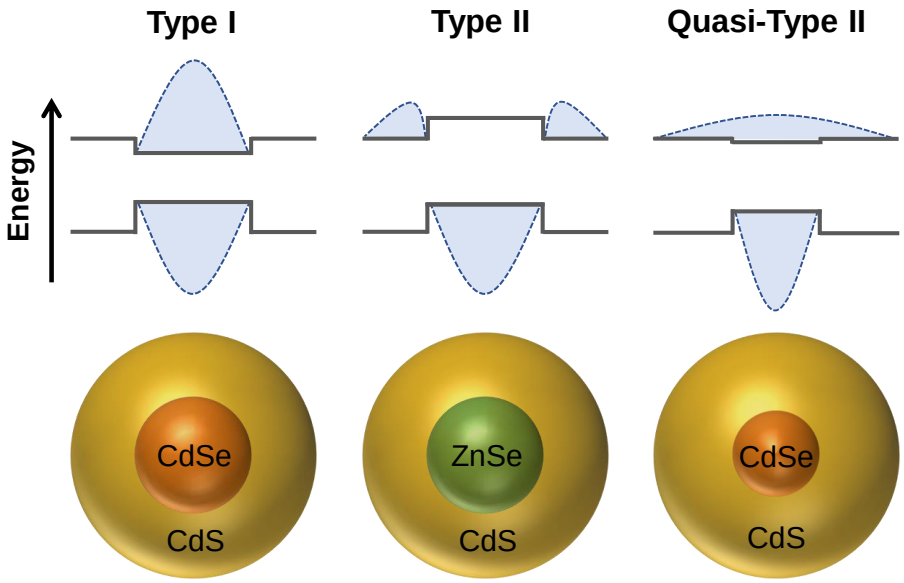

Figure 4.6: Illustration of three types of semiconductor heterostructures. A type I, type II, and quasi-type II band alignment arises, depending on the semiconductor materials and domain size of the core-shell NPs. Based on the relative position of the quantum wells, photogenerated electrons and holes localize into the same or different domains. The dashed lines and blue areas indicate the electron and hole wave functions.[59]

located in the same material domain. Hence, all photogenerated charge carriers localize into this domain. As the charge carriers accumulate inside the NP, distant from defect sites, dangling bonds, and other trap states at the NP's surface, type I core-shell heterosystems typically exhibit high photoluminescence (PL) quantum yields (see Section 4.3 for details on PL from semiconductor NPs).[67–71] In

a type II system, the quantum wells in VB and CB are in different material domains, causing the photogenerated electrons and holes to transfer into different domains. If one of the quantum wells is small, *i.e.* a small band offset is present between the two semiconductor domains, the respective charge carrier can delocalize over the whole material, while the second charge carrier is localized in one domain (quasi-type II). Since the band gap energy depends on the size of the domain, classical type I systems can transition into quasi-type II potential profiles at certain domain sizes (*e.g.* transition at a core size $< 2.8\,\mathrm{nm}$ from type I to quasi-type II for CdSe/CdS core-shell NPs).[72–74] Due to the spatial separation of the charge carriers, type II and quasi-type II heterosystems are well-suited for catalytic or photovoltaic applications in which the recombination rate should be minimized.[24;65;75;76]

4.3 Photoluminescence

Photoluminescence is the emission of light by a substance after excitation by light. It is divided into the two processes of fluorescence and phosphorescence. Both processes differ in their emission rates and nature of the excited state.[77;78] Phosphorescence does not typically occur in colloidal NP suspensions at room temperature (RT) due to numerous non-radiative decay channels.[77] The PL processes described below are therefore exclusively fluorescence processes.

As indicated above, the absorption of light can excite an exciton in semiconductor crystals. After fast, non-radiative, vibrational relaxation to the ground state of the CB, the electron recombines with the hole at the VB, leading to the emission of a photon (*cf.* **Figure 4.7**; non-radiative relaxation to the ground state typically within femto- to picoseconds).[77;78] Due to the preceding non-radiative relaxation, the emitted photon has less energy than the absorbed photon. The resulting bathochromic shift from emission to absorption is called Stokes shift.[77] The energy of the emitted photon is primarily determined by the band gap of the NC and therefore the size of the crystal. In heterostructures with a type I potential profile, the energy of the emitted photon is determined by the component with the smallest band gap (typically the core component). In actual NC samples, the PL and absorption features are broadened by thermal effects and due to NP size distribution.[79] However, the exciton does not necessarily recombine radiatively, but the electron might relax back into the VB *via* numerous non-radiative channels. The photoluminescence quantum yield (QY_{PL}) characterizes the proportion of radiative recombinations that occur in a fluorophore. It is defined as the ratio of the number of emitted N_{em} and the number of absorbed photons N_{abs} and there-

fore can also be expressed using the respective rate constants for the radiative k_{rad} and non-radiative $k_{\text{non-rad}}$ exciton decay.[77;80]

$$QY_{\text{PL}} = \frac{N_{\text{em}}}{N_{\text{abs}}} \cdot 100\,\% = \frac{k_{\text{rad}}}{k_{\text{rad}} + k_{\text{non-rad}}} \cdot 100\,\% \tag{4.7}$$

The non-radiative rate constant $k_{\text{non-rad}}$ summarizes various pathways of non-radiative recombination like energy dissipation *via* Auger recombination, charge carrier trapping into defect states, or use of the photogenerated charge carriers for chemical reactions, which are discussed in more detail later.

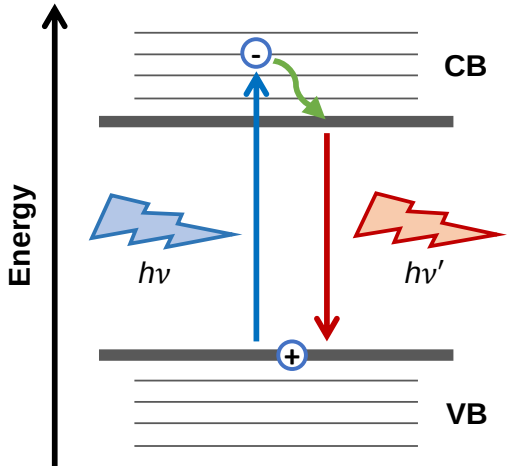

Figure 4.7: Scheme illustrating the PL process in semiconductor NCs. The absorption of a photon with an energy of $h\nu$ excites an electron from the VB into the CB of the NC, creating a hole in the VB (blue arrow). The electron relaxes non-radiatively to the ground state of the CB (green, curved arrow). Electron and hole eventually recombine, causing the emission of a photon with an energy of $h\nu'$ (red arrow).

4.3.1 Photoluminescence Lifetime

Upon excitation of a fluorophore, the relaxation of the excited state is a first order process, which is therefore proportional to the occupation of this state N_{exc} and determined by rate constants for the radiative and non-radiative recombination.[77;78;80]

$$-\frac{\mathrm{d}N_{\text{exc}}(t)}{\mathrm{d}t} = N_{\text{exc}}(t) \cdot (k_{\text{rad}} + k_{\text{non-rad}}) \tag{4.8}$$

This differential equation can be solved by

$$N_{\text{exc}}(t) = N_{\text{exc}}^{0} \cdot e^{-(k_{\text{rad}} + k_{\text{non-rad}}) \cdot t}, \tag{4.9}$$

with the initial occupation of the excited state N^0_{exc}. The PL lifetime τ_{PL} is defined as the average time the fluorophore remains in the excited state before returning to the ground state by electron-hole recombination.[77] Since the rate constants k_{rad} and $k_{\text{non-rad}}$ depopulate the excited state, the PL lifetime can be expressed as

$$\tau_{\text{PL}} = \frac{1}{k_{\text{PL}}} = \frac{1}{k_{\text{rad}} + k_{\text{non-rad}}}, \tag{4.10}$$

with the rate constant of the PL decay k_{PL}.[77;78;80] Equation (4.9) can therefore be formulated as

$$N_{\text{exc}}(t) = N^0_{\text{exc}} \cdot e^{-\frac{t}{\tau_{\text{PL}}}}. \tag{4.11}$$

Thus, the PL lifetime is the time needed for the occupation of the excited state to decay to e^{-1} of the initial occupation

$$N_{\text{exc}}(\tau_{\text{PL}}) = \frac{N^0_{\text{exc}}}{e}. \tag{4.12}$$

If the non-radiative decay channels compete with the radiative decay channels, they reduce the PL lifetime of the fluorophore.[77]

4.3.2 Photoluminescence Quenching

The PL intensity of a fluorophore can be diminished by various processes, which are referred to as quenching. These processes can be desired, *e.g.* to enable chemical reactions, or detrimental in optical applications, aiming for a maximal QY_{PL}. If the quenching results from the interaction with another NP or molecule, the latter is referred to as a quencher. The interaction between the quencher and fluorophore can be either static or dynamic.[77;80]

Static Quenching

In the process of static quenching, fluorophore and quencher form a non-fluorecent complex. Therefore, the number of fluorescent fluorophores is reduced by the quencher, resulting in a reduction of the sample's PL intensity, while the PL lifetime is constant

$$\frac{\tau_{\text{PL},0}}{\tau_{\text{PL}}} = 1, \tag{4.13}$$

with the lifetimes of the fluorophore $\tau_{\text{PL},0}$ and τ_{PL} in the absence and presence of the quencher, respectively. The quencher-dependent fluorescence can be de-

scribed by the Stern-Volmer equation

$$\frac{F_0}{F} = \frac{QY_{PL,0}}{QY_{PL}} = \frac{[F_0]}{[F]} = 1 + K_S \cdot [Q]. \tag{4.14}$$

In this equation, F_0 and F are the fluorescence intensities, $QY_{PL,0}$ and QY_{PL} the PL quantum yields, and $[F_0]$ and $[F]$ the concentrations of the fluorophore in the absence and presence of the quencher, respectively. K_S is the equilibrium constant of the complex formation and $[Q]$ is the concentration of the quencher.[77] The relations in Equation (4.13) and Equation (4.14) can be plotted in a Stern-Volmer plot (**Figure 4.8**a).

Dynamic Quenching

In dynamic or collisional quenching, the fluorophore and quencher do not form a stable complex, but the quencher must diffuse to the fluorophore in order to deactivate it. The excited fluorophore is deactivated only upon contact with the quencher within the timeframe of the PL lifetime.[77] In dynamic quenching, the fluorescence intensity and the lifetime are diminished equivalently in the presence of the quencher

$$\frac{F_0}{F} = \frac{\tau_{PL,0}}{\tau_{PL}} = 1 + K_D \cdot [Q], \tag{4.15}$$

with the rate constant of dynamic quenching K_D (see Stern-Volmer plot in Figure 4.8b).[77;78;80] As dynamic quenching by collision with the quencher represents another non-radiative decay channel, the PL lifetime (Equation (4.10)) can be calculated as follows

$$\tau_{PL} = \frac{1}{k_{rad} + k_{non\text{-}rad} + k_Q \cdot [Q]}, \tag{4.16}$$

with the quenching rate constant k_Q.[77]

Combination of Static and Dynamic Quenching

Dynamic and static quenching can also occur simultaneously for the same quencher. Both processes are combined in the Stern-Volmer equation

$$\frac{F_0}{F} = (1 + K_D \cdot [Q])(1 + K_S \cdot [Q]). \tag{4.17}$$

Accordingly, the Stern-Volmer plot is not linear but exhibits an upward curvature (Figure 4.8c).[77] As the lifetime is only influenced by dynamic quenching, the product of $\tau_{PL,0} \cdot \tau_{PL}^{-1}$ can be expressed by Equation (4.15).

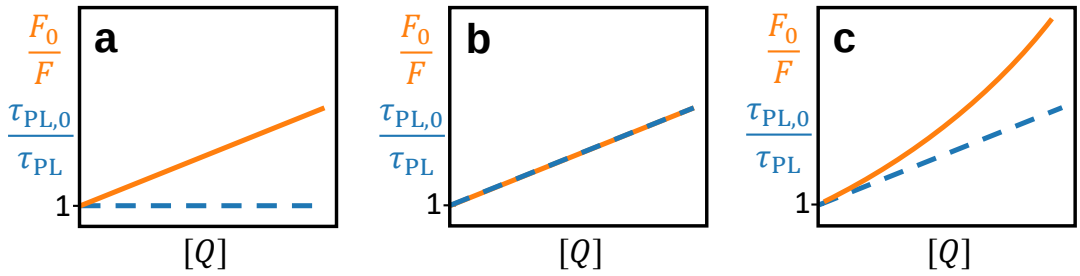

Figure 4.8: Schematic of the Stern-Volmer plot for static (a), dynamic (b), and a combination of static and dynamic quenching (c).

4.4 Nanophotocatalysts

In addition to optical applications, the photogenerated charge carriers in semiconductor NPs can also be employed to run redox reactions like hydrogen and oxygen generation by water splitting or carbon dioxide reduction.[32;81–84] The energy of the photogenerated charge carriers and therefore the band gap energy of the employed semiconductor must be large enough to drive the respective reaction. Due to its matching band alignment, CdS is ideally suited for the photolysis of water, while being excitable by visible light.[85–88] To achieve large hydrogen production rates, the charge recombination rate has to be minimized, as it competes directly with the photocatalytic use of the charge carriers.[31;89] Therefore, electron and hole need to be separated effectively. In a CdSe/CdS core shell system, the CdSe core functions as a hole acceptor. If a metal domain is deposited on the semiconductor, the metal functions as an electron acceptor. Various liquid-phase syntheses enable the deposition of metal domains of desired material, number, and size onto semiconductor NPs (see below for details on deposition methods).[86;90–93] The use of Pt is especially advantageous as it catalyzes the hydrogen production by reducing the overpotential of the hydrogen evolution reaction (HER).[34;94;95] Hydrogen evolution is enabled by the upward shift of the Fermi level of the nanoscopic Pt domain caused by the accumulation of photogenerated electrons.[96–99] To further improve the charge separation between the electron at the Pt photocathode and the hole at the CdSe core, an elongated CdS domain can be applied. The hydrogen production rate was found to generally rise with increasing length of the CdS rod domain due to better charge separation and an increased absorption cross section. However, as the number of trap states as well as the average distance charge carriers have to cover to reach the Pt domain or CdSe core increases with the length of the rod, the ideal length was found to be of a several tens of nanometers.[32;100–102] In the resulting Pt-CdSe/CdS nanohybrid, the photogenerated charge carriers are separated

by the length of the CdS rod-domain and three different inorganic components. The size, number, and position of the metal domains were also found to have a large influence on the photocatalytic activity.[27–30] The largest activity was obtained by depositing a single Pt domain on the DR's tip opposing the CdSe core (**Figure 4.9**). This increase in activity was attributed to improved spatial charge separation and the concentration of all reduction processes at one specific site compared to NPs with different domain locations or multiple metal domains, respectively.[27;28] Furthermore, it was demonstrated that the photocatalytic activity is inversely correlated with the CdSe core size, as it affects the localization of the charge carriers.[26;31;32]

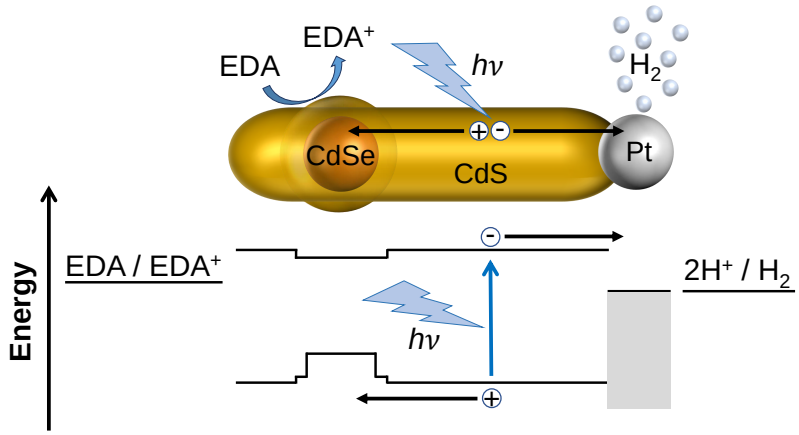

Figure 4.9: Scheme of a Pt-tipped CdSe/CdS DR and the related simplified energy level diagram, illustrating the separation of photogenerated charge carriers, hydrogen evolution and hole scavenging by the EDA. The CdSe core is surrounded by a CdS bulb, resulting in a smaller band gap energy than the rest of the CdS domain. The Pt tip functions as a photocathode and co-catalyst, catalyzing hydrogen production. Figure modified from Wengler-Rust *et al.*,[103] used under *Creative Commons CC-BY* license.

In principle, the photogenerated holes could be used for water oxidation in Pt-CdSe/CdS photocatalysts. However, since the generation of an oxygen molecule from water requires the transfer of four electrons ($2H_2O \rightarrow O_2 + 4H^+ + 4e^-$), it is inevitable to proceed *via* oxidized intermediates.[95] Therefore, suitable oxidation co-catalysts are needed.[104;105] Concurrently, the oxygen evolution reaction competes with the loss of photogenerated holes resulting from charge recombination and oxidation of the semiconductor domain or ligand at the NP's surface.[34;106] Additionally, the generated oxygen can function as an electron acceptor, reducing the efficiency in hydrogen production, or may react back to water.[36;107] At present, only a few reports state complete water-splitting, generating hydrogen

and oxygen while using nanohybrids, and the efficiencies achieved are relatively low.[75;95]

To prevent the nanocatalyst from gradual degradation and achieve large and stable efficiencies in hydrogen production, the photogenerated holes have to be removed efficiently from the NP. This is typically implemented by adding sacrificial EDAs to the NPs' suspension. The present literature provides a whole library of suitable EDAs, including various alcohols and amines, as well as sulfides, sulfites, and hydroxides.[27;32;34–36;108] As sulfides and sulfites are a by-product of petrochemical industries, the use as EDAs might additionally contribute to solving environmental issues.[109] Furthermore, many organic compounds can eventually be decomposed to CO_2 through multiple oxidation steps (*e.g.* MeOH can be photooxidized to CO_2 *via* the stable intermediates formaldehyde and formic acid).[36;110] In a pursuing "waste-to-energy" study, it was found that even polymeric compounds can be decomposed by using them as EDAs.[111] The oxidation of the EDA typically proceeds *via* a kinetically favored one-electron transfer, generating a free radical intermediate (*e.g.* for sulfite: $^{*}SO_3^- + e^- \rightarrow SO_3^{2-}$ or for methanol: $^{*}CH_2OH + e^- + H^+ \rightarrow CH_3OH$, with a redox potential of $\sim 0.7\,V$ vs NHE at pH 10 and $\sim 1.2\,V$ vs NHE at pH 7, respectively).[1] [36;110;112–115] These radicals are strong reducing agents ($\sim$ -2 V at pH 10 vs NHE for $SO_4^{2-} + H_2O + e^- \rightarrow {}^{*}SO_3^- + 2\,OH^-$ or -1.3 V vs NHE at pH 7 for $CH_2O + e^- + H^+ \rightarrow {}^{*}CH_2OH$).[36;113;115–117] Hence, these radicals are likely to transfer an electron to the conduction band of the CdS or the Pt domain directly, if no alternative electron acceptor, like molecular oxygen, is present (*e.g.* $^{*}CH_2OH \rightarrow CH_2O + H^+ + e^-_{CdS/Pt}$).[36;110;116] Thus, after absorbing one photon, two electrons are generated, which both might contribute to the HER. This effect is called "current doubling" and was observed for multiple alcoholic EDAs and diverse photocatalysts.[36;110;116;118–126] The extent of this process is contingent upon the energetic position of the semiconductor's electronic bands relative to the redox potentials of the EDAs and the radicals forming during oxidation.[89;103]

4.5 Synthesis of Metal-Semiconductor Nanohybrids

4.5.1 Synthesis of CdSe/CdS Dot-in-Rods

Cd-chalcogenide NCs of controlled size and shape can be synthesized using well-established, wet-chemical colloidal synthesis methods. High-temperature thermal reaction approaches in the presence of organic ligands ensure the formation

[1] Note that reduction reactions are shown where redox potentials are stated.

of NCs with high crystallinity and small size distribution.[11;40] The size of the formed NCs can be controlled *via* the reaction time, temperature, the amount of introduced precursor, and the use of ligands. As the ligands passivate the surface of the nuclei, they limit the accessibility for the monomer and decelerate the nuclei diffusion, enabling slow and steady growth.[127] Additionally, the attached ligands form a steric barrier to NP aggregation.[11] This steric stabilization is dependent on the ligands' interaction with the solvent and thus can be gradually reduced by adding an anti-solvent. As the attractive forces are increased for larger NPs, they aggregate at smaller quantities of added anti-solvent than smaller ones. Exploiting this fact, the size distribution of NP samples can be narrowed by size-selective precipitation after synthesis.[11] Furthermore, the introduction of specific ligands can facilitate anisotropic growth of the NC. As the ligands exhibit different affinities for the various facets of the NC, their selective attachment influences the facet-specific growth rates and therefore the shape of the NC. The crystallographic facets of the NC are determined by its crystal structure. CdSe NCs can either nucleate in a hexagonal wurtzite (w) or cubic zinc blende (zb) structure, depending on the reaction temperature.[62;128;129] The various facets of these crystal structures have different surface energies and polarity, enabling anisotropic growth in a kinetic growth regime.[40] Due to the polarity of the (001) and (00$\bar{1}$) facets in w-Cd-chalcogenides, the growth is generally faster along the c-axis, favoring 1D rod growth.[12] The anisotropic growth can be promoted further by introducing ligands that bind preferably to the (100) and (110) side facets of the NC, like phosphonic acids.[12;40;62]

By introducing a second semiconductor material, heterostructures of "mixed dimensionality" like CdSe/CdS DRs or nanotetrapods can be obtained.[62] These DRs can be synthesized using spherical w-CdSe NCs as seeds and growing a w-CdS rod domain on its (001) and (00$\bar{1}$) facet, whereas CdSe/CdS tetrapods can be obtained by growing w-CdS arms on the (111) facets of zb-CdSe seeds.[62;130] Within the obtained DRs, the CdSe seed is not located in the middle but closer to one end of the rod due to the higher surface energy and therefore larger growth rate of the (00$\bar{1}$) compared to the (001) facet (**Figure 4.10**; seed position at 1/3 to 1/4 of the rod's length).[40;62;130;131;131–133] Monomer attachment is favored at the chalcogenide-terminated, anionic (00$\bar{1}$) facet due to a reduced passivation by the electron-donating ligands compared to the Cd-terminated, cationic (001) facet.[134] Even in the case of an additional monolayer of Cd atoms at the (00$\bar{1}$) facet, this facet is more reactive, as the Cd atoms have more dangling bonds than at the (001) facet.[130;134] However, as the growth of the CdS domain is not restricted to the c-axis, some of the DRs exhibit a slightly larger diameter around

the CdSe core. This so-called bulb region has a reduced exciton confinement energy, and hence a reduced band gap compared to the rest of the CdS rod domain (*cf.* Figure 4.9).[76;94;135;136]

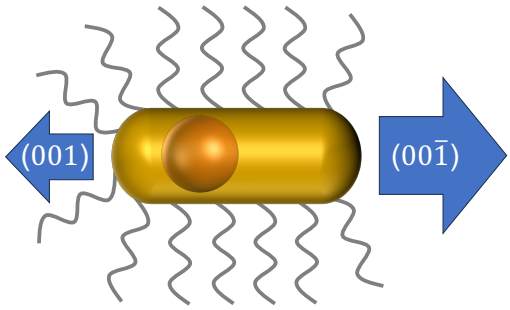

Figure 4.10: Scheme of the anisotropic growth along the c-axis of CdSe/CdS DRs. Due to higher surface energy and less ligand passivation, the growth rate is larger at the (00$\bar{1}$) than at the (001) facet.[40] The blue arrows indicate the growth rates at the respective facets.

4.5.2 Pt Deposition on CdSe/CdS Dot-in-Rods

The Pt-CdSe/CdS metal-semiconductor nanohybrid is obtained by depositing a Pt domain on the semiconductor NC. The metal deposition can be implemented either by a high-temperature synthesis or by photodeposition at RT.

Pt Deposition *via* High-Temperature Synthesis

The high-temperature synthesis approach is based on a thermal decomposition of a Pt compound (*e.g.* platinum(II) acetylacetonate), resulting in metal deposition on the semiconductor NC, in the presence of a reductant (*e.g.* 1,2-hexadecanediol).[90] The semiconductor NCs function as seeds for heterogeneous nucleation with a reduced energy barrier compared to homogeneous nucleation.[7] As the (00$\bar{1}$) facet of CdSe/CdS DRs exhibits the largest reactivity, weakest ligand passivation, and is additionally terminated by electron-rich sulfur atoms, the material will preferably deposit at this facet. Hence, the Pt domain growth can be directed selectively to the DR's tip opposing the CdSe core. However, as the reactivities of the (00$\bar{1}$) and (001) facet differ only slightly, a second domain may grow on the other tip of the DR. Therefore, reaction time and temperature, as well as the amount of Pt precursor, need to be adjusted and controlled precisely. For long reaction times and large amounts of Pt precursor, the selectivity diminishes, leading to metal deposition at both tips of the DR and alongside the DR's body.[90]

Pt Deposition *via* Photodeposition

Photodeposition exploits the photogenerated charge carriers inside the NP for selective metal (oxide) deposition at the NP's surface by reduction or oxidation of metal salts or organometallic precursors.[86;131] In order to limit the excitation to the semiconductor domain and suppress homogeneous nucleation of the metal, the excitation wavelength is typically adjusted to the semiconductor's band gap energy.[86] Following the formation of a small Pt seed, the photogenerated electrons quickly transfer into it, directing subsequent reduction events to this domain.[86] For small excitation powers, domain growth is therefore favored over the formation of a second Pt domain on the DR. In the case of CdSe/CdS DRs, the sulfur-terminated, electron-rich, and weakly passivated $(00\bar{1})$ facet is advantageous for light-induced, reductive metal deposition (**Figure 4.11**a). However, due to the reduced CB potential of the CdSe core compared to the CdS shell, photogenerated electrons can also transfer into the core, leading to metal deposition at the NP's surface next to it (Figure 4.11b).[86;91;131] The photogenerated holes are consumed by an EDA added. Additionally, the choice of ligand may influence the position of the metal deposition.[91]

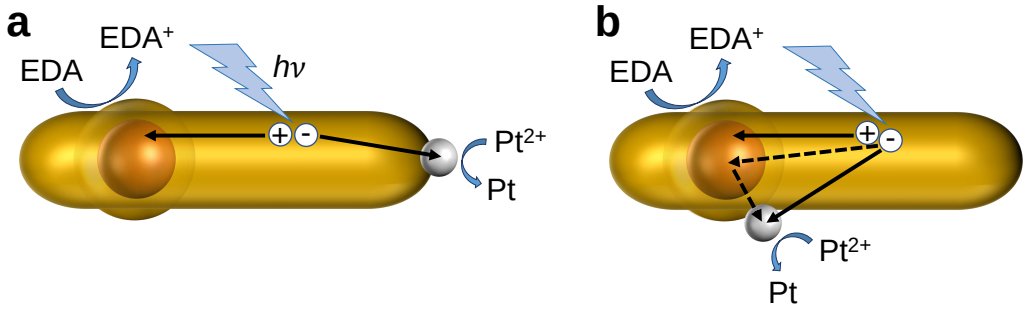

Figure 4.11: Illustration of reductive photodeposition of Pt on CdSe/CdS DRs. The photoexcited electrons reduce organometallic Pt precursors or metal salts (simplified as Pt^{2+}), leading to deposition of the metal on the DR's surface. The reduction occurs preferentially at the electron-rich $(00\bar{1})$ facet (a) or at the CdSe core (b). After a small Pt seed is formed, photogenerated electrons are drawn to this seed, favoring domain growth over the formation of a second Pt domain on the DR. The photogenerated holes are consumed by an EDA.

4.6 Characterization Methods

4.6.1 Static Ultraviolet-Visible Spectroscopy

Ultraviolet-visible (UV-vis) spectroscopy is an analytical method that can be used for determining the wavelength-dependent absorbance of a sample in the visible and ultraviolet (UV) range. The sample is irradiated with light of intensity I_0, and the attenuation of the radiation to intensity I is recorded. The Beer-Lambert law describes the relation of the absorbance or optical density (OD) of the sample with the concentration of the analyte c, the optical path length d, and the analyte's molar extinction coefficient ε.[77;80;137;138]

$$-\log\left(\frac{I}{I_0}\right) = OD = cd\varepsilon \tag{4.18}$$

The fraction of absorbed light Abs can be calculated from the OD

$$Abs = 1 - 10^{-OD}. \tag{4.19}$$

For individual NPs with a size much smaller than the wavelengths in the UV-vis range, scattering can be neglected.[139] In this case, the fraction of absorbed and transmitted light T sum up to 1.[80;137]

$$Abs + T = Abs + \frac{I}{I_0} = 1 \tag{4.20}$$

However, for samples that scatter light in the investigated wavelength range (*e.g.* agglomerates of NPs), or reflect light, the fraction of scattered and reflected light S and R, respectively, have to be added to Equation (4.20)

$$Abs + T + S + R = Abs + \frac{I}{I_0} = 1. \tag{4.21}$$

Therefore, in this case, the scattered and reflected light must be collected in order to determine the OD correctly

$$T + S + R = \frac{I}{I_0} = 10^{-OD}. \tag{4.22}$$

UV-vis spectrometer typically use a double beam line, consisting of one sample beam which passes through the cuvette holding the sample (measurement of I) and one reference beam (measurement of I_0). The light of both beams originates from the same polychromatic source, and the wavelength is adjusted by a

monochromator.[77;80] In classical spectrometers, both beams follow a linear path, with the detector behind the sample, measuring the transmitted light. In such a setup, scattered or reflected light does not reach the detector and thus contributes to the *OD* determined. In order to collect the scattered and reflected light, a spectrometer with an integrating sphere can be used.[137] The sample is placed inside the integrating sphere, which is coated with a diffuse reflective material (*e.g.* polytetrafluoroethylene or barium sulfate), and the detector is offset with respect to the sample beam path. The transmitted, scattered and reflected light is scattered diffusely inside the sphere and hence contributes to the intensity *I* measured by the detector. Therefore, this setup allows to determine the fraction of absorbed light even for samples that scatter strongly (*cf.* Equation (4.21) and Equation (4.22)). To account for scattering, reflection, and absorption by the solvent and cuvette, a baseline measurement is typically conducted. PL distorts the absorbance measurement. This effect is particularly severe in an integrating sphere where all the emitted light is directed onto the detector. Therefore, for highly fluorescent samples, the absorbance can be determined more precisely in a spectrometer with a linear beam path.[77] Alternatively, the fluorescence can be extinguished by adding a quenching agent.

4.6.2 Time-Resolved Photoluminescence Spectroscopy

The time-dependent PL behavior of fluorophores is typically characterized using time-correlated single-photon counting (TCSPC). This technique utilizes pulsed lasers for exciting the fluorophore and photomultiplier tubes for detecting the emitted photons. A scheme of a TCSPC setup is shown in **Figure 4.12**a. A time-to-amplitude converter (TAC) is utilized to determine the time between the laser pulse and the detection of the emitted photon. The TAC enables the time measurement by generating a voltage ramp that increases linearly with the elapsed time. The measured time intervals are plotted in a histogram, the PL decay curve (Figure 4.12b). To ensure accurate measurements, the excitation power must be kept low (roughly one emitted photon every 100 excitation pulses).[77] If the excitation power is too high, multiple photons may excite the sample, resulting in several emissions. However, only the first emitted photon can be detected due to the dead time of the TCSPC device, which is typically in the two-digit nanosecond range.[77] Hence, at large excitation powers, the histogram is biased towards shorter times. This effect is called pile-up effect.[77;140] The repetition rate of the pulsed laser is adjusted based on the lifetime of the fluorophore. If the repetition rate is too high, emitted photons may be assigned to the successive laser pulse, re-

sulting in significantly reduced times being determined.[77;140] Furthermore, the instrument's intrinsic response has to be characterized. This is implemented by measuring an instrument response function (IRF), using a scattering, zero lifetime sample (*e.g.* polystyrene NPs).[77]

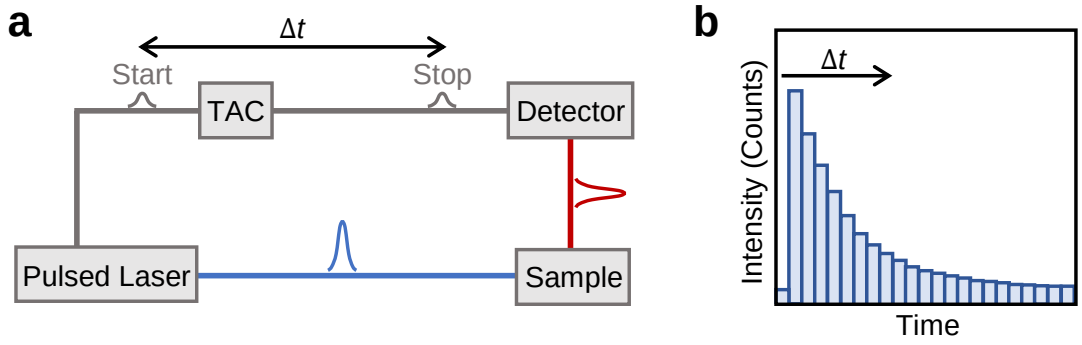

Figure 4.12: Schematic of a TCSPC system (a) and the recorded PL decay curve (b). Figure modified from Lakowicz,[77] © 2006, 1999, 1983 *Springer Science+Business Media, LLC*, used with permission.

Depending on the fluorophore investigated, the obtained PL decays can be described by mono- or multi-exponential decay curves. While fluorescent molecules exhibit mono-exponential PL decays, the PL decay of semiconductor NCs is typically multi-exponential due to numerous non-radiative decay channels.[141] Based on Equation (4.11), the decay of the PL intensity can be expressed as

$$I(t) = \sum_i A_i \cdot e^{-\frac{t}{\tau_i}}, \tag{4.23}$$

where A_i is the amplitude and τ_i the decay time of the respective decay channel.[77]

In the case of a multi-exponential decay, an average lifetime can be calculated. It can be determined using either an intensity- or amplitude-weighted approach

$$\tau_{\text{ave,IW}} = \frac{\sum_i A_i \tau_i^2}{\sum_i A_i \tau_i} \tag{4.24}$$

$$\tau_{\text{ave,AW}} = \frac{\sum_i A_i \tau_i}{\sum_i A_i}, \tag{4.25}$$

with the intensity-weighted $\tau_{\text{ave,IW}}$ and amplitude-weighted $\tau_{\text{ave,AW}}$ average lifetime.[142;143] Due to the quadratic contribution of the decay time, the amplitude-weighted average emphasizes short, whereas the intensity-weighted average highlights long decay times. For semiconductor NCs, the intensity-weighted average is commonly used as it is more stable against variations in the number of compo-

nents than the amplitude-weighted.[77;143;144] Therefore, the calculation is suitable for NC samples in which the lifetime varies due to different NC sizes.[145]

4.6.3 Transient Absorption Spectroscopy

TA spectroscopy is a pump-probe technique that measures time-dependent changes in the absorbance of a sample upon photoexcitation. As the experiment's time resolution depends on the pulse duration, femtosecond lasers are typically used. A scheme of a TA setup is shown in **Figure 4.13**. Using a beam splitter (BS), the

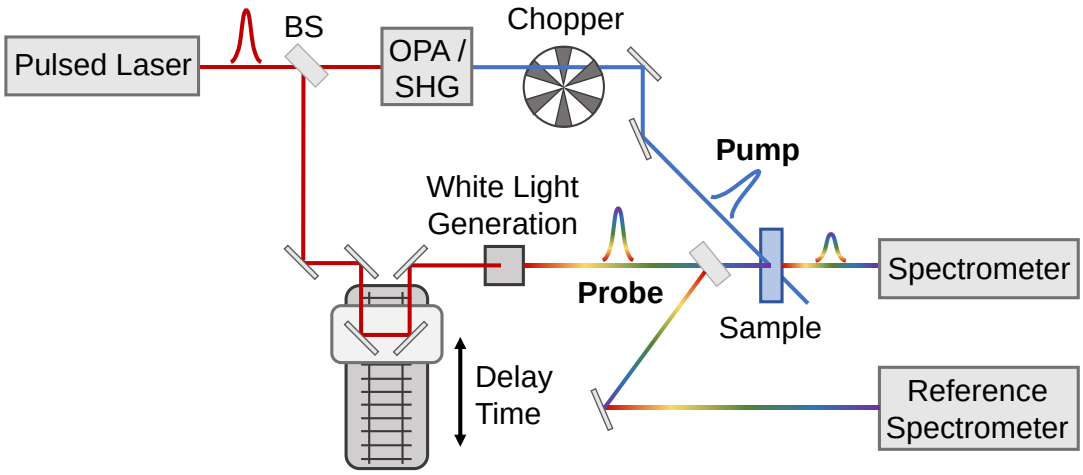

Figure 4.13: Scheme of the employed TA setup. An absorbance spectrum of the sample is recorded by a white light probe pulse alternately with and without excitation by a pump pulse of defined wavelength. A time resolution is obtained by varying the delay time between pump and probe pulse.

pulse is divided into two pulses: a pump pulse of high and a probe pulse of low intensity. The wavelength of the pump pulse photons is tuned by nonlinear optical effects like second harmonic generation (SHG) or using an optical parametric amplifier (OPA). The probe pulse is directed over a mechanical delay stage, allowing to adjust the time offset between the pump and probe pulse, which is referred to as the delay time. Using a transparent medium (*e.g.* a calcium fluoride crystal), a white light probe pulse is generated, enabling to probe the entire optical spectrum with one pulse. Eventually, the probe pulse is directed onto a spectrometer after passing the sample. A chopper is used to block every second pump pulse. Therefore, spectra of the sample are recorded alternately with and without excitation by the pump pulse. From each pair of measurements, the difference of the sample's absorbance in the excited and ground state ΔA is determined.[146]

$$\Delta A = A_{\text{excited state}} - A_{\text{ground state}} = OD_{\text{excited state}} - OD_{\text{ground state}} \tag{4.26}$$

Inserting the Beer-Lambert law (Equation (4.18)) into Equation (4.26) demonstrates that ΔA is independent of I_0.[146]

$$\Delta A = -\log\left(\frac{I_{\text{excited state}}}{I_0}\right) + \log\left(\frac{I_{\text{ground state}}}{I_0}\right) = \log\left(\frac{I_{\text{ground state}}}{I_{\text{excited state}}}\right) \tag{4.27}$$

The main source of noise in the experiment results from variations in the spectral intensity of the probe beam. To reduce this effect, the fluctuations in the white light spectrum can be monitored by a reference channel, employing a second spectrometer. As a mechanical delay stage enables only delay times of up to single-digit nanoseconds, a separate, electronically triggered white light laser source can be employed to generate probe pulses for TA measurements with longer delay times (ns to µs). The wavelength of the pump pulse is set to excite specific transitions in the sample. For investigating semiconductor NCs, the wavelength of the pump pulse is typically adjusted to excite electrons above the band gap of the NC (**Figure 4.14**a). In the measurement, contrast ($\Delta A \neq 0$) is mainly created from three different mechanisms: ground state bleach, photoinduced shift, and photoinduced absorption.

Ground State Bleach: After excitation by the pump pulse, photogenerated electrons and holes occupy the CB and VB, respectively, causing a reduced absorption of the probe pulse compared to the unexcited NC due to the Pauli exclusion principle (Figure 4.14b). The bleaching of the sample's absorption results in a negative ΔA (Figure 4.14e).[146]

Photoinduced Shift: In the excited NC, the electric field between excited charge carriers can induce a spectral shift of the NP's energy levels (Stark effect; Figure 4.14c). This results in a differential absorption with a positive and negative component (Figure 4.14f).[29;65;147]

Photoinduced Absorption: In the excited sample, the probe pulse can induce transitions of the excited charge carriers into higher excited states (Figure 4.14d). As these transitions are not available in the unexcited sample, the photoinduced absorption yields a positive ΔA (Figure 4.14g).[146;148]

In multicomponent nanostructures, the movement and recombination of the photoinduced charge carriers can be tracked as time-dependent changes in the TA spectrum.[24;149]

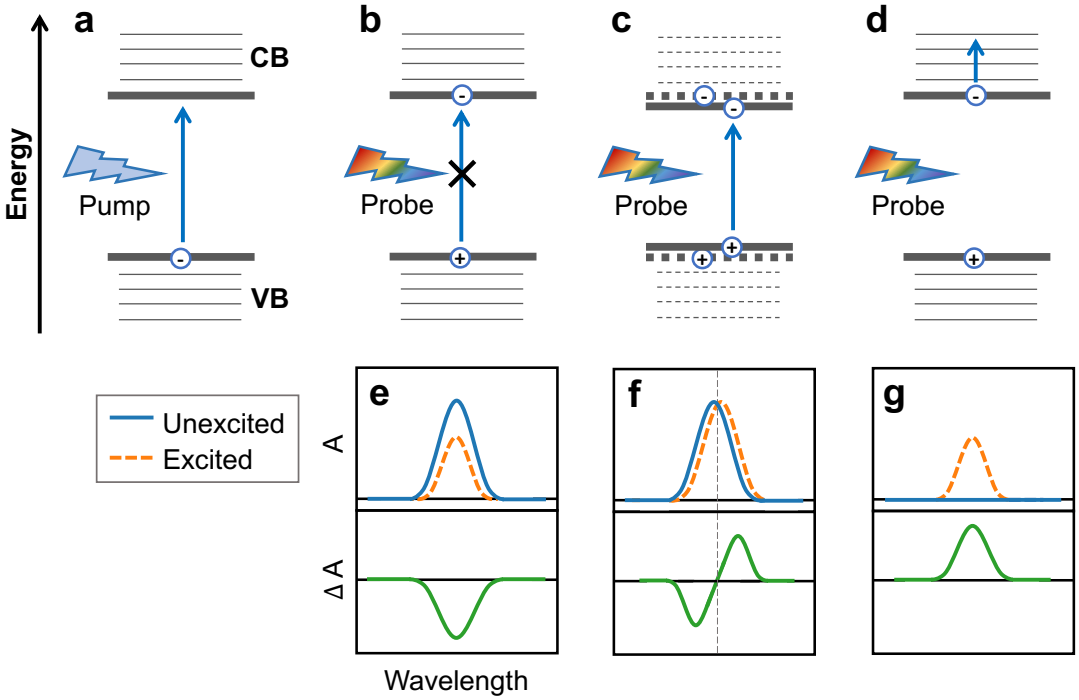

Figure 4.14: Scheme of the contrast mechanisms in TA on semiconductor NPs. The pump pulse excites an electron from the VB into the CB, creating a hole in the VB (a). After a distinct delay time, the probe pulse interacts with the excited NP (b-d). Due to blocking of transitions, the absorption of the excited NP is bleached, yielding a negative ΔA (e). Photoinduced charge carriers can cause a shift of the NC's energy levels, resulting in a derivative like ΔA (f). A positive ΔA occurs for photoinduced absorptions, which are transitions of the excited charge carriers into higher energy states (g).

5 Scope

The influence of the size, shape, and composition of the nanocatalyst, as well as the presence of different EDAs on the photocatalytic activity, was investigated in literature studies.[26–32;34–36] However, processes occurring at the NPs' surface were barely considered in the given explanations for the observed trends and phenomena. Furthermore, the EDA-induced formation of NP networks has not been reported so far, a process that significantly influences the charge carrier dynamics of the NPs and therefore also the photocatalytic yield.
The aim of this work was to draw a detailed picture of the processes limiting the photocatalytic activity. This was implemented by correlating the photocatalytic activity, charge carrier dynamics, and colloidal stability of Pt-tipped CdSe/CdS DRs with functional components of different number and dimensionality, as well as in the presence of different EDAs, in a comprehensive study. Firstly, suited syntheses and synthesis parameters for obtaining Pt-tipped CdSe/CdS DRs with functional components of desired number and size were found. The charge carrier dynamics and photocatalytic activity of various synthesized colloidal NPs in the presence of different EDAs (methanol (MeOH), ethanol (EtOH), isopropyl alcohol (IPA), Na_2SO_3, and the mixtures of Na_2S & Na_2SO_3, KOH & IPA, and KOH & MeOH) were investigated by TA and time-resolved PL spectroscopy, as well as steady-state hydrogen production measurements. The TA data was analyzed in detail to resolve all relevant processes during photocatalytic hydrogen production and evaluate their dependency on the NPs' dimensionality and the interaction with an EDA. In this context, it was investigated whether the deposition of Pt domains induces a static or dynamic PL quenching. Electron microscopy, DLS, and static spectroscopy measurements were conducted to investigate the colloidal stability of the NPs in the presence of different EDAs and during illumination. Illumination time-dependent measurements were performed to gain insights into the processes occurring at the NPs' surface during the solar-to-fuel conversion. Furthermore, excitation power density-dependent measurements were executed to assess the lifetime of charge carriers participating in the photocatalytic process and to validate the occurrence of NP networks.

6 Materials and Methods

6.1 Materials

Trioctylphosphine (TOP, 90 %), selenium (>99 %), sulfur (>99 %), n-octylamine (99 %), oleylamine (OAm, 70 %), oleic acid (OA, 90 %), 1,2-hexadecanediol (HDD, 90 %), diphenyl ether (DPE, 99 %), n-hexylphosphonic acid (HPA, 95 %), 2,3,6,7-tetrahydro-9-trifluoromethyl-1H,5H-quinolizino(9,1-gh)coumarin (coumarin 153, 99 %), sodium sulfide (95 %), (1,5-cyclooctadiene)dimethylplatinum(II) (COD-DM-Pt, 97 %), triethylamine (>99 %), and 11-mercaptoundecanoic acid (MUA, 95 %) were obtained from Sigma-Aldrich. Trioctylphosphine oxide (TOPO, 98 %), potassium hydroxide (≥85 %), and sodium sulfite (98 %) were purchased from Merck, while n-octadecylphosphonic acid (ODPA, 98 %) was obtained from PCI Synthesis and cadmium oxide (>99 %) from ChemPur. Toluene (≥99.8 %), acetone (>99 %), MeOH (≥99.8 %), EtOH (≥99.8 %), chloroform (> 99 %), IPA (≥99.7 %) were acquired from VWR Chemicals. Nonanoic acid (97 %), platinum(II) acetylacetonate (98 %) were purchased from abcr, 1,2-dichlorobenzene (DCB, >99 %) was purchased from Acros Organics. Hydrogen gas (≥99.999 %) was obtained from Westfalen AG and nitrogen gas (≥99.999 %) from SOL Group. Argon gas (≥99.999 %) was purchased from Sauerstoffwerk Steinfurt E. Howe GmbH & Co. KG and the argon-hydrogen mixture (2.000 % hydrogen) from Linde GmbH. Ultrapure water (18.2 MΩ cm, Millipore) was used in all experiments. All chemicals were used as received.

6.2 Synthesis of CdSe Nanocrystals

The procedure reported by Manna *et al.* was used to prepare CdSe seeds.[49] In a 25 mL three-necked round-bottom quartz-glass flask, TOPO (3.0 g), ODPA (280 mg) and CdO (60 mg, 0.47 mmol) were combined and heated to 150 °C under vacuum for one hour. Subsequently, the CdO was dissolved by heating the solution to 320 °C under nitrogen for 30 min. Optionally, a second degassing step was performed at this point by lowering the temperature to 150 °C under vacuum

for half an hour. Afterwards, the temperature was set to 380 °C under nitrogen and TOP (1.5 g) was injected at a temperature of 360 °C. Once the temperature recovered to 380 °C, a solution of Se:TOP (Se (58 mg, 0.73 mmol) dissolved in TOP (360 mg)) was rapidly injected. Depending on the desired NP size, the reaction was allowed to proceed for a couple of seconds or quenched immediately using a water bath or an ice bath with 25 vol% acetone in it. At a suspension temperature of 150 °C, toluene (5 mL) was injected. The NPs were precipitated by centrifugation after the addition of acetone and MeOH as anti-solvents. The precipitated NPs were redispersed in toluene and the cleaning procedure was repeated multiple times. After cleaning, the NPs were stored in a glove box under nitrogen atmosphere.

6.3 Synthesis of CdSe/CdS Dot-in-Rod Nanocrystals

The CdSe/CdS DRs were synthesized following the procedure by Manna and coworkers with some modifications.[49] TOPO (3.0 g), ODPA (290 mg), HPA (90 mg), and CdO (90 mg, 0.70 mmol) were introduced into a 25 mL three-necked round-bottom flask and degassed at 150 °C under vacuum for one hour. Afterwards, the solution was heated to 300 °C under nitrogen until it turned optically clear and colorless. A second degassing step was carried out by reducing the temperature to 150 °C under vacuum for half an hour. Meanwhile, an injection suspension was prepared by dissolving CdSe seeds (50 nmol) and sulfur (120 mg, 3.7 mmol) in TOP (2 mL). The dissolution of the sulfur was facilitated by heating the injection solution to 80 °C for 10 min. The main solution was heated under nitrogen, and at 330 °C TOP (1.5 mL) was injected, followed by a rapid injection of the CdSe/S:TOP suspension at 340 °C. The reaction was allowed to proceed for 8 min after the temperature recovered to 340 °C. Afterwards, the reaction was cooled by using an air blower. At 150 °C, the reaction was finally quenched by injecting toluene (12 mL) and octylamine (1.5 mL). After the synthesis, a size-selective precipitation was performed repeatedly using an anti-solvent mixture of acetone and MeOH and centrifugation. The product was stored in a glove box under nitrogen atmosphere.

6.4 Pt Tipping on CdSe/CdS Dot-in-Rods

Pt domains were deposited on the CdSe/CdS DRs following the hot-injection procedure by Mokari and coauthors,[90] or the photodeposition method by Alivi-

satos *et al.*[86] The products were stored in a glove box under inert atmosphere.

6.4.1 Pt Tipping *via* Hot-Injection

In a 25 mL three-necked round-bottom flask, OA (0.2 mL), OAm (0.2 mL), HDD (43.0 mg), and DPE (10 mL) were mixed and heated to 80 °C under vacuum for 45 min. Simultaneously, CdSe/CdS DRs (approximately 40 nmol (concentration deduced from the absorbance spectrum, based on the calculations from Dorfs *et al.*)[150]) were concentrated by evaporating the solvent under inert atmosphere. The dried NPs were combined with Pt(II) acetylacetonate (12 mg, 30.5 µmol) and dissolved in DCB (2.5 mL). This NP suspension was heated to 70 °C for 10 min. The surfactant solution in the flask was heated to 200 °C under nitrogen, and the mixture of DRs and Pt precursor was injected. The reaction proceeded for 5 min and was quenched quickly by cooling the suspension with a water bath. The tipped DRs were washed twice and separated from homonucleated Pt NPs by precipitation *via* the addition of EtOH, centrifugation, and redispersion in toluene.

6.4.2 Pt Tipping *via* Photodeposition

Under inert atmosphere, a COD-DM-Pt solution in toluene (90 µL, 200 mM), triethylamine (100 µL) and a DR suspension in toluene (250 µL) were combined in a NMR tube. The sealed tube was illuminated by a 445 nm LED (Thorlabs SOLIS-445C), at $\sim$ 650 mW of total output power ($\sim$ 35 mW cm^{-2} and therefore $\sim$ 37 mW on the total sample area inside the NMR tube of $\sim$ 1.05 cm^2). The suspension was illuminated for several hours.

6.5 Synthesis of Pt NPs

For synthesizing Pt NPs, the hot-injection protocol for Pt-tipping of DRs by Mokari *et al.* described above was modified (Section 6.4.1) by omitting the injection of DRs. The homonucleated NPs were precipitated size-selectively using centrifugation and methanol as an anti-solvent, followed by redispersion in toluene.

6.6 Ligand Exchange and Phase Transfer to Water

For transferring the Pt-tipped and bare CdSe/CdS DRs into aqueous media, the organic, hydrophobic ligands on the NPs were exchanged to hydrophilic MUA

following the procedure by Banin *et al.*[151] The MUA (13 mg, 59.5 µmol) was added to the NPs in chloroform (10 mL, roughly 4000 MUA molecules per Pt-DR and roughly 5000 MUA molecules per bare DR), and the suspension was shaken and sonicated in order to disperse the MUA (*cf.* **Figure 6.1**). A KOH solution (2 mL, ∼0.1 M) was added to the NP suspension forming a second phase above the chloroform phase. After vigorous shaking, the MUA-capped NPs transferred into the upper, aqueous phase, which was subsequently separated. The procedure of adding KOH solution (0.5 mL each) and separation of the upper phase was repeated four times. The transferred NPs were precipitated by centrifugation, adding MeOH as an anti-solvent and were redispersed in water.

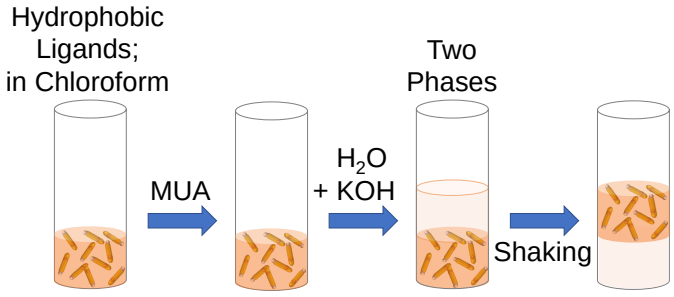

Figure 6.1: Scheme illustrating the steps during ligand exchange to MUA and phase transfer to water.

6.7 Determining the Concentration of CdSe Nanoparticles

The size-dependent absorption properties of CdSe NCs were studied systematically by Mulvaney *et al.*[152] They investigated the optical absorption coefficients of these NCs by utilizing inductively coupled plasma-optical emission spectroscopy and transmission electron microscopy (TEM), obtaining size-dependent band-edge calibration curves. By fitting their experimental data they derived the relation

$$D = 59.60816 - 0.54736\lambda_{E_{1S}} + 1.8873 \cdot 10^{-3}\lambda_{E_{1S}}^2 - 2.85743 \cdot 10^{-6}\lambda_{E_{1S}}^3 + 1.62974 \cdot 10^{-9}\lambda_{E_{1S}}^4 \quad (6.1)$$

for CdSe NCs of a diameter D (in nm) between 2 nm and 8 nm, with $\lambda_{E_{1S}}$ (in nm) as the wavelength of the first excitonic absorption peak E_{1S}. Additionally, the

molar extinction coefficient $\left(\varepsilon_{1S}, \text{in}\frac{1}{\text{M cm}}\right)$ was calculated

$$\varepsilon_{1S} = 155507 + 6.67054 \cdot 10^{13} \exp\left(-\frac{E_{1S}}{0.10551}\right), \tag{6.2}$$

where E_{1S} is the energy (in eV) of the first excitonic peak. The concentration of the CdSe NCs [NCs] (in M) was derived from the Beer-Lambert law (see Equation (4.18))

$$[\text{NCs}] = \frac{OD}{d \cdot \varepsilon_{1S}} \cdot \frac{\Delta E_{1S,\text{HWHM}}}{0.06\,\text{eV}}, \tag{6.3}$$

with the optical path length d (in cm), the measured optical density OD at peak maximum and the half-width-half-maximum of the first excitonic peak on the lower energy side $\Delta E_{1S,\text{HWHM}}$ (in eV). The second term of this equation considers the distribution width of the NC ensemble.[152]

6.8 Determining the Concentration of CdSe/CdS DRs

Analogous to CdSe NPs, the CdSe/CdS DRs exhibit a size-dependent absorption. Dorfs *et al.* state that the molar extinction coefficient can be calculated from the optical density at high energies (*e.g.* at 350 nm), since this high energy absorption was found to be dependent on the DRs' volume but not on its dimensions.[150] Conducting TEM and atomic absorption spectroscopy, they found the relation

$$\varepsilon = 28326.9 \cdot V \frac{\text{L}}{\text{mol cm nm}^3} \tag{6.4}$$

for the molar extinction coefficient at 350 nm, with the DRs volume V. Using the Beer-Lambert law (Equation (4.18)), the concentration of the DR sample can be calculated after measuring the OD at 350 nm.

6.9 Transmission Electron Microscopy

Conventional TEM measurements were carried out at a JEOL, JEM-1011 microscope operating at 100 kV accelerating voltage. High-resolution TEM (HRTEM) and high-angle annular dark field scanning TEM (HAADF STEM) measurements were conducted at a JEOL, JEM-2200FS microscope at an accelerating voltage of 200 kV. TEM samples were prepared by drop-casting roughly 10 µL of a diluted NP suspension onto a carbon-coated 400-mesh copper grid. Cryo-TEM measurements were performed at a FEI Tecnai G2 Spirit Twin at an accelerating voltage

of 120 kV. The samples for cryo-TEM imaging were prepared using a FEI Company, Vitrobot Mark IV for vitrification in liquid ethane. The micrographs were analyzed using the software ImageJ. The measurements were conducted by Stefan Werner, Andrea Koeppen, and Ulf Koenig (*Institut für Physikalische Chemie, Universität Hamburg*).

6.10 Dynamic Light Scattering

DLS measurements were conducted in a DLS instrument (Malvern Panalytical Ltd, Zetasizer Pro Blue Label). A dynamic viscosity of 0.8872 mPa s (water at 25°C) and a refractive index of 2.53 (CdSe/CdS NPs) was set for all measurements. The software ZS Xplorer was used for instrument control and data recording.

6.11 Static Ultraviolet-Visible Spectroscopy

The *OD* of the colloidal NP samples was determined in an UV-vis spectrometer (Agilent Technologies, Cary 5000) equipped with an integrating sphere (labsphere, DRA-2500), or in a spectrometer with a linear beam path (Agilent Technologies, Varian Inc., Cary 50). NP samples of 3 mL were transferred into quartz-glass cuvettes (Hellma Analytics) with an optical path length of 1 cm. In the spectrometer with the integrating sphere, the cuvette was placed in center position inside the integrating sphere. The software Cary WinUV for UV-vis-NIR applications was used for instrument control and data recording.

6.12 Transient Absorption Spectroscopy

The TA measurements with a femtosecond resolution (fs-TA measurements) were performed using an amplified Ti-Sapphire laser system (Spectra-Physics, Spitfire-Ace, 800 nm, 1 kHz, 35 fs pulse duration) in combination with a TA spectrometer (Ultrafast Systems, HELIOS). The laser beam was split into two parts. The first part was used for generating the pump beam *via* SHG in a β-barium borate crystal for the 400 nm and an OPA (Light Conversion, TOPAS Prime) for the 450 nm pump pulse. The second part was used to generate white light in a calcium fluoride crystal, after passing a delay stage. The pump beam was guided through a chopper with a frequency of 500 Hz. For the TA measurements with a nano- to microsecond resolution (ns-TA measurements), a separate spectrometer (Ultra-

fast Systems, EOS) was utilized. A 2 kHz white light probe beam was generated by an electronically triggered white light laser source. The same pump beam was used for the fs-TA and ns-TA experiments. The excitation fluence was set to 30 µJ cm^{-2} for all measurements. For both types of TA experiments, both, pump and probe beam were focused onto the NP sample, which was rapidly stirred in a quartz-glass cuvette of 2 mm optical path length. The longest delay time producible with the fs-TA setup was $\sim$7.5 ns and the shortest delay time achievable with the ns-TA setup was $\sim$1 ns. The TA measurements were conducted in collaboration with Yannic U. Staechelin (*Lange Research Group, Institut für Physikalische Chemie, Universität Hamburg*).

6.13 Static Photoluminescence Spectroscopy

Static PL spectra were recorded and QY_{PL} was determined using a spectrofluorometer system (Jobin Yvon HORIBA, Fluorolog-3), equipped with a photomultiplier (Jobin Yvon HORIBA, Spex DM302). Samples were diluted to $OD \leq 0.1$ and measured in quartz-glass cuvettes with an optical path length of 1 cm. The software FluorEssence (HORIBA), OriginPro 2024 (OriginLab Corporation) and a self-written script in MATLAB (The MathWorks Inc.) were used for instrument control, data recording and analysis, as well as for determining PL quantum yields.
Alternatively, PL quantum yields were determined relative to the standard coumarin 153 in EtOH. The quantum yield of the fluorophore was calculated by relating the integrated intensity of the emission I_{Em}, the OD, and the refractive index of the solvent n of the fluorophore and the standard (subscript "ref").[77;153]

$$QY_{\mathrm{PL}} = QY_{\mathrm{PL,\,ref}} \frac{I_{\mathrm{Em}}}{I_{\mathrm{Em,\,ref}}} \frac{OD_{\mathrm{ref}}}{OD} \frac{n^2}{n_{\mathrm{ref}}^2} \tag{6.5}$$

In this context, static PL spectra of the dye and NP samples were recorded using a fluorescence lifetime spectrometer (PicoQuant GmbH, FluoTime 300), equipped with a high-power supercontinuum laser (NKT Photonics, SuperK Fianium) and a tunable high-contrast filter (NKT Photonics, LLTF Contrast), operating in long range mode. The software EasyTau 2 (PicoQuant GmbH) was used for instrument control, data recording, and analysis. The sample's OD was determined in an UV-vis spectrometer equipped with an integrating sphere (see above).

6.14 Time-Resolved Photoluminescence Spectroscopy

The PL decay kinetics were recorded using a fluorescence lifetime spectrometer (PicoQuant GmbH, FluoTime 300), equipped with a high-power supercontinuum laser (NKT Photonics, SuperK Fianium) and a tunable high-contrast filter (NKT Photonics, LLTF Contrast). Samples were diluted to $OD \leq 0.1$ and measured in quartz-glass cuvettes with an optical path length of 1 cm. The IRF was measured using a polystyrene NP suspension. The software EasyTau 2 (PicoQuant GmbH) was used for instrument control, data recording, and analysis. The emission monochromator was adjusted to the wavelength of the PL peak maximum for recording the PL decay kinetic.

6.15 X-Ray Diffraction

X-ray diffraction (XRD) measurements were conducted employing a diffractometer (Philips, X'Pert PRO MPD) with a Bragg-Brentano geometry, containing a high-intensity ceramic sealed tube (Philips, 3 kW) as a Cu Ka X-ray source with a wavelength of 1.5405 Å. XRD samples were prepared by drop-casting a concentrated NP suspension in toluene onto a Si wafer substrate. The solvent was evaporated and the drop-casting process was repeated until a visible layer was deposited. The measurements were conducted by Nina Schober (*Institut für Physikalische Chemie, Universität Hamburg*).

6.16 pH Value Measurements

pH values were measured using a pH meter (Mettler Toledo, FiveEasy), equipped with a pH electrode (InLab, pH electrode Micro).

6.17 Steady-State Hydrogen Production Measurements

For the hydrogen generation measurements a setup was designed and assembled (*cf.* **Figure 6.2**a+b). The suspension of MUA-capped NPs in water was transferred into a cuvette setup, combining a 50 mL quartz-glass cuvette with an optical path length of 2 cm, a 100 mL flask, two glass pipes with valves and two septa (165 mL gas volume; *cf.* Figure 6.2b). The *OD* of all samples was adjusted to roughly 0.8 at 445 nm inside the cuvette. Firstly, the NPs suspension and the cuvette setup

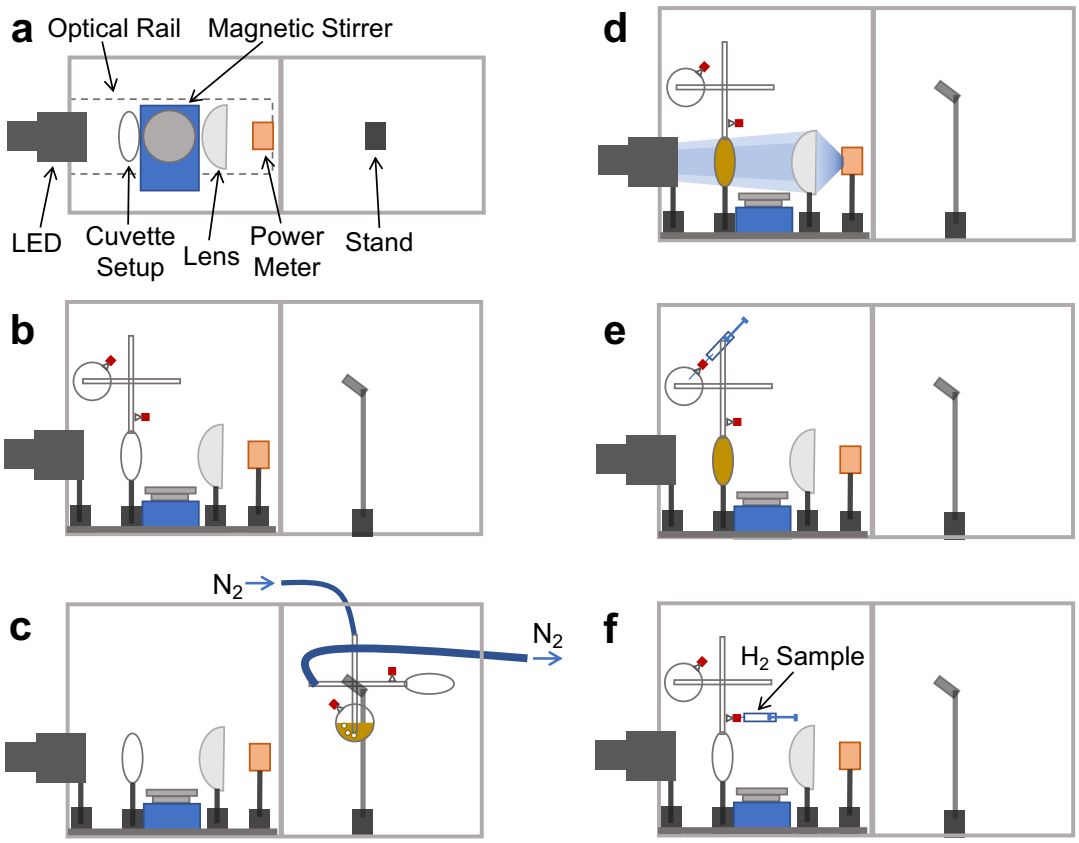

Figure 6.2: Scheme of the setup assembled for steady-state hydrogen production measurements in top (a) and side (b-f) view. The NP suspension and the cuvette setup are purged with nitrogen (c), the photocatalysts are illuminated inside the quartz-glass cuvette (d), and gas aliquots are taken from the upper septum (e). For calibration, hydrogen samples can be injected at the lower septum (f).

were purged with nitrogen for roughly 20 minutes (*cf.* Figure 6.2c). To ensure a complete gas exchange inside the cuvette setup, the cuvette was turned multiple times during this purging process, guiding the NPs suspension into the quartz glass cuvette and back into the flask. After purging, the valves were sealed, the NP suspension was guided into the quartz-glass cuvette and the whole cuvette setup was transferred to its holder. For exciting the photocatalysts a 445 nm LED (Thorlabs, SOLIS-445C) was used, adjusted to 115 mW of total output power ($\sim$7.92 mW cm^{-2}), while the suspension was stirred (*cf.* Figure 6.2d). After each 15 minutes of illumination, a gas aliquot of 500 µL was extracted from the cuvette setup using a gastight syringe (*cf.* Figure 6.2e). To prevent local accumulation of the generated hydrogen gas but distribute the gas uniformly, the cuvette setup was turned and shaken before extracting the gas aliquot at the upper septum. The aliquot was injected into a gas chromatograph (GC), equipped with a thermal conductivity detector (Shimadzu, Nexis GC-2030). The GC was equipped with

two columns, a 5 Å molecular sieve (SH-Rt-Msieve 5A, 30 m, 0.53 mm, 50 µm) and a porous polymer Q-BOND column (SH-Rt-Q-BOND, 30 m, 0.53 mm, 20 µm) for separating permanent gases. Nitrogen was used as carrier gas. The software LabSolutions (Shimadzu) was used for instrument control, data recording and analysis.

The measured hydrogen volumes were plotted against time and the data was fitted linearly for determining the hydrogen production rate. In **Figure 6.3** an exemplary measurement of Pt-tipped DRs in the presence of IPA is shown. The hydrogen production rate determined is $6.32 \pm 0.36 \frac{\mu L}{min}$. The stated error was derived from the deviation of the data points from the linear fit applied, while the error bars of the data points were calculated from the average (black error bar) and maximum (grey error bar) relative standard deviation of the hydrogen calibration measurements (see Section 6.17.1 for detailed description on hydrogen calibration measurements).

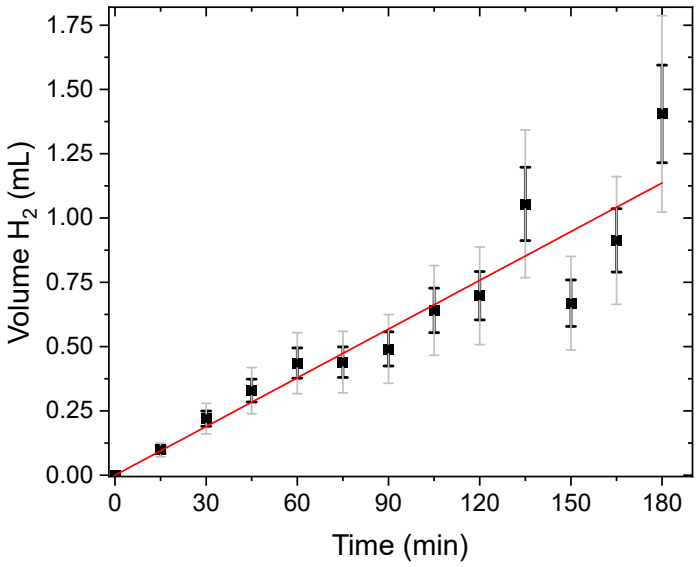

Figure 6.3: Steady-state hydrogen production measurement of Pt-CdSe/CdS DRs using IPA as a sacrificial EDA. The hydrogen volumes were measured using a GC. The data points were fitted linearly for determining the hydrogen production rate. The error bars were calculated from the average (black error bar) and maximum (grey error bar) relative standard deviation of the hydrogen calibration measurements (*cf.* Figure 6.4).

The quantum efficiency in hydrogen production (QE_{H_2}) can be calculated from the number of generated hydrogen molecules per time $\frac{N_{H_2}}{t}$ and the number of

absorbed photons per time $\frac{N_{\text{Photons}}}{t}$.[80]

$$QE_{\text{H}_2} = \frac{\frac{N_{\text{H}_2}}{t} \cdot 2}{\frac{N_{\text{Photons}}}{t}} \tag{6.6}$$

A factor of two is added in the numerator, since for each hydrogen molecule generated, two protons have to be reduced.[32] The number of generated hydrogen molecules per time can be calculated from the determined hydrogen production rate $\frac{V_{\text{H}_2}}{t}$ and the molar volume of an ideal gas V_{m} $\left(V_{\text{m}} = 22.4\,\frac{\text{L}}{\text{mol}}\right)$[80]

$$\frac{N_{\text{H}_2}}{t} = \frac{n_{\text{H}_2} \cdot N_{\text{A}}}{t} = \frac{V_{\text{H}_2}}{t} \cdot \frac{N_{\text{A}}}{V_{\text{m}}}, \tag{6.7}$$

with the amount of substance of hydrogen molecules n_{H_2} and the Avogadro constant N_{A}.[32;80]

The number of absorbed photons per time can be determined from the absorbed photon flux Φ_{abs} (number of absorbed photons per time per area) and the illuminated area of the cuvette A

$$\frac{N_{\text{Photons}}}{t} = \Phi_{\text{abs}} \cdot A. \tag{6.8}$$

The absorbed photon flux can be calculated from the absorbed power P_{abs} and the energy of each photon E_{Photon}

$$\Phi_{\text{abs}} = \frac{H_{\text{abs}}}{E_{\text{Photon}}} = \frac{P_{\text{abs}}}{A \cdot E_{\text{Photon}}} = \frac{P_{\text{abs}} \cdot \lambda}{A \cdot h \cdot c}, \tag{6.9}$$

with the absorbed power density H_{abs}, the wavelength of the exciting light λ, the Planck constant h and the speed of light c.[80] The absorbed power was calculated from the incident power that hits the sample P_{PC} (see Section 6.17.2 and Equation (6.13) for detailed description on LED power calibration) and the OD of the sample (see Equation (4.19)) at 445 nm

$$P_{\text{abs}} = Abs \cdot P_{\text{PC}} = \left(1 - \frac{1}{10^{OD}}\right) \cdot P_{\text{PC}}. \tag{6.10}$$

The OD of each sample was determined using a spectrometer equipped with an integrating sphere (see experimental section). After inserting Equation (6.7), Equation (6.8), Equation (6.9), and Equation (6.10) into Equation (6.6) the quantum efficiency in hydrogen production can eventually be calculated from the OD of the sample at 445 nm, the incident power, and the hydrogen production rate

measured

$$QE_{H_2} = \frac{\frac{V_{H_2}}{t} \cdot \frac{N_A}{V_m} \cdot 2}{\frac{\left(1-\frac{1}{10^{OD}}\right) \cdot P_{PC} \cdot \lambda}{h \cdot c}}. \tag{6.11}$$

In the case of the Pt-DRs in the presence of 10 vol% IPA (*cf.* Figure 6.3) a QE_{H_2} of 2.63 ± 0.14 % results:
OD = 0.782, P_{PC} = 115 mW (see Section 6.17.2 for LED power calibration), $\frac{V_{H_2}}{t}$ = $6.32 \pm 0.36 \frac{\mu L}{min}$

$$\frac{N_{H_2}}{t} = 1.70 \cdot 10^{17} \frac{1}{min}$$

$$\frac{N_{Photons}}{t} = 1.29 \cdot 10^{19} \frac{1}{min}$$

$$\Rightarrow QE_{H_2} = 2.63\,\%$$

6.17.1 Calibration of Hydrogen Volumes in Gas Chromatography

An analytical gas chromatography calibration was implemented, enabling precise quantification of the unknown hydrogen volumes inside the cuvette setup during the steady-state hydrogen generation measurements. Firstly, a gas sampling tube was filled with pure hydrogen gas. Secondly, distinct volumes of hydrogen gas were transferred from the gas sampling tube to the cuvette setup, using gastight syringes of different sizes. The cuvette setup was filled with 45 mL of water and 5 mL of IPA and was previously purged with nitrogen. The hydrogen samples were injected at the lower septum, above the quartz-glass cuvette, in order to mimic the hydrogen generation inside this cuvette and the distribution of the hydrogen gas within the cuvette setup authentically (*cf.* Figure 6.2f). Subsequently, a hydrogen calibration curve was recorded by withdrawing gas aliquots of 500 µL from the cuvette setup and injecting these into the GC (see **Figure 6.4**). The cuvette was turned and shaken (see above) before aliquot extraction. It was found that it takes some minutes for the hydrogen gas to distribute uniformly within the cuvette setup. After 15 minutes, the amount of hydrogen stays at a constant level. The calibration curve was generated from aliquots taken 15 and 30 minutes after injection of the hydrogen sample. The process of purging with nitrogen, hydrogen sample injection, and aliquot extraction was repeated multiple times on different days for each hydrogen volume. Since the gas aliquots for calibration are extracted directly from the cuvette setup, the process of aliquot extraction from the cuvette, the gas distribution within the cuvette, and further experimental conditions are precisely reproduced and hence integrated into the

calibration. The average and maximum relative standard deviation of the measurements was used for determining the error bars in the steady-state hydrogen production measurements (*cf.* Figure 6.3).

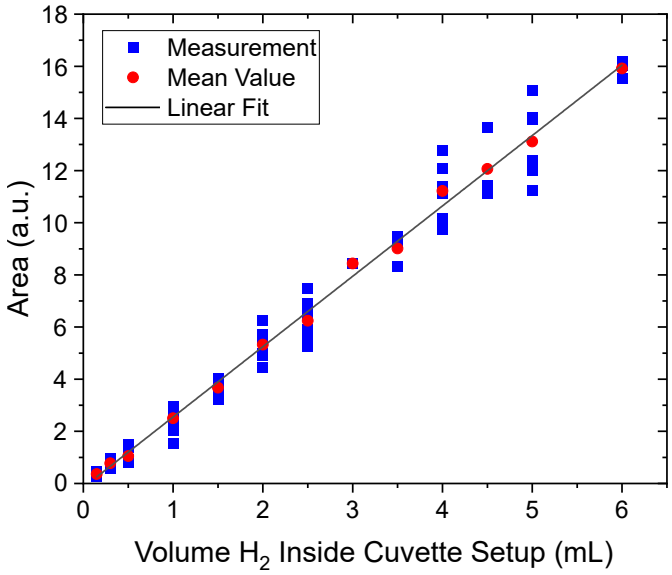

Figure 6.4: Hydrogen calibration curve of the GC. The measured peak area of the hydrogen peak is plotted against the hydrogen volumes injected into the cuvette setup. The mean value of the measurements conducted at each hydrogen volume is used for the linear regression analysis.

6.17.2 Calibration of LED Power

The power emitted by the LED at distinct applied currents was calibrated, utilizing a power meter sensor (Thorlabs, S425C Thermal Power Sensor Head, 0.19-20 µm, 10 W) and a digital console (Thorlabs, PM100D Compact Power and Energy Meter Console). The LED beam is focused onto the power meter sensor head by a plano-convex lens (Thorlabs, N-BK7 Plano-Convex Lens, AR Coating 350 - 700 nm; *cf.* Figure 6.2d). By focusing the entire LED beam onto the sensor head, the small divergence and the slightly non-uniform power density along the cross-section of the beam become irrelevant. Additionally, all optical components are mounted onto an optical rail, ensuring a linear beam path (*cf.* Figure 6.2a). By mounting a mesh filter in front of the LED, very small (3.5 mW of total output power, $\sim 0.24\,\mathrm{mW\,cm^{-2}}$) excitation powers could be achieved. Light scattering at the second cuvette window was considered by measuring the power of the LED beam 1. after passing a cuvette filled with water and 2 cm optical path length $P_{2\mathrm{cm}}$ (**Figure 6.5**a), 2. after passing a cuvette filled with water and 4 cm optical path

length P_{4cm} (Figure 6.5b), 3. without a cuvette in the beam path P_0 (Figure 6.5c). The first measurement considers the attenuation of the excitation power at the first cuvette window and due to the solvent, however, it also contains an attenuation of power due to the second cuvette window. Therefore, the measured power P_{2cm} is slightly lower than the power that hits the sample P_{PC}. In order to calculate and eventually subtract the contribution of the second cuvette window, the power that would have passed an empty cuvette was determined first

$$P_{\text{EmptyCuvette}} = P_{2cm} - P_{4cm} + P_{2cm}. \tag{6.12}$$

Finally, the power that excites the aqueous NP suspension P_{PC} without the attenuation by the second cuvette window $\left(\frac{P_0 - P_{\text{EmptyCuvette}}}{2}\right)$ can be calculated

$$P_{PC} = \frac{P_0 - P_{\text{EmptyCuvette}}}{2} + P_{2cm}. \tag{6.13}$$

In the case of 100 mA current applied to the LED (P_0 = 0.119 W, P_{2cm} = 0.112 W, P_{4cm} = 0.111 W), the photocatalyst sample is excited by 115 mW

$$P_{\text{EmptyCuvette}} = 0.112\,\text{W} - 0.111\,\text{W} + 0.112\,\text{W} = 0.113\,\text{W}$$

$$P_{PC} = \frac{0.119\,\text{W} - 0.113\,\text{W}}{2} + 0.112\,\text{W} = 0.115\,\text{W}.$$

The determined powers exciting the sample at certain currents applied to the LED are plotted in **Figure 6.6**.

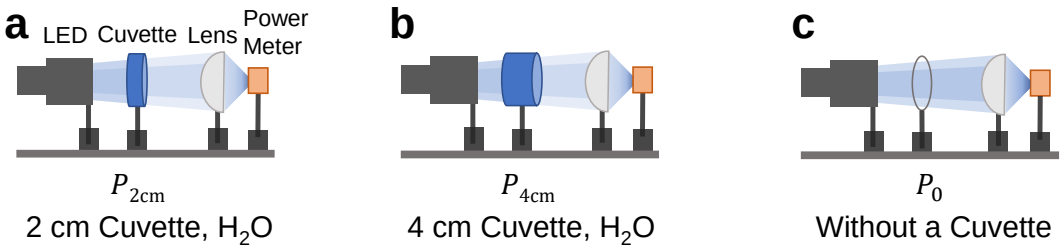

Figure 6.5: Scheme illustrating the three measurements implemented for calibrating the excitation power of the LED. The power of the LED beam was measured by a power meter after passing a cuvette filled with water and 2 cm optical path length (a), after passing a cuvette filled with water and 4 cm optical path length (b), without a cuvette in the beam path (c).

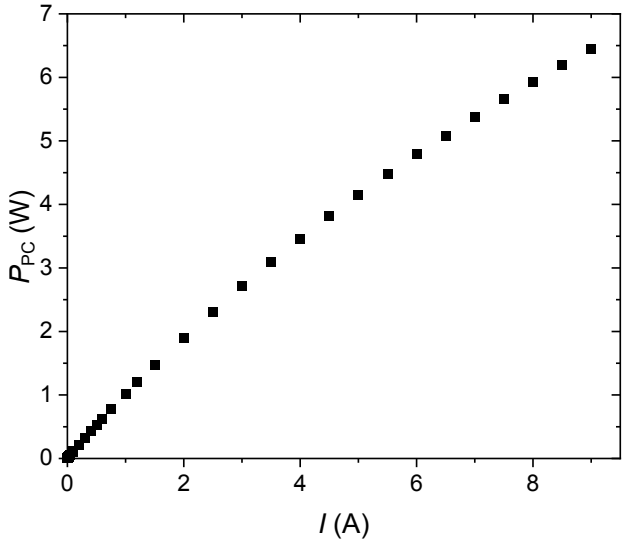

Figure 6.6: Power exciting the sample P_{PC} at certain currents applied to the 445 nm LED.

6.17.3 Steady-State Hydrogen Production Measurements in an Online Reactor

Some of the illumination time- and excitation power density-dependent measurements were conducted in an online reactor setup. The reactor setup was designed and assembled by Sebastian Hentschel (*Mews Research Group, Institut für Physikalische Chemie, Universität Hamburg*). A gas-tight reactor of 8.8 cm path length, 159 mL liquid phase, and 55 mL gas volume was used. The flow-through reactor setup was constantly fed by 10 mL min^{-1} of argon. For the power density-dependent measurements at high power densities (11.8 mW cm^{-2}, 22.8 mW cm^{-2}, 44.5 mW cm^{-2}), the argon flow was directed through the gas phase, whereas for low power densities (12.2 mW cm^{-2}, 9.12 mW cm^{-2}, 6.08 mW cm^{-2}), the argon flow was directed through the liquid phase for preventing the accumulation of hydrogen gas in the liquid. The flow of the carrier gas was controlled by mass flow controllers (Alicat Scientific, M/MC Series). The temperature of the colloidal sample inside the reactor was kept at 20 °C by water cooling (Solid State Cooling Systems, TCube edge). The gas composition was monitored utilizing a quadrupole mass spectrometer (MS; Hiden Analytical, HPR-20 EGA). The software QGA 2 (Hiden Analytical) was used for instrument control, data recording and analysis. The *OD* of the NP suspension was adjusted to $\sim$0.8 inside the reactor of 8.8 cm path length. Before starting the measurement, the setup was purged with argon until the oxygen content reached a constant value ($\sim$2.5 h). After purging, the colloidal photocatalysts were excited by a 445 nm

LED (Thorlabs, SOLIS-445C) and the suspension was rapidly stirred. The collimated LED beam was reduced to a cross section of 9.21 cm^{-2} by a 3D printed aperture. During the steady-state hydrogen production measurement, the *OD* of the colloidal sample was monitored, utilizing a photodiode power sensor (Thorlabs, S120VC) which was equipped with neutral density filters (Thorlabs, NE06A-A and NE13A-A), was connected to a digital console (Thorlabs, PM100D Compact Power and Energy Meter Console), and was placed behind the reactor. All transmitted light was focused onto the senor using a plano-convex lens (Thorlabs, N-BK7 Plano-Convex Lens). The NPs' PL was monitored using an UV/Vis-spectrometer (Ocean Insight, USB4000-UV-VIS) and a fiber collimator and coupler (Thorlabs, PAF-SMA-5-A - FiberPort), which was mounted on the side of the reactor and thus offset to the LED beam path. The MS was calibrated on different concentrations of hydrogen beforehand. An argon hydrogen mixture (2 % hydrogen), which was dynamically diluted using an additional mass flow controller (Alicat Scientific, M/MC Series), was used for calibration. Analogous to the cuvette setup, the power density of the LED beam was calibrated using a power meter sensor (Thorlabs, S425C Thermal Power Sensor Head), the digital console, and the plano-convex lens. The QE_{H_2} was determined online during the experiment ($QE_{H_2,online}$). For calculating the $QE_{H_2,online}$, the *OD* was monitored as described above (assuming no scattering) and the hydrogen production rate was calculated from the determined hydrogen concentration and the gas flow rate. The measurement in the reactor setup was conducted in collaboration with and the hydrogen calibration of the MS and initial data processing was performed by Sebastian Hentschel (*Mews Research Group, Institut für Physikalische Chemie, Universität Hamburg*).

7 Results and Discussion

7.1 Nanoparticle Synthesis

The syntheses described in this section were partly conducted in collaboration with Julia A. Voss and Benedetta S. Feltrin and are part of their internship protocol and bachelor thesis, respectively. The three-step synthesis of the nanophotocatalysts allows for precise adjustment of the dimensions of its functional components (*cf.* **Figure 7.1**).

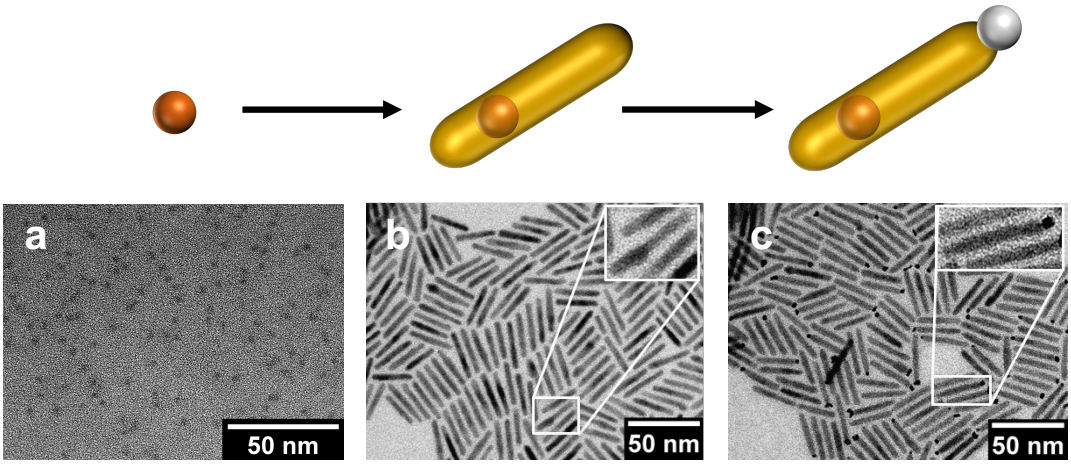

Figure 7.1: Schematic illustration and respective TEM micrographs of the three-step synthesis of Pt-CdSe/CdS nanophotocatalysts, including the synthesis of CdSe NPs (a), CdSe/CdS DRs (b), and Pt-tipped DRs (c). The inset in (b) shows a DR with a pronounced bulb region, the inset in (c) shows a Pt-tipped DR.

7.1.1 CdSe Nanoparticles

Spherical CdSe NPs are synthesized first, which eventually become the CdSe cores within the nanocatalysts. The size of the CdSe NPs was tailored by varying the reaction time and temperature. The lower the temperature of the solution at injection and the faster the cooling, the shorter the growth period and the smaller the NPs obtained. The seeds' diameter was varied from 2.30 nm to

3.34 nm by changing the reaction time from immediate quenching to a reaction time of 15 s, varying the cooling method (water bath or ice bath with 25 vol% acetone) and injection temperature (**Table 7.1**). The size of the NPs was calculated from the absorbance spectra using the calculation by Mulvaney *et al.* (*cf.* Section 6.7, Equation (6.1)). From the smallest to the largest CdSe NPs synthesized, the first excitonic peak of the absorbance spectrum shifts by roughly 70 nm (see **Figure 7.2**a+b), due to the size-dependent quantum confinement and band gap. By adding a second degassing step (*cf.* synthesis protocol in Section 6.2) into the synthesis, even smaller NPs are obtained (Figure 7.2c). The absorbance spectrum shows a narrow peak at 350 nm but no clear excitonic features at around 490 nm. The peak at roughly 350 nm was attributed to magic-sized clusters (MSCs), which are assumed to function as monomer reservoirs during NP growth.[154;155] The occurrence of these MSCs was observed to be highly sensitive to the presence of water, which would initiate a rapid dissolution of the MSCs.[156] The second degassing step apparently decelerates the growth of the NPs by extracting remaining water from the reaction solution, which may be formed during dissolution of the CdO. Integrating a second degassing step into the synthesis protocol thus promises better control of the NPs' size by decreasing the growth rate. According to the peak's position, these MSCs have a diameter of roughly 1.2 nm (Table 7.1), which is consistent with the diameters specified in the literature.[154] However, this calculation should only be considered a rough estimation, since the mathematical modulation of the size-dependent absorption properties by Mulvaney and coworkers only considered NPs of a diameter ≥ 2 nm (*cf.* Section 6.7).[152]

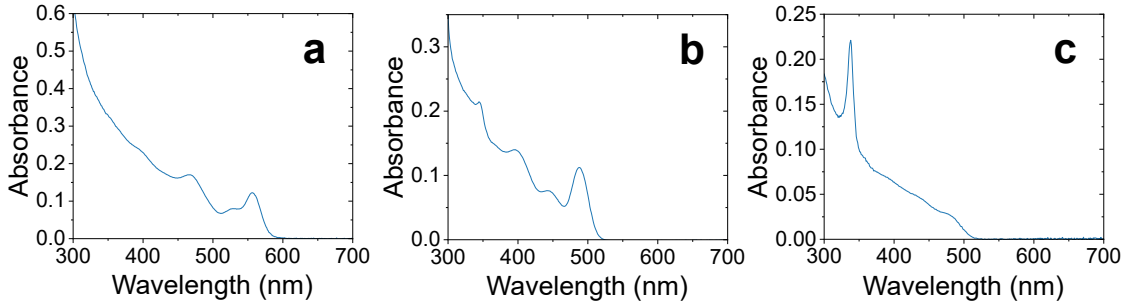

Figure 7.2: Static absorbance spectra of CdSe NPs of different sizes, of arbitrary concentration, with phosphonate ligands in toluene, recorded in a spectrometer with a linear beam path (see Table 7.1 for synthesis parameters). The diameter of the NPs was calculated from the first excitonic peak (3.34 nm (a), 2.30 nm (b)) and the peak at $\sim$ 350 nm (1.15 nm (c)), respectively.

Table 7.1: Synthesis parameters for different batches of CdSe NPs and resulting NP diameters. The diameters were calculated from the samples' absorbance at the first excitonic peak, except for the smallest NPs (1.15 nm), where the MSC peak (see text) at 338 nm is used for this calculation (see Figure 7.2 and Figure A1 for absorbance spectra).

Injection Temperature (°C)	Reaction Time (s)	Cooling Method	Second Degassing	Diameter (nm)
378	0	acetone + ice bath	yes	1.15
378	0	acetone + ice bath	no	2.30
370	0	water bath	no	2.87
374	0	water bath	no	2.95
378	15	acetone + ice bath	no	3.10
383	10	water bath	no	3.34

7.1.2 CdSe/CdS Dot-in-Rods

The second step in synthesizing the nanophotocatalysts is to grow an elongated CdS shell on the CdSe NPs (*cf.* Figure 7.1b). This is implemented by using the latter as seeds to initiate heterogeneous CdS nucleation. The length of the CdS domain was adjusted by varying the amount of CdSe seeds injected, while keeping the amount of Cd and S precursor constant (**Table 7.2**). The DRs' diameter was roughly 4 nm for all batches of DRs. Due to the differences in CdSe core size, the DRs made from the 2.3 nm CdSe seed have a quasi-type II potential profile, while the DRs made from larger cores (2.95 nm and 3.1 nm) exhibit a type I potential profile.[72;73] Therefore, the electronic excited states delocalize into the CdS shell for the former, while they localize at the CdSe core for the latter.[72]

The static absorbance spectra (solid line) and the respective PL peaks (dashed line) of two batches of DRs with similar lengths and diameters but different CdSe core sizes are shown in **Figure 7.3**. Both spectra exhibit the characteristic features known for this semiconductor heterostructure. The pronounced features at 460 nm and 415 nm can be attributed to the 1Σ ($1\sigma_e - 1\sigma_h$) and 1Π ($1\pi_e - 1\pi_h$) excitonic transitions in the CdS domain, respectively.[29;94;100;149] The small shoulder at around 490 nm can be assigned to the excitonic transition in the bulb region of CdS surrounding the CdSe core (see inset in Figure 7.1b and *cf.* Figure 4.9).[76;94;135;136] Since in both batches of DRs the CdS domains have the same diameter, these CdS shell absorption features are identical. The weak absorption feature at roughly 550 nm and 580 nm for the DRs with a small and large core, respectively, can be assigned to the excitonic transition in the CdSe core. The

maximum of the PL spectrum of the CdSe/CdS DRs occurs Stokes-shifted with respect to the CdSe core absorption at around 560 nm and 595 nm, respectively. As the radiative recombination occurs at the CdSe core, the core size determines the emission color. The full width at half maximum (FWHM) of the PL peaks is 30.3 nm ± 0.2 nm and 33.5 nm ± 0.2 nm for the DRs with a small and large core, respectively, indicating a small size distribution in the DRs' diameter.

Table 7.2: Dimensions, aspect ratio, and volume of the synthesized CdSe/CdS DRs, CdSe seed size and injected amount of substance. The injected amount of substance was calculated from the concentration of the seed suspension, which was determined from the absorbance spectra using the calculation by Mulvaney *et al.* (*cf.* Section 6.7, Equation (6.3)).[152] The dimensions of the DRs were determined from TEM micrographs (see Figure A2a-e).

Seed Diameter (nm)	Amount of Substance Seeds (nmol)	Length (nm)	Diameter (nm)	Aspect Ratio	Volume (nm^3)
2.95	51	47.5 ± 4.2	4.0 ± 0.3	12	597
2.95	79	33.9 ± 1.7	4.3 ± 0.3	7.9	492
2.30	55	44.4 ± 2.7	3.8 ± 0.5	12	504
2.30	79	35.3 ± 4.2	4.0 ± 0.4	8.8	444
3.10	55	46.3 ± 5.9	4.1 ± 0.4	11	611

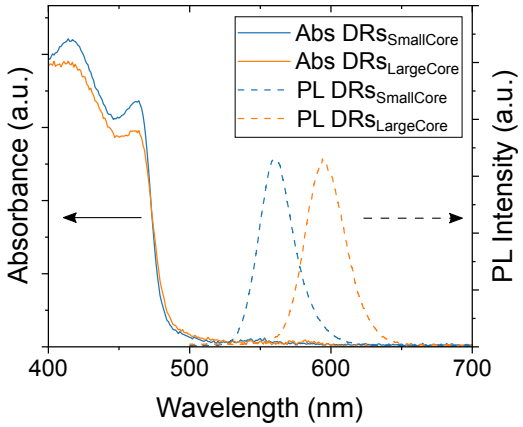

Figure 7.3: Static absorbance and PL spectra of two DR batches of different core size (2.3 nm, blue line and 3.1 nm, orange line) and of arbitrary concentration. The absorbance spectra were recorded in a spectrometer which was equipped with an integrating sphere.

7.1.3 Pt-Tipping

The third and final step in synthesizing the hybrid nanophotocatalysts is to grow cubic (c) Pt tips on the w-CdSe/CdS DRs (*cf.* Figure 7.1c). It was investigated whether the photodeposition or high-temperature synthesis method is best suited for obtaining highly active photocatalysts, having a single Pt domain at the DR's tip opposing the CdSe core. The position and number of Pt domains deposited were determined from TEM micrographs (>200 NPs were evaluated).

Pt Growth *via* Photodeposition

Alivisatos and coworkers reported that photodeposition of Pt onto CdSe/CdS DRs leads to the vast majority of Pt domains growing at the side of the DRs, next to the CdSe core.[86] In reductive photodeposition, the location of metal deposition is dependent on the electrons' localization within the heterostructure (*cf.* Figure 4.11).[91;131] As the electron localization is influenced strongly by the dimensions of the functional components of the heterostructure, it was investigated in this thesis, whether the size of the CdSe core and the length of the CdS rod domain affect the location of Pt deposition. In this context, Pt was photodeposited onto DRs of different geometries, and the location of the Pt domain growth was investigated (**Figure 7.4** and **Table 7.3**). During photodeposition, Pt deposits continuously on the DRs with increasing illumination time (**Figure 7.5**).

Table 7.3: Dimensions of the DRs used for photodepositing Pt, as well as the proportion of Pt domains grown at the DRs' tips, at the sides of the DRs next to the core, and at both tips of the DRs.

Core Diameter (nm)	Rod Length (nm)	Rod Diameter (nm)	Pt Domains at Tip (%)	Pt Domains at Side (%)	Pt Domains at Both Tips (%)
3.1	46	4	8	92	0
2.3	44	4	28	71	1
2.3	35	4	69	29	2

For DRs with a large core and a type I band alignment, the metal deposition occurs mainly next to the core (*cf.* Table 7.3). In DRs with a small core and a quasi-type II heterojunction, a significantly larger proportion of metal domains deposits at the DRs' tips. However, the majority of domains still grow at the sides of the DRs. On the contrary, for short rods with a small core, the majority of metal domains deposit at the DRs' tips. These results confirm that the CdSe core size and CdS rod length indeed influence the location of metal deposition. For DRs with a type I band alignment, the photogenerated electrons transfer into

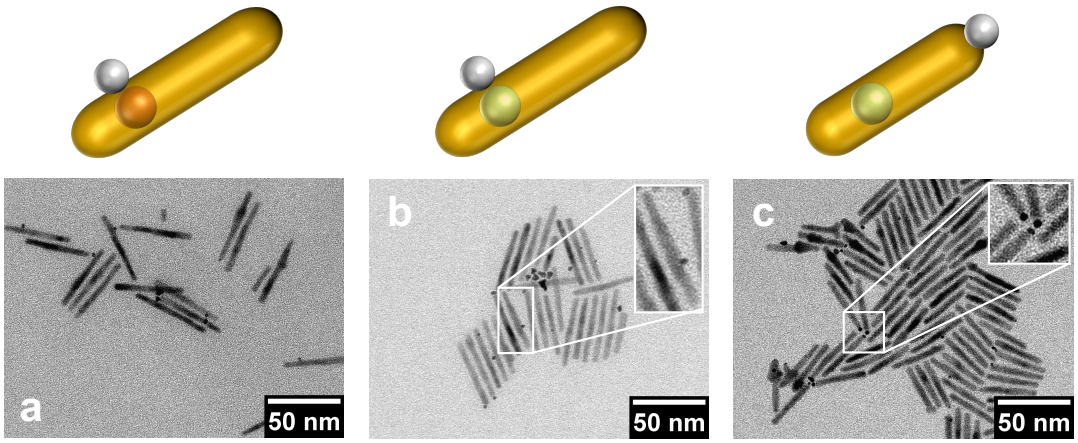

Figure 7.4: Schematic illustrations and TEM micrographs of CdSe/CdS DRs of different core and shell dimensions after photodeposition of Pt domains. For long DRs with large cores (a) nearly all of the domains deposit at the sides of the DRs, for long rods with small cores (b) the majority of the domains grow at the sides and some at the tips, while for short rods with small cores (c) the majority of the domains deposit at the DRs' tips (*cf.* Table 7.3). The insets in (b) and (c) show Pt domains deposited at the side of a DR and at the tips of some DRs, respectively. The schemes depict the most numerous species of the Pt-CdSe/CdS DRs.

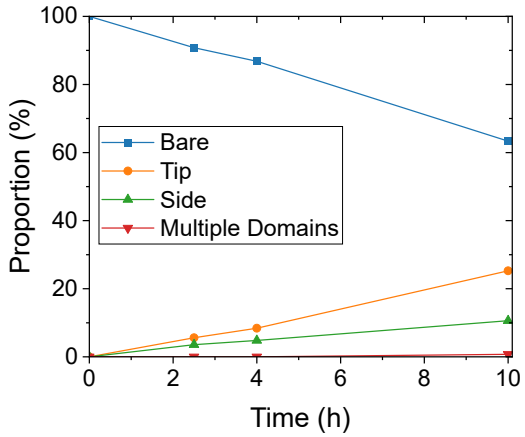

Figure 7.5: Proportion of bare DRs (blue line), DRs with a Pt domain grown at the DR's tip (orange line), side (green line), and both tips of the DR (red line) against the illumination time during photodeposition of Pt. The DRs had a small CdSe core and a short CdS rod domain (*cf.* Table 7.3 for parameters).

the CdSe core, directing metal deposition to occur next to the core. In DRs with a quasi-type II band alignment, the electrons delocalize into the CdS rod domain, and therefore favor metal deposition at the DR's tip. As the number of surface defects, and thus trap states, increases with the length of the rod, the probability of an electron reaching the tip of the DR decreases with increasing length.[100;102]

Hence, the most Pt domains deposit at the DR's tip for short rods with small cores. However, for achieving large photocatalytic efficiencies, a long CdS domain is favored over a short one due to an increased spatial charge separation. Furthermore, even for the short DRs a significant proportion of the Pt domains still deposit next to the CdSe core, again reducing photocatalytic efficiency due to a small spatial charge separation. Nevertheless, regardless of the dimensions of the DRs, almost exclusively single Pt domains deposit on the DRs and hardly any DRs are double-tipped.

Pt Growth *via* High-Temperature Synthesis

The number and size of Pt domains deposited on the DRs by the hot-injection synthesis were controlled by varying the ratio of Pt precursor to DRs or the reaction time. By modifying the ratio of Pt precursor to DRs (0.34 mg nmol^{-1}, 0.88 mg nmol^{-1}, and 1.3 mg nmol^{-1}), DRs with barely any Pt domains on them, with mainly a single Pt tip on the DR's tip, and with multiple Pt domains are obtained, respectively (*cf.* **Figure 7.6**; see Section A1.3 for calculation of DR concentration and Table A2 for introduced amounts of reactants).

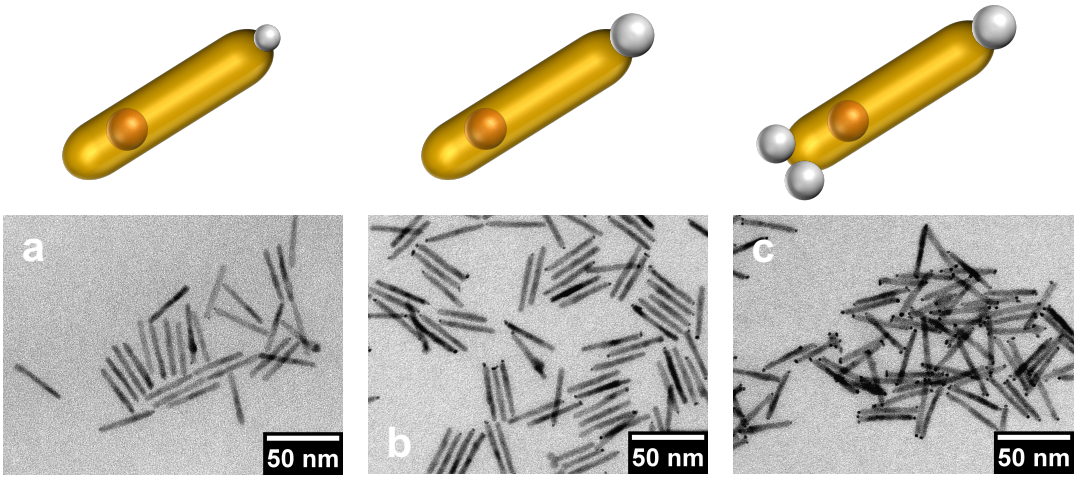

Figure 7.6: Schematic illustrations and TEM micrographs of CdSe/CdS DRs after hot-injection deposition of Pt using a reaction time of five minutes and a ratio of Pt precursor to DR of 0.34 mg nmol^{-1} (a), 0.88 mg nmol^{-1} (b), and 1.3 mg nmol^{-1} (c), respectively. With increasing amount of Pt precursor per DR, more and larger Pt domains grow on the DRs. The schemes depict the most numerous species of the Pt-CdSe/CdS DRs.

The influence of the reaction time was investigated by extracting aliquots during a synthesis. The number and size of deposited domains increase with reaction time (see **Figure 7.7** and **Figure 7.8**). However, with long reaction times (>9 min for this sample), additional Pt domains grow on previously single-tipped DRs

(see Figure 7.7). In contrast to the photodeposition method, the Pt domains rarely grow at the sides of the DRs, but their deposition is directed towards the facets of high reactivity (001) and (00$\bar{1}$) at the tips of the DRs. Pt domain growth on the DRs' sides occurs increasingly on long DRs and on DRs with pronounced bulb regions around the core, probably induced by surface defects (see inset in Figure 7.8d).[100;102]

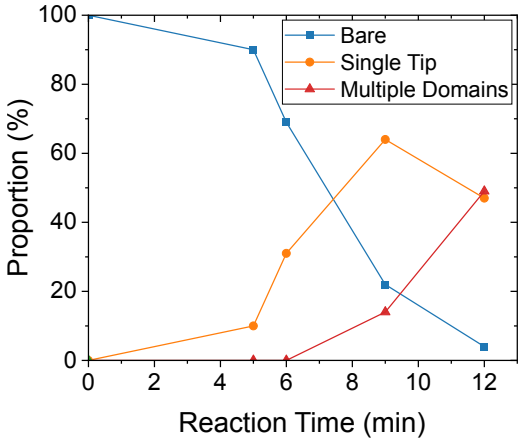

Figure 7.7: Reaction time-dependent proportion of bare DRs, DRs with a single Pt domain at the DRs' tip, and DRs with multiple Pt domains after Pt deposition using a hot-injection synthesis. The determined proportions are listed in Table A3.

Comparing the approaches for Pt deposition *via* photodeposition and hot-injection synthesis, aiming for highly active photocatalysts, hot-injection is more suitable because almost no Pt domain growth occurs next to the core but primarily at the DRs' tips. In the photodeposition approach, the disadvantage of reduced spatial charge separation within the obtained photocatalysts prevails over the advantage of nearly exclusive growth of single tips. Additionally, in the hot-injection approach, the deposition of two Pt tips can be inhibited using a short reaction time, low ratio of Pt precursor to DRs, and a reasonable DR length (<50 nm). For a reaction time of 5 min and a ratio of Pt precursors to DRs of 0.3 mg nmol^{-1} (12 mg Pt precursor and ~ 40 nmol DRs introduced), using 29 nm long DRs with 2.3 nm core size, nearly exclusively single-tipped DRs were obtained: 48 % of the DRs had a single, large Pt tip (tip diameter ≥ 2 nm - right inset **Figure 7.9**a), 24 % had a single, small Pt tip (tip diameter <2 nm - left inset Figure 7.9a), only 1 % had two Pt tips at both ends of the DR, and 27 % had no Pt tip. In the HAADF STEM and HRTEM measurements, it is clearly visible that the deposited domains consist of Pt, having a higher atomic number (Z) than Cd, S, and Se and hence appearing brighter in the dark-field measurement and darker in the HRTEM (Figure 7.9b+c). This batch of Pt-tipped DRs was used to conduct most of the steady-

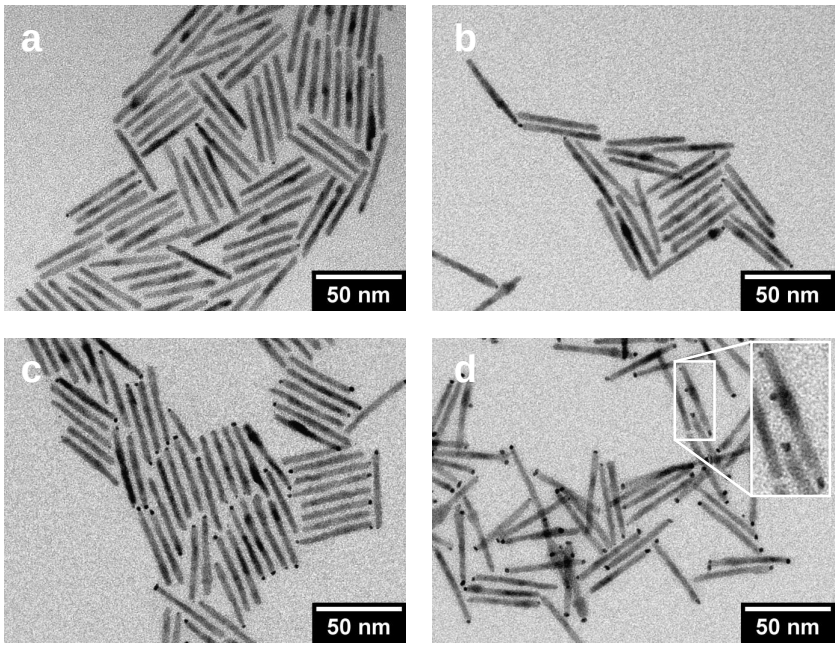

Figure 7.8: TEM micrographs of CdSe/CdS DRs after hot-injection deposition of Pt at a reaction time of 5 min (a), 6 min (b), 9 min (c), and 12 min (d). The inset in (d) shows a DR with Pt domains at each tip and on the bulb region.

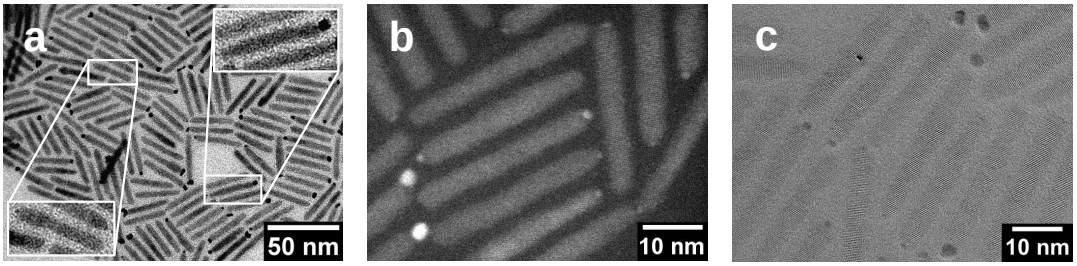

Figure 7.9: TEM (a), HAADF STEM (b), and HRTEM (c) measurements of the Pt-tipped DRs. The left and right inset in (a) show a DR with a single, small and large Pt tip, respectively. Figure modified from Wengler-Rust *et al.*,[103] used under *Creative Commons CC-BY* license.

state H_2 generation, static and time-resolved spectroscopy measurements in the study on the EDA-dependent surface interactions (see Section 7.3 and Section 7.5). The XRD measurement of the Pt-tipped CdSe/CdS DRs validates the wurtzite structure of the CdS domain (**Figure 7.10**). Due to the small volume fraction of the CdSe and Pt domains compared to the CdS domain, both materials are barely visible in the diffractogram. The reflexes that can be assigned to the (100) and (110) planes are especially pronounced due to a texture effect, resulting from the preferred lateral orientation of the anisotropic DRs on the Si substrate.[157;158] Due to the nanoscopic size of the particles and thus the small number of lat-

tice planes, the reflexes are broadened compared to larger (*e.g.* micrometer-sized) particles.[157;158] Diffractograms of bare DRs of different core sizes are shown in Figure A4.

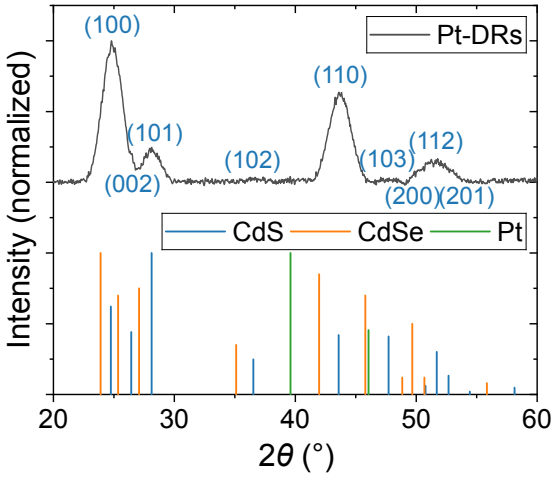

Figure 7.10: XRD measurement of Pt-tipped CdSe/CdS DRs (black line) and the reference diffraction data sets from *The International Centre for Diffraction Data* of w-CdS (*The Powder Diffraction File* (PDF) No. 01-075-1545,[159] blue line), w-CdSe (PDF No. 00-008-0459,[160] orange line) and c-Pt (PDF No. 01-087-0642,[161] green line).

7.2 Ligand Exchange and Phase Transfer to Water

The Pt-tipped DRs were transferred to aqueous suspension by exchanging the native, non-polar, organic ligands to MUA. After ligand exchange, the NPs are still individually dispersed (*cf.* **Figure 7.11**b). A significantly larger quantity of MUA is required to stabilize the bare DRs in water than the Pt-tipped (25 % more MUA added). This finding suggests that the phosphine ligands bind more strongly to the surface of the bare DRs than the OA and OAm ligands to the surface of the Pt-tipped DRs and thus need a larger excess of MUA ligands to be displaced.

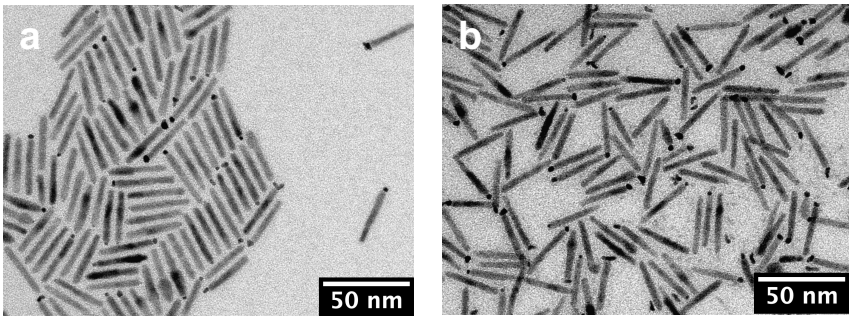

Figure 7.11: TEM micrographs of the Pt-tipped DRs with native, non-polar, organic ligands (a) and after ligand exchange to MUA (b).

7.3 Optical Properties of Bare and Pt-tipped CdSe/CdS Dot-in-Rods

7.3.1 Static Absorbance and Photoluminescence Spectroscopy

The static absorbance spectrum of the Pt-tipped DRs shows an increased absorption compared to the bare DRs (**Figure 7.12**a). This increased absorption is induced by the broad tail of the platinum's surface plasmon (Figure 7.12a, green, dotted line), spanning from the near-infrared to the UV region and superimposing with the DRs' absorption.[86;94;162] The static absorbance spectrum of the Pt

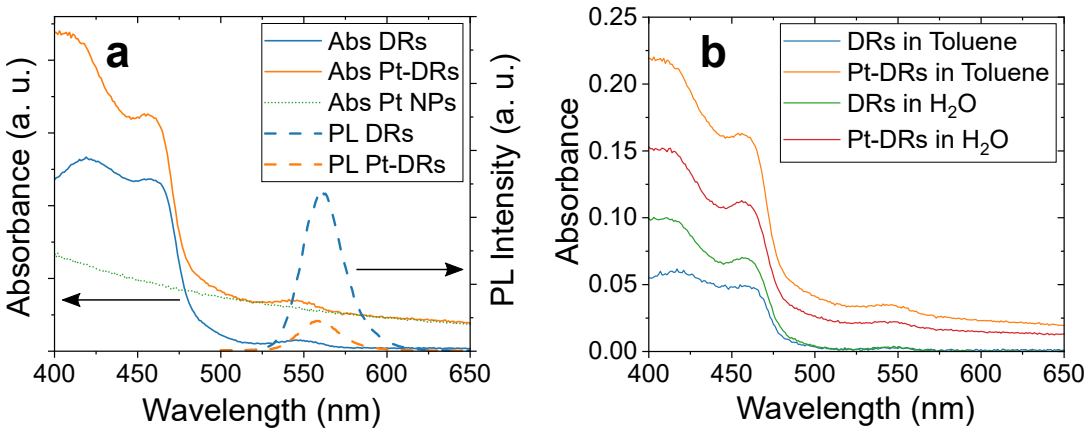

Figure 7.12: Static absorbance spectra of bare DRs (blue line), Pt-tipped DRs (orange line), and Pt NPs (green, dotted line), as well as static PL spectra of bare DRs (blue, dashed line) and Pt-tipped DRs (orange, dashed line) in toluene (a). Static absorbance spectra of bare and Pt-tipped DRs of arbitrary concentration with native, non-polar ligands in toluene and with MUA ligands in water (b). The absorbance spectra were recorded in a spectrometer which was equipped with an integrating sphere. Figure modified from Wengler-Rust *et al.*,[103] used under *Creative Commons CC-BY* license.

NPs was recorded on homonucleated Pt NPs (see **Figure 7.13**). The deposition of Pt tips causes a significant quenching of the DRs' PL (by more than 80 % for the displayed sample, *cf.* **Table 7.4** and Figure 7.12a, dashed blue and orange line; see Section 7.1.3 for sample parameters). This PL quenching results from the transfer of electrons into the Pt tip, impeding radiative charge recombination (*cf.* k_{ET}, k_{rad}, and k_{rad}' in **Figure 7.14**a+b, respectively).

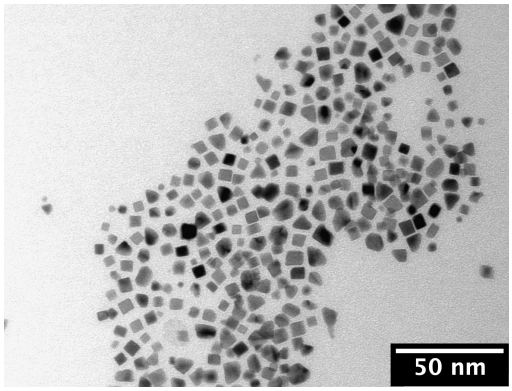

Figure 7.13: TEM micrograph of homonucleated Pt NPs.

Table 7.4: PL quantum yields of bare and Pt-tipped CdSe/CdS DRs in toluene, capped with non-polar, organic ligands (Organics) and in water, capped with MUA ligands (MUA), respectively. The quantum yields were determined in a spectrofluorometer.

Ligand	QY_{PL} (%) for Bare DRs	QY_{PL} (%) for Pt-Tipped DRs
Organics	45	8
MUA	2	3

After exchanging the ligand to MUA and transferring the nanocatalysts into water, the static absorbance does not change (see Figure 7.12b). However, the QY_{PL} is quenched strongly by the ligand exchange (by more than 60 % for the Pt-tipped DRs and more than 90 % for the bare, *cf.* Table 7.4). Analogous to the PL quenching by Pt deposition, the quenching results from charge transfer onto the ligand (k_{MUA} and k_{MUA}' in Figure 7.14a+b, respectively). Due to the large oxidative potential of the thiolate group of the MUA ligand (redox potential of roughly 0.8 V vs NHE),[38;162–164] photogenerated holes can transfer onto it, inhibiting radiative charge recombination. For the MUA-capped, bare DRs, the QY_{PL} is smaller than that of the Pt-tipped DRs. This results possibly from a larger amount of MUA ligands on the bare DRs compared to the Pt-tipped DRs (see above). Additionally, the reduced QY_{PL} could result from an Auger-channel generated by

photoinduced electrons remaining in the DR after hole transfer onto the MUA ligand. In the Pt-tipped DRs, these electrons transfer to the Pt domain. However, as the excitation power during the measurement is low, the impact of this effect should be small.

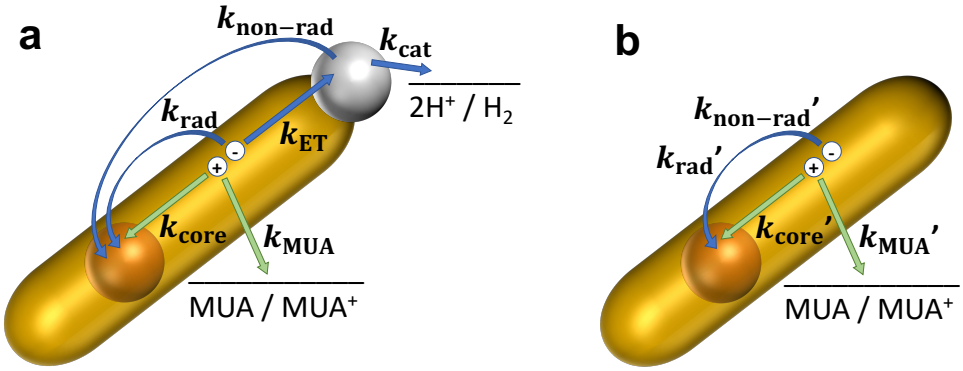

Figure 7.14: Schematic illustration of MUA-capped, Pt-tipped (a) and bare (b) CdSe/CdS DRs, showing the rate constants of charge transfer and recombination channels. The blue arrows indicate electron transfer, the green arrows indicate hole transfer. In the Pt-tipped DRs, the photogenerated holes locate into the CdSe core (k_{core}), while the photogenerated electrons transfer into the Pt tip (k_{ET}). Instead of or after transferring into the core, the holes can be scavenged by the MUA ligand (k_{MUA}). The Pt tip catalyzes hydrogen production after accumulation of electrons (k_{cat}). The photocatalytic activity of the nanohybrid is limited by the competing processes of radiative (k_{rad}) and non-radiative charge recombination ($k_{non-rad}$). Most of the rate constants are significantly influenced by the presence of the Pt tip. In the illustration of the bare DRs (b) these rate constants are therefore marked as k'.

7.3.2 Transient Absorption and Time-Resolved Photoluminescence Spectroscopy on Pt-Tipped CdSe/CdS Dot-in-Rods

TA spectroscopy measurements can be depicted as single differential spectra recorded at the respective delay times, or the kinetics at distinct wavelengths can be plotted (**Figure 7.15**a+b, respectively). Furthermore, the complete TA measurement can be combined in a 3D map (Figure 7.15c). Within such a TA map, the delay time is plotted against the wavelength, while the color indicates the ΔA. The TA map of bare, MUA-capped CdSe/CdS DRs after excitation at 400 nm shows the same features as their static absorbance spectra (*cf.* Figure 7.12). The CdSe core bleach feature is located at $\sim$550 nm, the CdS shell bleach feature at $\sim$460 nm,

and the bulb bleach feature at ∼490 nm. The bleaches recover over time, as can be tracked in the time-dependent change of the spectra or in the respective kinetics (see Figure 7.15a+b, respectively). Investigating the bleach recovery kinetics of distinct features and comparing it to the kinetics of other features enables tracking of the charge carriers' movement and recombination. By combining the measurements of the fs- and ns-TA setup, the kinetics of distinct features can be resolved across a temporal range extending from fs to µs (**Figure 7.16**a+b).

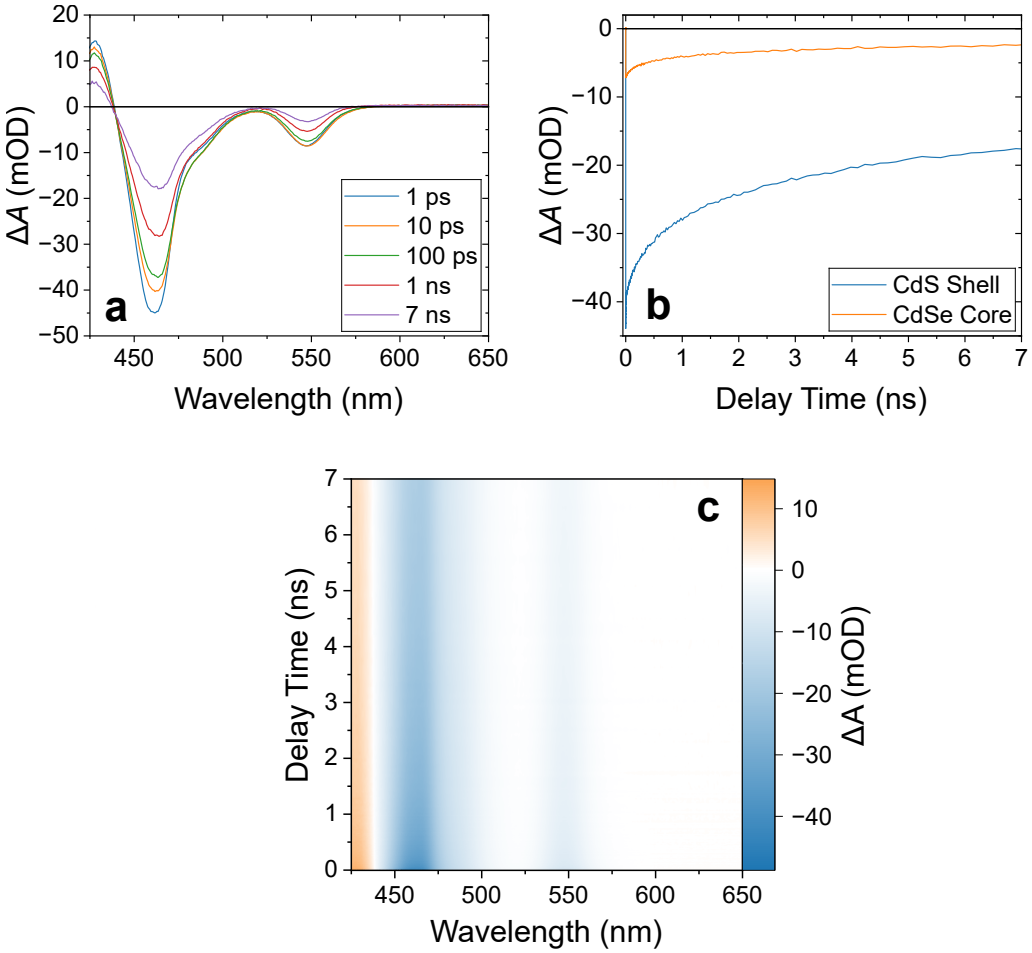

Figure 7.15: TA spectra at different delay times (a), bleach decay kinetics at the CdS shell (466 nm) and CdSe core (548 nm) feature (b), and 3D map of the TA measurement of MUA-capped, bare DRs in water, at 400 nm excitation.

Additional conclusions can be drawn from the radiative recombination of the charge carriers using time-resolved PL spectroscopy. In this section, the movement of the photoinduced charge carriers into the CdSe core, Pt tip, trap states, and onto the MUA ligand are tracked using TA and time-resolved PL spectroscopy, and the time scales on which these processes occur are roughly determined.

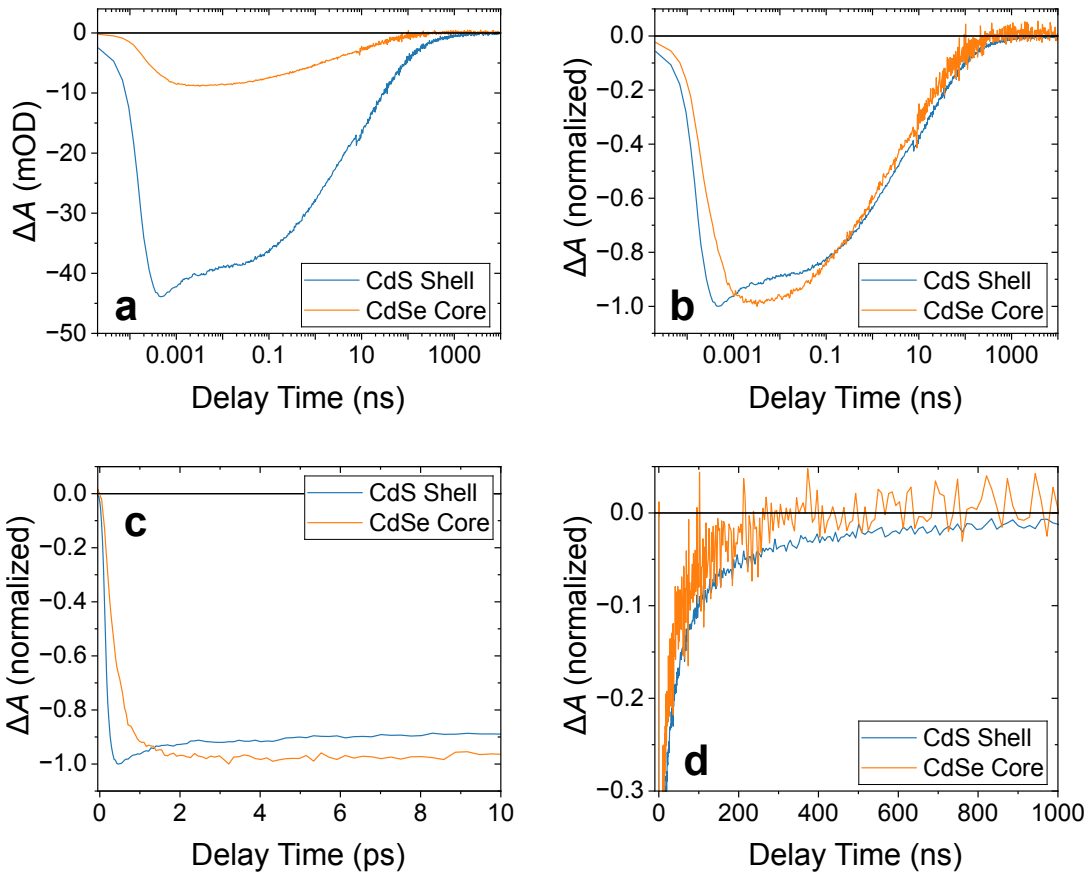

Figure 7.16: Non-normalized (a) and normalized (b-d) TA bleach recovery kinetics, combining fs- and ns-TA measurements for MUA-capped, bare CdSe/CdS DRs in water. The TA kinetics are measured at 400 nm excitation, comparing the CdS shell (466 nm, blue line) and CdSe core (548 nm, orange line) bleach recovery.

Hole Transfer Into the CdSe Core

The rapid transfer of the photogenerated holes into the CdSe core can be investigated by comparing the CdSe core and CdS shell TA bleach emergence of bare CdSe/CdS DRs upon shell excitation (Figure 7.16b+c; $k_{core'}$ in Figure 7.14b). The excitation of the CdS shell induces a rapid rise of the shell bleach, attaining its maximum value after less than one picosecond and promptly recovering thereafter. In contrast, the CdSe core bleach reaches its maximum value only after approximately four picoseconds. The delayed rise of the core bleach feature is caused by the transfer of holes from the shell into the core.[65;101;165] Hence, this hole transfer process apparently proceeds within a few picoseconds.[65] After this hole transfer, the delocalized electrons successively recombine radiatively or non-radiatively with the holes at the core ($k_{rad'}$ and $k_{non-rad'}$ in Figure 7.14b). Therefore, both bleach features recover at a similar rate in the range from 0.1 - 100 ns (Figure 7.16b). However, at larger delay times, the CdSe core bleach recov-

ers completely (after ~300 ns), while a long-lived CdS shell bleach remains (Figure 7.16d). This long-lived bleach feature is probably induced by trapped charge carriers at the NCs' surface.[24;65;76;136]

Electron Transfer Into the Pt Tip

The influence of the Pt tip on the charge movement within the semiconductor can be visualized by comparing the TA bleach kinetics of bare and Pt-tipped DRs. The rapid electron transfer from the semiconductor into the Pt tip leads to an accelerated recovery of the shell bleach for the Pt-tipped DRs (**Figure 7.17**a; k_{ET} in Figure 7.14a).[65;100] Additionally, the initial shell bleach is roughly 25 % smaller for the Pt-tipped DRs (Figure 7.17a). This indicates that some electrons transfer into the tip at a transfer rate beyond the TA setup's time resolution, which is estimated to be approximately 150 -200 fs for the fs-TA setup.[100] Thus, most of the electron transfer into the metal tip occurs within the first few tens of pi-

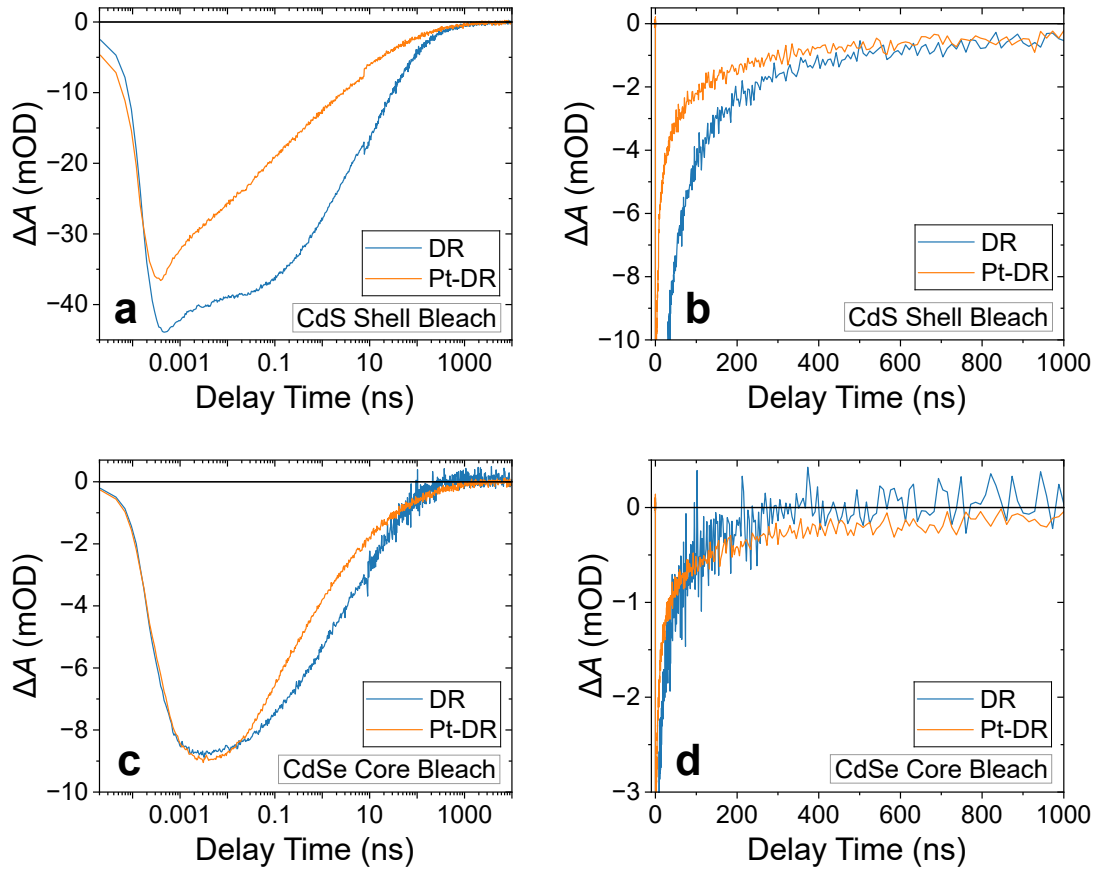

Figure 7.17: TA bleach recovery kinetics of the MUA-capped, bare (blue line) and Pt-tipped (orange line) CdSe/CdS DRs in water, measured at 400 nm excitation, probed at the CdS shell bleach (466 nm) (a+b) and at the CdSe core bleach (548 nm) (c+d), combining fs- and ns-TA measurements.

coseconds, which is consistent with literature reports.[65] Likewise, this electron transfer causes an accelerated recovery of the core bleach as the electrons delocalize within the quasi-type II heterostructure (Figure 7.17c).[65;165] However, at longer delay times, the core bleach recovers faster for the bare DRs than for the Pt-tipped ones (Figure 7.17d).[100] For the bare DRs, the core bleach recovers fully after roughly 300 ns, whereas some bleach remains for the tipped DRs. This long-lived bleach feature is evidently induced by the Pt tip. The transfer of electrons into the Pt tip enables long-lived spatial charge separation, with the holes resting at the core. These holes appear to generate the observed bleach feature. Therefore, the occurrence of this long-lived bleach feature demonstrates that the photogenerated holes indeed contribute to the CdSe core bleach. The shell bleach of the bare and Pt-tipped DRs recovers at a similar rate at longer delay times (Figure 7.17b). Both kinetics show a long-lived bleach feature, which is generated by surface-trapped charges (see above).

Surface-Trapped Holes

Besides influencing the shell kinetic, surface-trapped holes (STHs) generate a photoinduced absorption feature in the red spectral region of the TA spectrum (see **Figure 7.18**a+b).[66;148;149] Upon excitation by the probe pulse, the trapped holes are excited deeper into the VB of the semiconductor, resulting in a positive ΔA. Trap states can result from defect sites, dangling bonds, or polar ligands.[67;68;70;71] The STH feature is significantly larger (larger ΔA) in the presence of MUA ligands at the NPs surface compared to non-polar, organic ligands (Figure 7.18b+c), confirming that the hole-accepting MUA ligands generate additional hole trapping sites. The STH feature occurs within less than a picosecond for both ligands (Figure 7.18c), which is in line with literature reports on hole trapping.[66;76;148] The additional absorption of the MUA-capped compared to the organics-capped NPs recovers within a couple of nanoseconds (Figure 7.18d), and both kinetics recover similarly thereafter (Figure 7.18e). The holes trapped on the MUA ligand thus vanish within nanoseconds, either by (non-radiative) recombination or by detachment of the oxidized MUA ligand.[34;162;166]

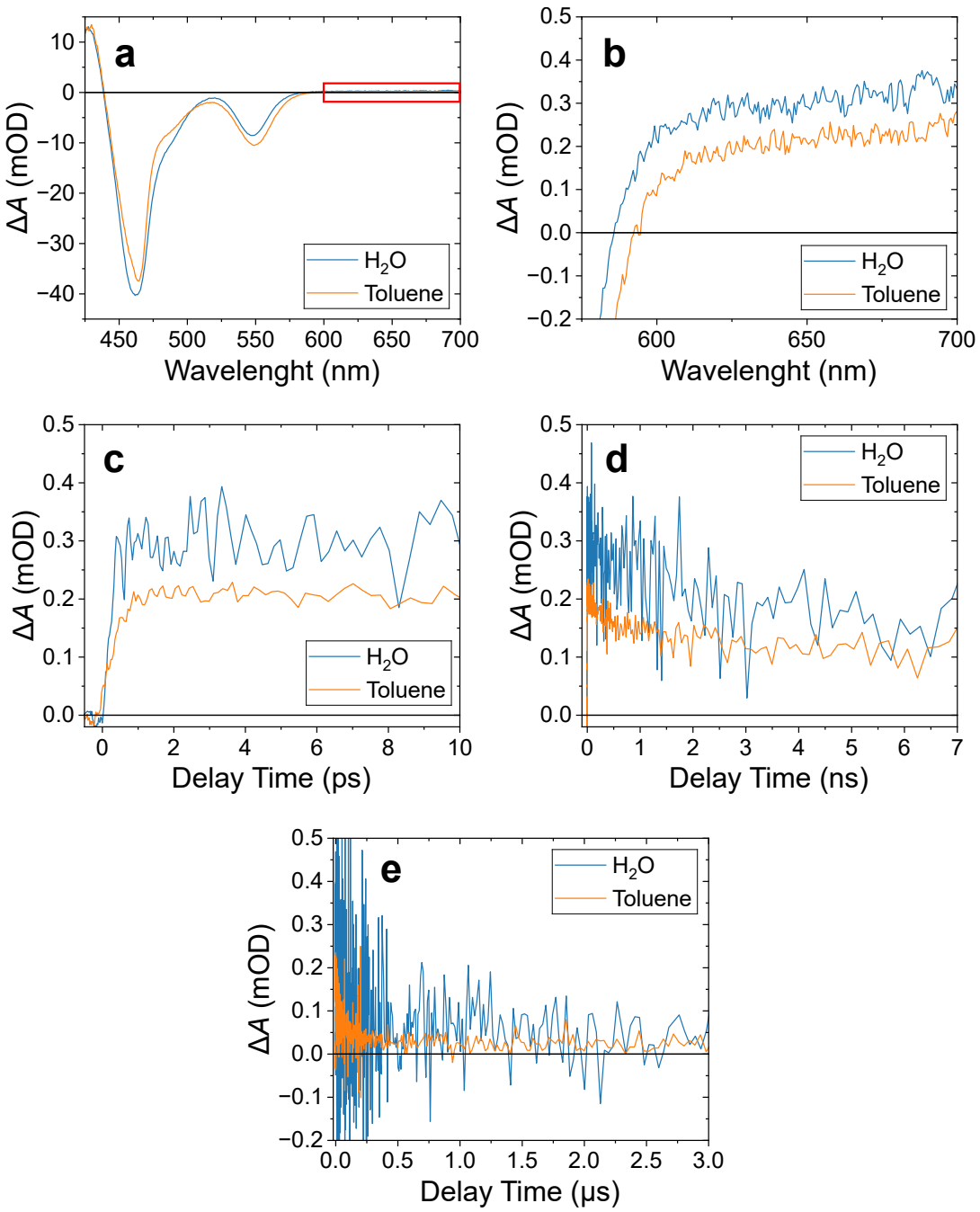

Figure 7.18: TA spectra at 10 ps delay time (a) and averaged over a delay time range from 1 to 10 ps, showing the STH feature (b), TA decay kinetics of the STH feature, averaged in the probe spectral range from 600 to 700 nm (see red box in (a)) at different delay time ranges (c-e). All measurements were conducted at 400 nm excitation, using CdSe/CdS DRs, capped with MUA in water (blue line) and capped with non-polar, organic ligands in toluene (orange line), combining fs- and ns-TA measurements.

Hole Transfer Onto the MUA Ligand

The transfer of the photoinduced holes onto the MUA ligand can additionally be visualized by comparing the TA CdSe core bleach recovery kinetic of the MUA-capped NPs in water with the kinetic of NPs capped with non-polar, organic ligands in toluene (**Figure 7.19**; k_{MUA} and k_{MUA}' in Figure 7.14a+b, respectively). The normalized kinetics are shown in order to neutralize the impact of variations in the NP concentration of the samples. In the presence of the MUA ligand, the bleach recovery is accelerated for both bare and Pt-tipped DRs. This accelerated bleach recovery is likely to be caused by the hole transfer onto the MUA ligand. Additionally, the bleach reaches its maximum for the MUA-capped NPs a few picoseconds earlier than for the NPs capped with hydrophobic ligands. This indicates that some holes transfer onto the MUA ligand directly instead of transferring into the core, resulting in a shortened bleach rise.

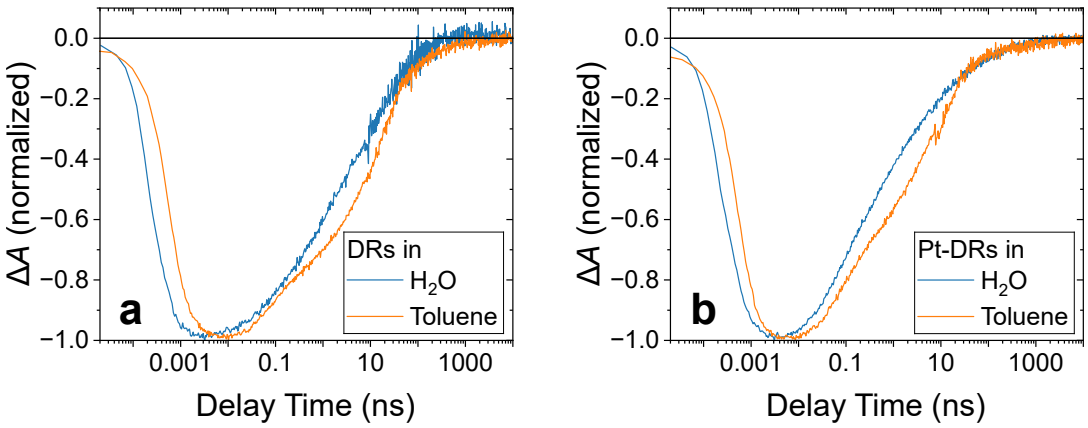

Figure 7.19: TA CdSe core bleach recovery kinetics of bare (a) and Pt-tipped (b) CdSe/CdS DRs, capped with MUA in water (blue line), and capped with non-polar, organic ligands in toluene (orange line). The TA kinetics were measured at 400 nm excitation and probed at the CdSe core bleach (548 nm), combining fs- and ns-TA measurements.

Charge-Separated State Feature

In the Pt-CdSe/CdS nanocatalyst, the charge separation can be visualized by the so-called charge-separated state (CSS) feature. The CSS feature results from a Stark effect-induced shift of the CdS exciton transition and occurs red-shifted from the CdS shell bleach.[29;65;94;148;149;162;167] The Stark effect is generated by the electric field between the spatially separated electron at the Pt tip and the hole in the semiconductor domain. As the photoinduced absorption feature (positive ΔA) occurs red-shifted from the CdS shell bleach, it spectrally overlaps with the bulb region's bleach (negative ΔA; *cf.* Section 7.3.2 for bulb bleach location).

The extent of the bulb bleach varies between batches of NPs, since the absorption of the bulb region depends on the DRs' shape and composition. Additionally, the number and size of Pt tips influence the formation of the CSS feature.[29] Therefore, the occurrence of the CSS feature is dependent on the NPs' parameters, and it does not occur as a discernible feature of positive ΔA for every batch of NPs. Comparing the TA spectra of MUA-capped, bare and Pt-tipped DRs in water (see Section A2 for sample parameters), the CSS feature arises as a positive ΔA after roughly 7 ns (**Figure 7.20**b). However, the shoulder that eventually develops into the positive feature emerges already after 1 ps, which is consistent with the rapid electron transfer into the Pt tip (*cf.* Figure 7.20a).[65]

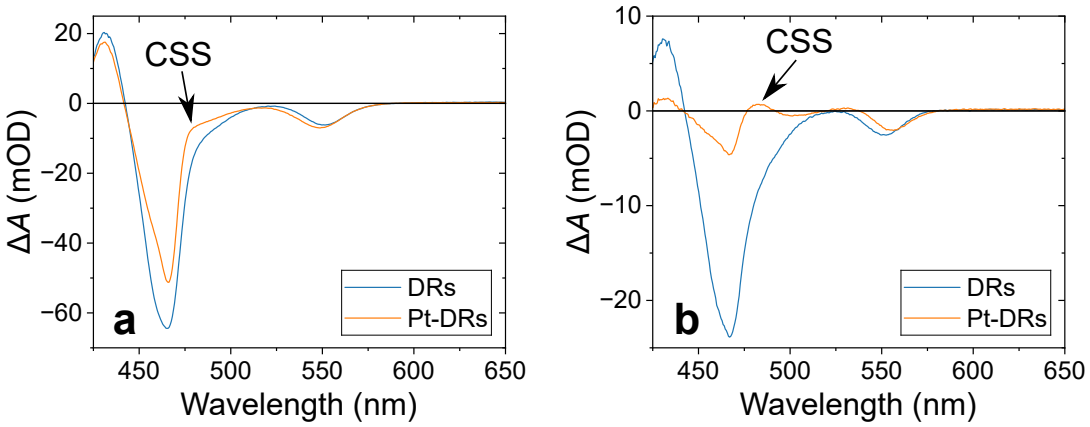

Figure 7.20: TA spectra at 1 ps (a) and 7 ns (b) delay time of MUA-capped, bare (blue line) and Pt-tipped (orange line) CdSe/CdS DRs in water, at 400 nm excitation. The shoulder, that eventually develops into a CSS feature of positive ΔA is already visible at 1 ps for the Pt-tipped DRs. Figure modified from Wengler-Rust *et al.*,[103] used under *Creative Commons CC-BY* license.

Time-Resolved Photoluminescence Spectroscopy

Analogous to the static PL, the time-resolved PL decay kinetic is significantly influenced by the Pt deposition and ligand exchange (see **Figure 7.21**a). Similar to the QY_{PL} (see Table 7.4), the average PL lifetime is considerably reduced by Pt deposition (reduced by $\sim$50 % for the NPs in toluene, see **Table 7.5**; *cf.* k_{rad} and k_{rad}' in Figure 7.14a+b, respectively) and ligand exchange (reduced by $\sim$55 % for the bare DRs). In line with the QY_{PL}, τ_{PL} increases by Pt-tipping for the MUA-capped NPs in water. Unexpectedly, the determined PL lifetime for the MUA-capped, Pt-tipped DRs in water is larger than for the Pt-tipped DRs in toluene and for the bare DRs in water. This is probably caused by the intensity-weighted average emphasizing long decay times, resulting in large variations in the deter-

mined average PL decay times, even though the PL kinetics decay similarly (*cf.* Figure 7.21a).

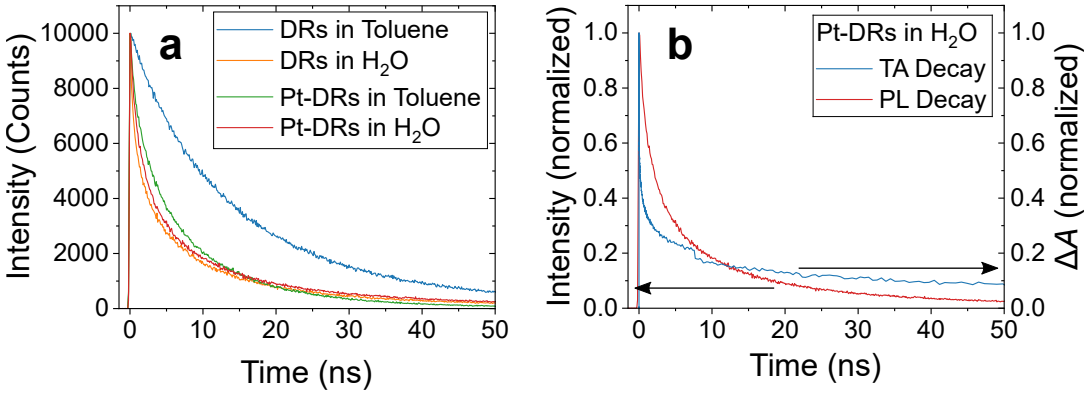

Figure 7.21: Normalized time-resolved PL decay of bare and Pt-tipped CdSe/CdS DRs, capped with MUA or non-polar, organic ligands in water or toluene, respectively (a), and TA CdS shell (466 nm) bleach recovery and PL decay kinetics for MUA-capped, Pt-tipped CdSe/CdS DRs in water (b). The TA kinetics are measured at 400 nm excitation, combining fs- and ns-TA measurements.

Table 7.5: Intensity-weighted average PL lifetimes of bare and Pt-tipped CdSe/CdS DRs in toluene, capped with non-polar, organic ligands and in water, capped with MUA ligands. The fitting parameters are listed in Table A4 and Table A5.

Solvent	τ_{PL} (ns) for Bare DRs	τ_{PL} (ns) for Pt-Tipped DRs
Toluene	23	12
H_2O	10	15

The time-resolved PL decay kinetic is recorded solely from radiative recombination of the photogenerated charge carriers, whereas in the TA measurement, contrast is additionally generated by charge carriers, which recombine non-radiatively. The related non-radiative decay channels have an influence on the PL kinetic (*cf.* Equation (4.10)) but do not contribute to the measured signal directly. For the MUA-capped, Pt-tipped DRs in water, the TA CdS shell bleach initially decays significantly faster than the PL (first ns) and later more slowly (>20 ns) than the PL kinetic (Figure 7.21b). This is likely to be caused by the fast electron transfer into the Pt tip and the slow, non-radiative recombination of trapped charge carriers, which proceed faster and slower than the radiative recombination, respectively, and both are resolved in the TA measurement. As the signal is created differently in TA and PL spectroscopy, these differences in kinetics should only be related qualitatively.

7.3.3 Pt Amount-Dependent Charge Carrier Dynamics

The influence of the number and size of Pt domains on the electron transfer rate was studied. The charge carrier dynamics, the PL lifetime, and QY_{PL} of four samples with different amounts of Pt deposited on the DRs were investigated in this context. The bare DRs (see **Figure 7.22**a) were compared to Pt-tipped DRs with tiny (1-2 nm) and mostly single tips (Pt-DRs$_{Small}$, see Figure 7.22b), Pt-tipped DRs with mostly two medium (2-3 nm) tips (Pt-DRs$_{Medium}$, see Figure 7.22c), and Pt-tipped DRs with at least two, mostly large (3-4 nm) tips and some homonucleated Pt NPs (Pt-DRs$_{Large}$, see Figure 7.22d). The DR batch used in this study had a core size of 2.95 nm and therefore a type I potential profile, favoring localization of the photogenerated electrons into the core. In order to exclude the influence of the reductive MUA ligand and focus on the electron dynamics, the NPs were capped with organic, non-polar ligands and dispersed in toluene.

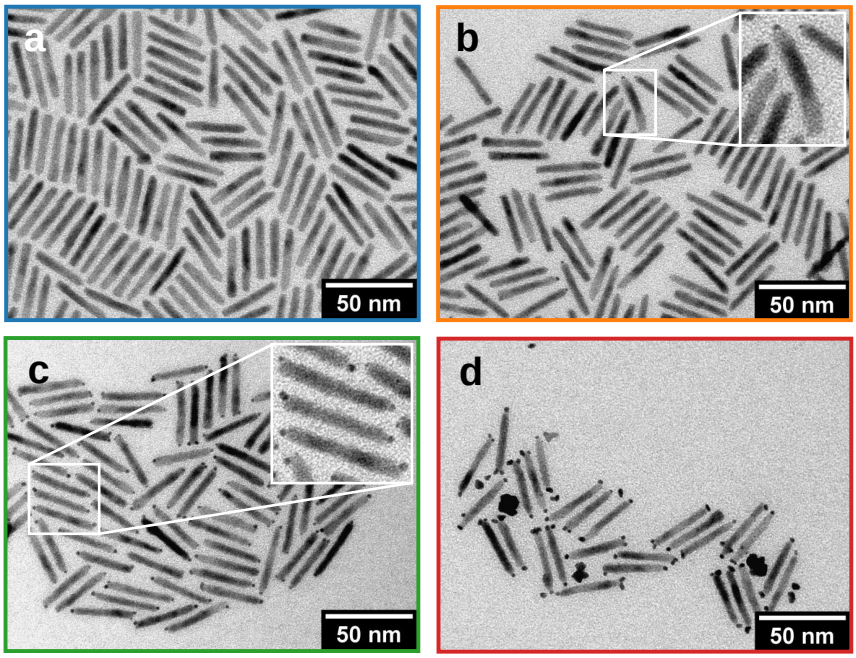

Figure 7.22: TEM micrographs of bare DRs (a), Pt-tipped DRs with tiny (1-2 nm) and mostly single tips (Pt-DRs$_{Small}$) (b), Pt-tipped DRs with mostly two medium (2-3 nm) tips (Pt-DRs$_{Medium}$) (c), and Pt-tipped DRs with at least two, mostly large (3-4 nm) tips and some homonucleated Pt NPs (Pt-DRs$_{Large}$) (d). The colors of the frames around the figures match the color code in Figure 7.23.

The TA bleach recovery kinetics at the CdS shell and the CdSe core feature and the time-resolved PL kinetics are shown in **Figure 7.23**. The PL decay kinetics were fitted with multiexponential decay functions (see Table A6 for fitting param-

eters), and the intensity-weighted PL lifetimes were calculated (**Table 7.6**). The TA bleach kinetics recover faster with an increasing amount of Pt deposited on the DRs (see Figure 7.23a-d). These accelerated kinetics probably result from an increased electron transfer rate into the Pt domains of larger sizes and numbers.

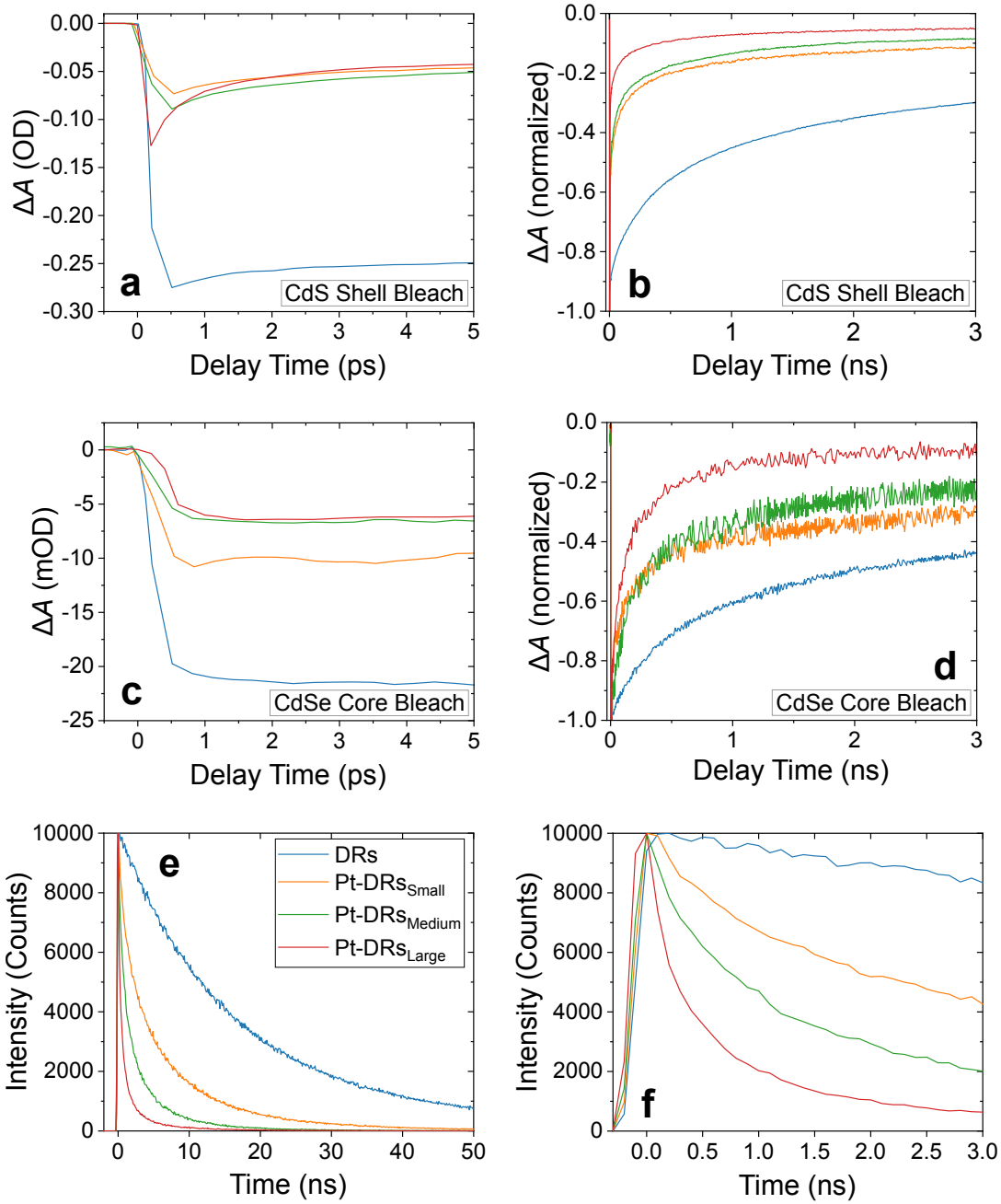

Figure 7.23: TA bleach decay kinetics probed at the CdS shell bleach (465 nm) (a+b) and at the CdSe core bleach (590 nm) (c+d), non-normalized (a+c) and normalized (b+d), and PL decay kinetics (e+f) of CdSe/CdS DRs with Pt domains of different sizes and numbers (see color code in (e)), capped with non-polar, organic ligands in toluene, at 450 nm excitation.

Table 7.6: Intensity-weighted τ_{PL} and QY_{PL} of bare and Pt-tipped CdSe/CdS DRs, with Pt domains of different sizes and numbers, capped with organic, non-polar ligands in toluene. The average decay times were calculated from the fitting parameters of the PL decay (Table A6). The quantum yields were determined relative to coumarin 153 (*cf.* Section A4 for PL spectra and details on calculation).

Batch	τ_{PL} (ns)	QY_{PL} (%)
DRs	22.2	27
Pt-DRs$_{Small}$	8.31	3.1
Pt-DRs$_{Medium}$	3.46	0.69
Pt-DRs$_{Large}$	1.33	0.042

With increasing Pt domain size, the Coulomb repulsion between electrons is reduced, allowing more electrons to transfer into one Pt domain and thus favoring fast electron transfer.[29] Additionally, an increasing number of Pt domains accelerates electron transfer.[27] Interestingly, the PL kinetics likewise decay faster with increasing Pt amount deposited on the DRs (see Figure 7.23e+f and Table 7.6). Thus, metal deposition does not induce static quenching by extinguishing the individual DR's PL completely (*cf.* **Figure 7.24**a). Instead, each tipped DR emits residual PL with a reduced PL lifetime (*cf.* Figure 7.24b). This reduced PL lifetime results from the increased electron transfer rate onto the Pt domain with increasing Pt amount (*cf.* Equation (4.16)). The QY_{PL} decreases significantly faster with increasing Pt amount than the PL lifetime (*cf.* Table 7.6). This leads to an exponential behavior of $QY_{PL_0} \cdot QY_{PL}^{-1}$ in the Stern-Volmer-plot, indicating that static and dynamic quenching occur simultaneously (*cf.* **Figure 7.25**). However, it must

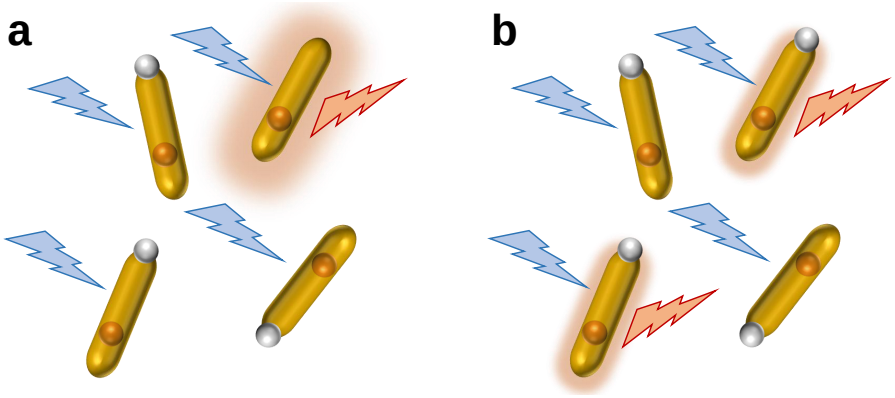

Figure 7.24: Scheme illustrating the static (a) or dynamic (b) quenching of the Pt-tipped DRs. In the case of static quenching, the PL of the individual DRs is extinguished completely by the Pt tips and the observed PL originates from remaining bare DRs. On the contrary, in the case of dynamic quenching, the Pt-tipped DRs emit residual PL with a reduced PL lifetime.

be considered that the concentration of quenchers does not change gradually between the batches, but that the size and number of quenchers per NP varies. Besides, the Pt-DR batch with the largest amount of Pt introduced (Pt-DRs$_{\text{Large}}$) contained large homonucleated NPs, while in all the other batches, the Pt was only deposited on the DRs. Thus, not all batches contain the same species of quencher as assumed in the Stern-Volmer-plot. The displayed Stern-Volmer-plot should therefore just be considered an estimation for illustrating the relation of QY_{PL} and τ_{PL} to the Pt amount. Nevertheless, the results suggest that PL quenching by deposition of noble metal on semiconductor NPs can be described best as a combination of static and dynamic PL quenching.

The initial TA bleach varies for the bare and different Pt-tipped DRs (*cf.* Figure 7.23a+c). A fraction of the photogenerated electrons transfers into the Pt domains faster than the time resolution of the TA setup, leading to a smaller initial bleach for all tipped DRs compared to bare (see above). The batch containing the largest amount of Pt (Pt-DRs$_{\text{Large}}$) has the largest initial shell bleach of all tipped samples but the smallest initial core bleach, and *vice versa* for the batch with the smallest amount of Pt in it (Pt-DRs$_{\text{Small}}$). This illustrates the competition between electron transfer into the core of this type I heterosystem and into the Pt domains. The larger the number and size of Pt domains on each DR, the fewer electrons transfer into the core.

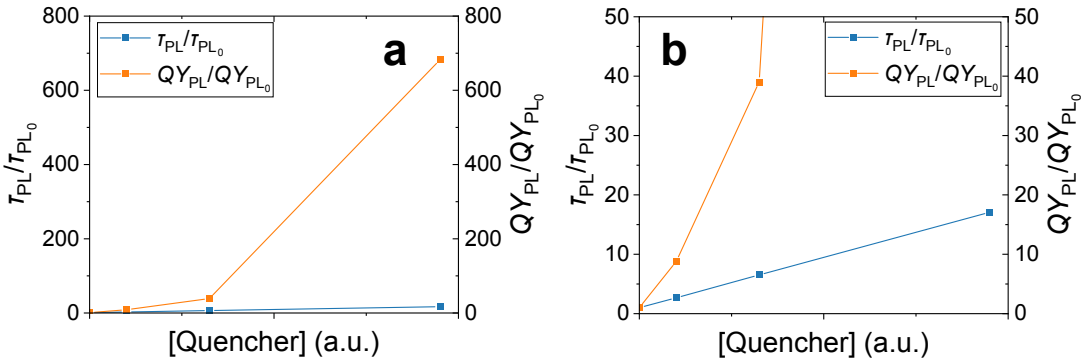

Figure 7.25: Stern-Volmer-Plot of the Pt amount-dependent PL lifetime and quantum yield. The quencher concentration, which equals the Pt amount, was estimated by assuming a linear relation to $\tau_{\text{PL}_0} \cdot \tau_{\text{PL}}^{-1}$.

7.4 Influence of the Dimensions of the Functional Components of the Photocatalyst on the Hydrogen Evolution Efficiencies

The influence of the length of the CdS domain, the CdSe core size, and the number of tips on the QE_{H_2} was investigated. In line with literature reports, the largest QE_{H_2} was obtained for long CdS rods with small CdSe cores (see **Figure 7.26**, **Figure 7.27**, and **Table 7.7**).[26;32] The number of Pt tips deposited on the DRs was not uniform for all investigated samples. It was shown in literature that single-tipped DRs achieve a larger QE_{H_2} than double-tipped.[27;28] Therefore, the difference in QE_{H_2} should be even larger for catalysts of different core sizes but with the same amount of Pt tips (indicated by the dashed arrow in Figure 7.26).

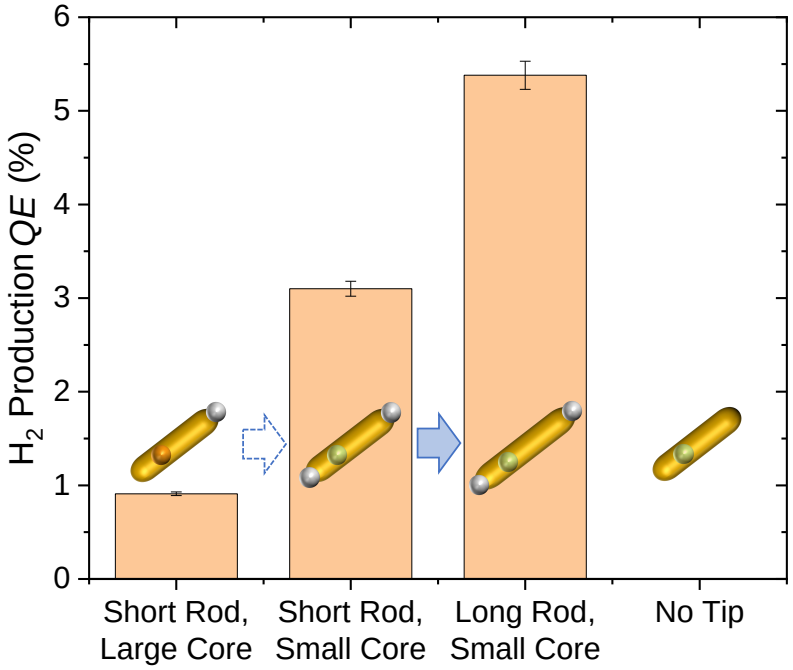

Figure 7.26: Hydrogen production quantum efficiencies for MUA-capped, Pt-tipped and bare CdSe/CdS DRs of different CdSe core size, CdS rod length, and number of tips in water, in the presence of IPA (see Table 7.7 for NP parameters and Figure A7 for hydrogen generation measurements).

Additionally, steady-state hydrogen production measurements were conducted on bare DRs with small CdSe cores in the presence of IPA. For the bare DRs, no hydrogen evolved during illumination for 3 h.[1] These results prove that the Pt

[1] Even in the presence of 1 M KOH in water and 10 vol% IPA, no hydrogen was produced by the bare DRs within 3 h, even though the hydroxide & alcohol mixture is a highly active EDA system (*cf.* Figure 7.34).

tip is of crucial importance for obtaining hydrogen production due to its catalytic activity and by improving spatial charge separation.

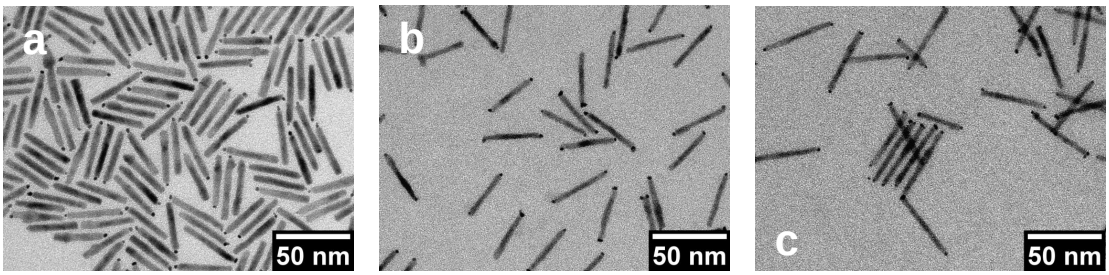

Figure 7.27: TEM micrographs of Pt-tipped CdSe/CdS DRs of different dimensions, which were used for investigating the influence of core size and rod length on the photocatalytic activity.

Table 7.7: Quantum efficiencies in hydrogen production obtained for Pt-tipped and bare CdSe/CdS DRs of different CdS length and CdSe core size, as well as number of Pt tips (*cf.* Figure 7.27), using IPA as an EDA.

Type of NPs	Core Diameter (nm)	Rod Length (nm)	Rod Diameter (nm)	Average Number of Pt Tips per DR	QE_{H_2} (%)
Pt-DRs	3.0	34	4	1	0.91 ± 0.02
Pt-DRs	2.3	35	4	2	3.1 ± 0.1
Pt-DRs	2.3	44	4	2	5.4 ± 0.2
DRs	2.3	29	4	0	0.0 ± 0.0

7.5 Electron Donating Agent-Specific Surface Interactions that Promote the Photocatalytic Activity of Nanohybrids

In a comprehensive study, the impact of the introduced EDA on the photocatalytic activity, charge carrier dynamics, and colloidal stability of the nanohybrids was investigated. Typical concentrations of EDAs were added to the MUA-capped, Pt-tipped CdSe/CdS DRs in water.[2] [32;34–36;38] Additionally, as a point of reference, the performance of the colloidal nanocatalysts was studied in the absence of any additional EDA. To exclude any potential influence of varying NP

[2] For the alcoholic EDAs MeOH, EtOH, and IPA the concentration of the EDA was 10 vol%, while for sodium sulfite and for the mixture of sodium sulfide & sodium sulfite it was 0.1 M each. For the mixtures of hydroxide & alcohol, a 1 M KOH solution in water was combined with 10 vol% MeOH and 10 vol% IPA, respectively (KOH & IPA and KOH & MeOH).

parameters, all measurements displayed in this section were conducted using the same batch of NPs unless otherwise stated (a batch of nearly exclusively single-tipped DRs was used; see description on the batch in Section 7.1.3).

7.5.1 Optical Properties and Colloidal Stability of Pt-CdSe/CdS Nanophotocatalysts in the Presence of Electron Donating Agents

In **Figure 7.28**a+b, the static absorbance spectra of the Pt-tipped CdSe/CdS DRs are shown, recorded in a spectrometer equipped with an integrating sphere and a linear beam path, respectively. The absorbance spectra recorded employing an integrating sphere are very similar, regardless of the EDA added. On the contrary,

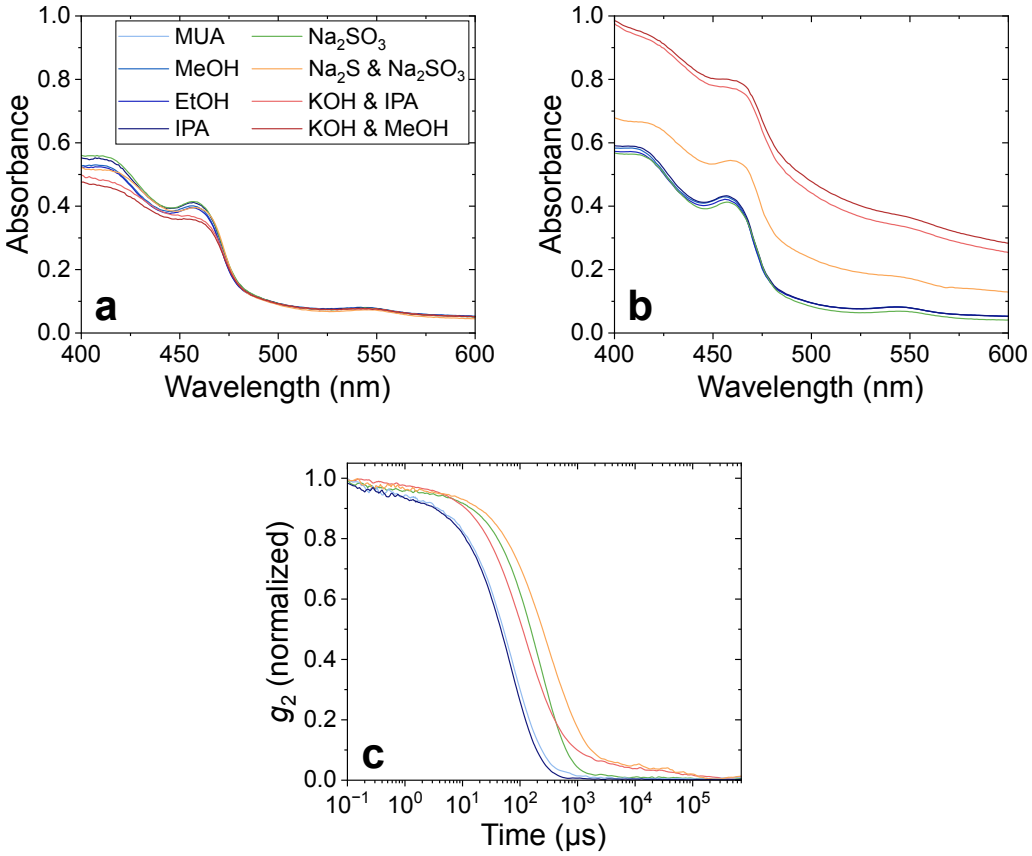

Figure 7.28: Static absorbance spectra (a+b) and normalized autocorrelation functions $g_2(q,\tau)$ (c) of MUA-capped, Pt-CdSe/CdS DRs in water after adding different EDAs (see color code in (a)). The absorbance spectra were recorded in a spectrometer which was equipped with an integrating sphere (a) and with a linear beam path (b), respectively. The normalized autocorrelation functions were recorded by DLS measurements. Figure modified from Wengler-Rust *et al.*,[103] used under *Creative Commons CC-BY* license.

the absorbance spectra recorded in the spectrometer with a linear beam path are significantly increased over the whole spectral region in the presence of the sulfide & sulfite mixture, as well as the mixtures of KOH & alcohol as EDAs. This rise in absorbance can be attributed to an increased light scattering by the colloidal NPs in the presence of sulfide and hydroxide, which is also evident by visual examination of the suspensions (**Figure 7.29** and **Figure 7.30**). Additionally, the NPs are colloidally stable in the presence of the alcoholic EDAs and sulfite for several days, whereas after adding the hydroxide & alcohol EDA mixtures or the sulfide & sulfite mixture, the NPs aggregate and precipitate within hours without stirring (*cf.* **Figure 7.31**).

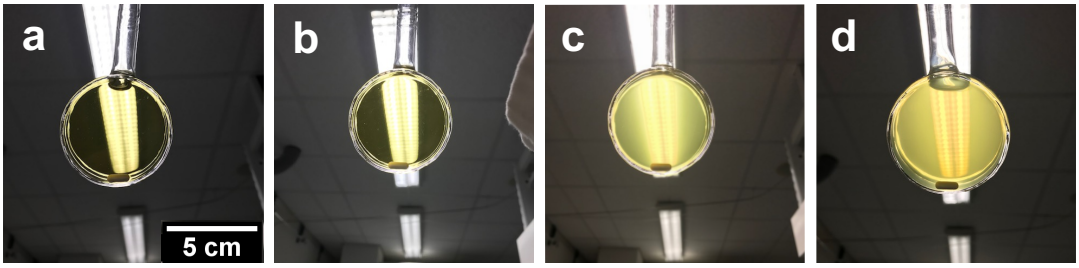

Figure 7.29: Photos of MUA-capped Pt-CdSe/CdS DRs in water with MeOH (a), Na_2SO_3 (b), Na_2S & Na_2SO_3 (c), and KOH & MeOH (d) as EDAs added in the quartz-glass cuvette right before illumination. The suspensions scatter light in the presence of sulfide and hydroxide due to EDA-induced agglomeration of the NPs. An approximate scale bar is shown in (a). Figure modified from Wengler-Rust *et al.*,[103] used under *Creative Commons CC-BY* license.

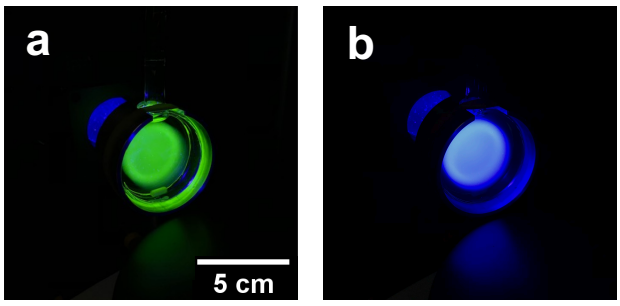

Figure 7.30: Photos of MUA-capped Pt-CdSe/CdS DRs in water with MeOH (a) and a mixture of Na_2S & Na_2SO_3 (b) as EDAs added in the quartz-glass cuvette under illumination during steady-state hydrogen production measurements. In the presence of the alcohol, the NPs emit green light, whereas the agglomerated NPs in the presence of sulfide only scatter the blue excitation light. An approximate scale bar is shown in (a). Figure modified from Wengler-Rust *et al.*,[103] used under *Creative Commons CC-BY* license.

Figure 7.31: Photo of colloidal MUA-capped Pt-CdSe/CdS DRs in water in the presence of IPA, a mixture of KOH & IPA, EtOH, and a mixture of sulfide & sulfite (from left to right). While the NPs are colloidally stable for weeks in the presence of the alcoholic EDAs, they precipitate within hours after introducing the hydroxide & alcohol mixture or the sulfide & sulfite mixture.

The autocorrelation functions recorded from DLS measurements confirm large variations of the hydrodynamic radii after exposure to the different EDAs (Figure 7.28c).[3] The exposure to the alcoholic EDA IPA does not alter the hydrodynamic radii. In contrast, following exposure to hydroxide and sulfide, a second plateau emerges at lag times >1 ms in the autocorrelation function, indicating the existence of large aggregates. These agglomerates are also visible in TEM (**Figure 7.32**). Thus, even a short exposure to sulfide and hydroxide appears to diminish the colloidal stability of the NPs irreversibly, impeding the dissolution of the aggregates after precipitation and redispersion. These observations indicate that the hydroxide and sulfide interact with the surface of the NPs, potentially by attaching to it and displacing the MUA ligand. As previously demonstrated, hydroxides indeed attach to the surface of NPs, forming cadmium hydroxide at high pH.[169–171] Likewise, sulfide anions can attach to the CdS surface, too.[172–176] Moreover, the autocorrelation function shifts to larger lag times after exposure to sulfite, sulfide, and hydroxide, suggesting growth of the NPs' hydrodynamic radii. This shift is most likely caused by the accumulation of salt ions in the NPs' solvation shell, resulting in a growth of the latter and promoting electrostatic aggregation of the NPs.[177–180] Furthermore, the NP aggregation in the presence of the surface-active hydroxide and sulfide induces a bathochromic shift in the the static absorbance spectra (see Figure 7.28a+b and Figure A9 for magnified plot) and in the PL spectra (**Figure 7.33**). Besides, the absorption bands are less pro-

[3] In order to equalize the viscosity of the solvent for the DLS measurements,[168] the MUA-capped Pt-DRs were exposed to the different classes of EDAs for 15 min while stirring, followed by precipitation and redispersion of the NPs in water. For the MUA-sample, the same volume of water was added instead of the EDA solution, in order to account for potential ligand loss by dilution as well as during precipitation and redispersion.

nounced after the addition of the sulfide & sulfite mixture or hydroxide & alcohol mixtures (*cf.* Figure 7.28a+b), which is likely attributed to a change in the NPs dielectric environment.[171]

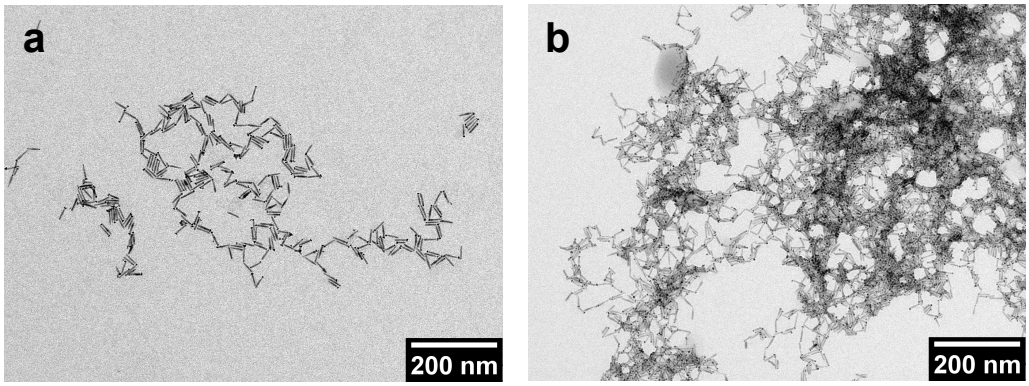

Figure 7.32: TEM micrographs of MUA-capped, Pt-CdSe/CdS DRs in water in the presence of IPA at neutral pH (a) and pH 11 (b). At increased pH, the NPs aggregate. DLS and absorbance measurements suggest that the aggregation is even stronger at pH 14, however the large amount of KOH inhibits imaging *via* TEM. Figure modified from Wengler-Rust *et al.*,[103] used under *Creative Commons CC-BY* license.

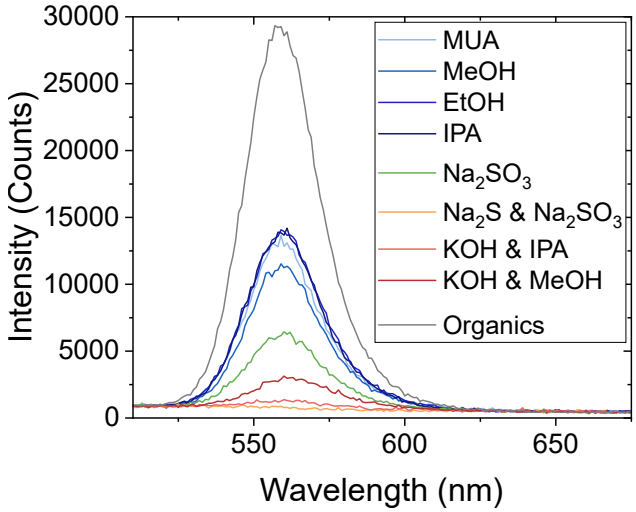

Figure 7.33: Static PL spectra of MUA-capped, Pt-tipped CdSe/CdS DRs in water (MUA), in the presence of different EDAs (MeOH, EtOH, IPA, Na_2SO_3, Na_2S & Na_2SO_3, KOH & IPA, KOH & MeOH), and in toluene, capped with non-polar, organic ligands (Organics). The PL peaks are located at 558-560 nm in the presence of alcohols, Na_2SO_3 and without EDA (MUA), whereas they shift bathochromicaly to 562 and 563 nm for KOH & IPA and KOH & MeOH, respectively, and no clear peak occurs for Na_2S & Na_2SO_3. Figure modified from Wengler-Rust *et al.*,[103] used under *Creative Commons CC-BY* license.

7.5.2 Steady-State Hydrogen Production Measurements

The photocatalytic activity of the NPs in the presence of various EDAs was investigated by steady-state hydrogen production measurements (**Figure 7.34**).[4]

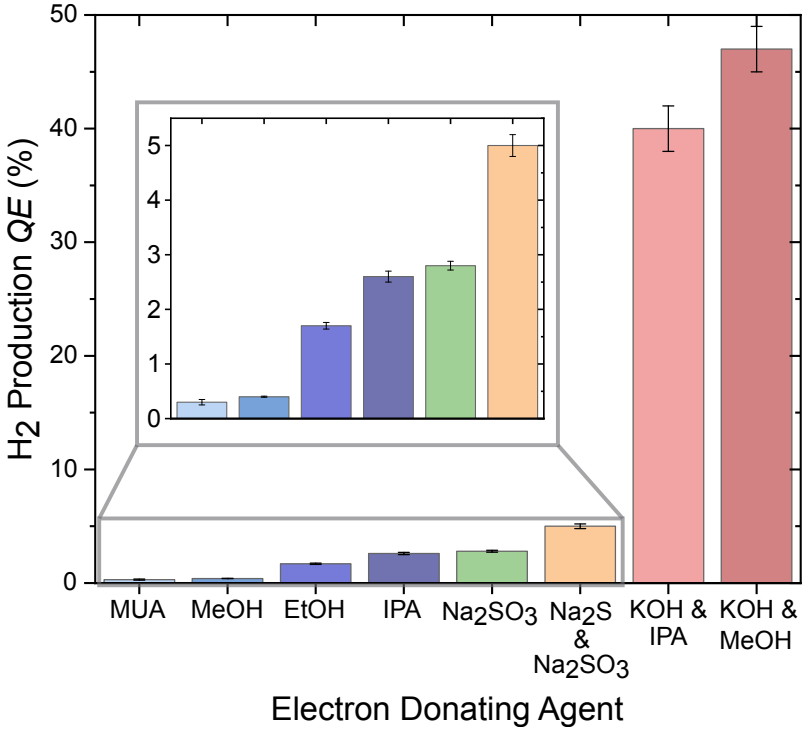

Figure 7.34: Quantum efficiencies in hydrogen production for MUA-capped, Pt-tipped CdSe/CdS DRs in water, without a sacrificial EDA added (MUA, QE_{H_2} = 0.3 ± 0.05 %) and in the presence of different sacrificial EDAs: MeOH (0.4 ± 0.01 %), EtOH (1.7 ± 0.06 %), IPA (2.6 ± 0.1 %), Na_2SO_3 (2.8 ± 0.08 %), Na_2S & Na_2SO_3 (5 ± 0.2 %), KOH & IPA (40 ± 2 %), and KOH & MeOH (47 ± 2 %). See Figure A8 for hydrogen production measurements. Figure modified from Wengler-Rust *et al.*,[103] used under *Creative Commons CC-BY* license.

The cuvette setup was used for this study as it enables the accumulation of hydrogen gas and thus the detection of the analyte even at small production rates. In accordance with literature, the determined QE_{H_2} is strongly affected by the introduced EDA.[32;34–36;38] The largest QE_{H_2} is obtained upon addition of the sulfide & sulfite mixture and the hydroxide & alcohol mixtures, even though the presence of hydroxide and sulfide induces NP agglomeration. These observations are consistent with previous reports stating that the agglomeration of nanophotocatalyst forming 3D networks does in fact increase the QE_{H_2}, despite reducing the overall accessible surface area.[107;181–187] These reports attribute the rise in

[4]For the measurement in the absence of a sacrificial EDA (MUA), an alternative batch of MUA-capped, Pt-tipped DRs was used (see Section A6.1 for details).

QE_{H_2} to the energetic coupling between the attaching NPs, which enables charge carriers' movement within the extended networks. Therefore, the formation of networks results in improved spatial charge separation over different NPs. Additionally, photogenerated electrons from different NPs can accumulate at one metal domain, creating a photocathode with increased potential for hydrogen production.[107;182;186] This "antenna mechanism" should be particularly beneficial if some of the NPs have no tips, as these bare DRs do not contribute to the photocatalytic activity if they are individually dispersed,[5] whereas they do in NP networks due to inter-particle charge transfer.[107;184] As discussed above, the Pt-tipped DRs synthesized *via* high-temperature synthesis always yield a mixture of bare DRs and Pt-tipped DRs of different tip size and number.
Conducting cryo-TEM measurements, it was found that the NPs attach tip-to-tip, forming chain-like structures or assembling into spherical "hedgehog"-agglomerates in suspension (**Figure 7.35**).[107;188] Given this preference for tip-to-tip alignment during single NP assembly, the NPs within the extended networks are likely to exhibit the same relative orientation. Therefore, within the network, nodes consisting of attached Pt tips should be present, facilitating the accumulation of electrons from multiple NPs in these metal centers.

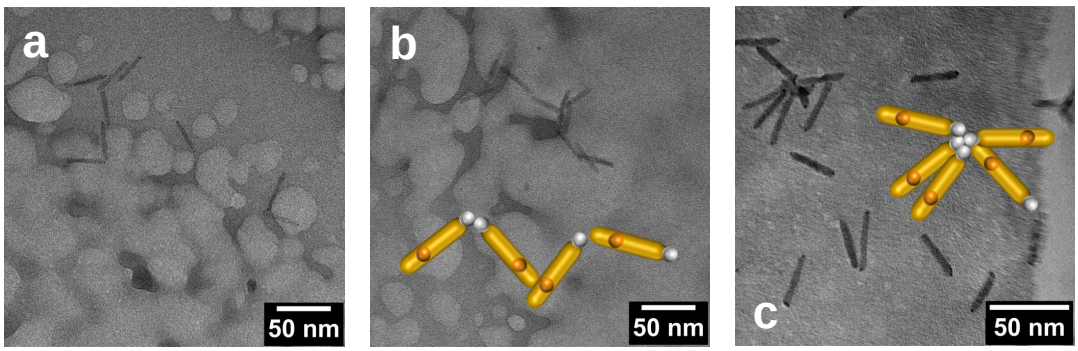

Figure 7.35: Cryo-TEM micrographs of MUA-capped and Pt-tipped CdSe/CdS DRs in water (a+b) and in the presence of hydroxide (c) after precipitation and redisperion at pH 6.9 and 9.8, respectively. Many DRs assembled tip-to-tip in the aqueous suspension. The sketches of attached Pt-DRs are a guide to the eye. Figure modified from Wengler-Rust *et al.*,[103] used under *Creative Commons CC-BY* license.

[5]No hydrogen evolution was observed in a 3 h steady-state hydrogen production measurement, using bare CdSe/CdS DRs in presence of the hydroxide & IPA mixture (1 M KOH & 10 vol% IPA) or only IPA (*cf.* Figure 7.26).

7.5.3 Time-Resolved Spectroscopy

The influence of the EDAs on the charge carrier dynamics within the DRs was investigated by TA spectroscopy (**Figure 7.36**). In accordance with the static ab-

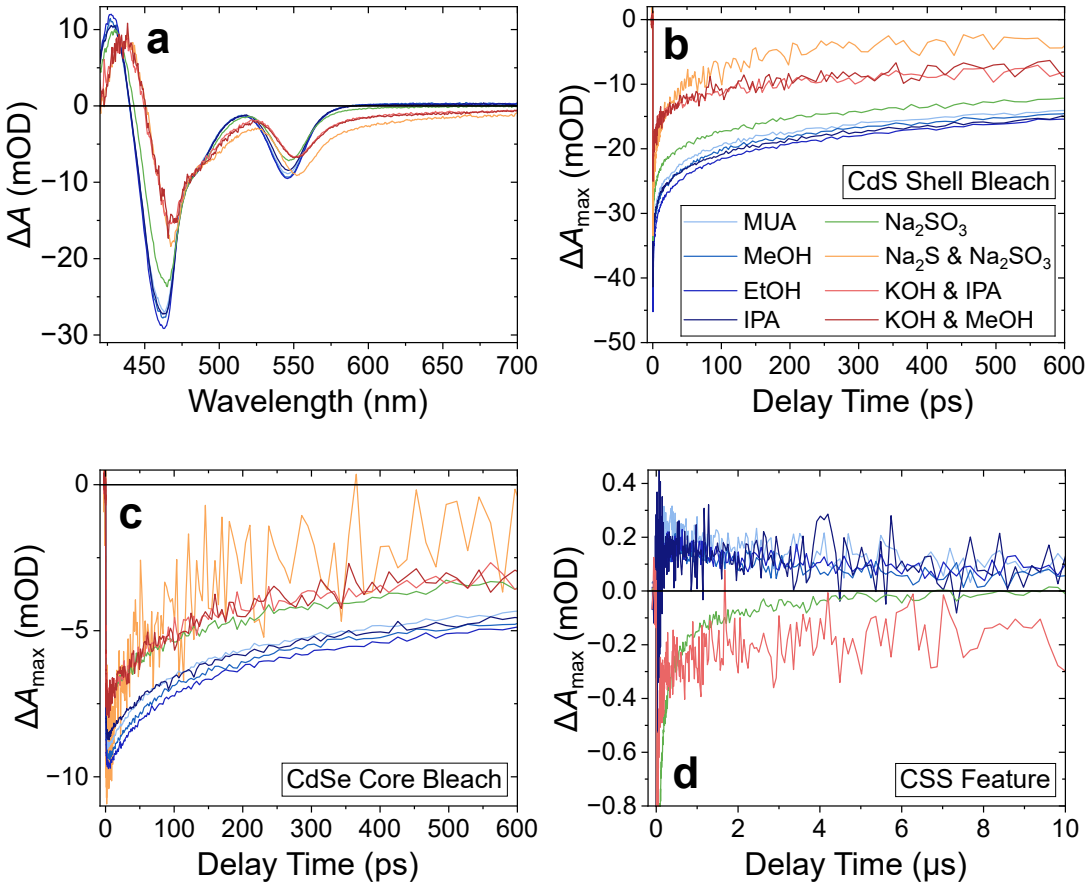

Figure 7.36: TA spectra at 10 ps delay time (a), bleach recovery kinetics of the CdS shell (b) and CdSe core (c) feature at bleach maximum, and averaged TA kinetics in a wavelength range from 475 nm to 490 nm (d), displaying the CSS feature (see text), of MUA-capped, Pt-tipped CdSe/CdS DRs in the presence of different EDAs (see color code in (b)), after excitation at 400 nm. The shell kinetics were plotted at wavelengths of: 462 nm for MUA, MeOH, EtOH, IPA, 464 nm for Na_2SO_3, 468 nm for Na_2S & Na_2SO_3, KOH & IPA, and KOH & MeOH; core kinetics: 548 nm for MUA, MeOH, EtOH, IPA, Na_2SO_3, 552 nm for Na_2S & Na_2SO_3, KOH & IPA, and KOH & MeOH. The TA kinetics after introduction of Na_2S & Na_2SO_3 and KOH & MeOH are omitted in (d) for clarity, as these measurements are very noisy in this spectral region. Figure modified from Wengler-Rust *et al.*,[103] used under *Creative Commons CC-BY* license.

sorbance and PL spectra (Figure 7.28a+b and Figure 7.33), the NPs' TA spectra shift bathochromicaly in the presence of sulfide and hydroxide (Figure 7.36a). In order to account for this shift, the bleach recovery kinetics of the CdS shell and

CdSe core feature are plotted for the wavelength at the bleach maximum for each EDA (indicated by the ΔA_{max} label on the y-axis in Figure 7.36b+c). The bare DRs exhibit the same TA bleach decay kinetics in the presence of alcoholic EDAs and hydroxide, indicating that the observed EDA-induced changes in the decay kinetics for the Pt-tipped DRs indeed result from charge transfer processes in the context of photocatalytic activity of the latter (*cf.* Figure A11). In Cd-chalcogenide NPs, the bleach feature is dominated by electrons occupying the CB ground state, while photogenerated holes contribute much weaker due to the high degeneracy of band edge hole states.[189–191] However, the bleach recovery kinetics of the Pt-DRs still allow for investigation of the hole transfer onto the EDA. As hole and electron experience Coulomb attraction, the latter are more mobile and can transfer into the Pt tip faster if the former are scavenged by the EDA, resulting in an accelerated bleach recovery (*cf.* **Figure 7.37**).[34]

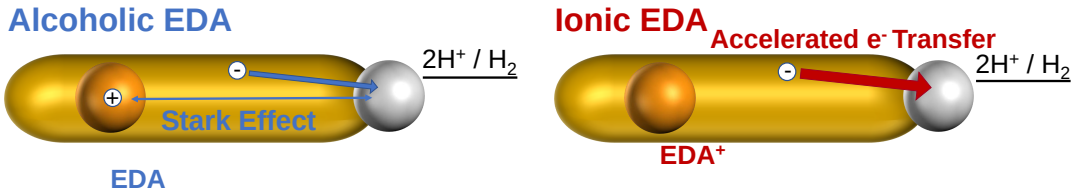

Figure 7.37: Scheme illustrating the emergence of the Stark effect in the presence of the alcoholic EDAs (left) and the accelerated electron transfer into the Pt tip due to direct hole transfer onto the surface-active ionic EDAs (right). The Stark effect is generated by the electric field between the electrons at the Pt tip and the holes at the CdSe core. Figure modified from Wengler-Rust *et al.*,[103] used under *Creative Commons CC-BY* license.

The TA shell and core bleaches recover similarly in the presence of the alcoholic EDAs (IPA, MeOH, EtOH) and without any added EDA (MUA) (Figure 7.36b+c). In contrast, after introducing the ionic EDAs (sulfite, the mixture of sulfide & sulfite, and the mixtures of hydroxide & alcohol), the TA bleach recovery kinetics are significantly accelerated compared to the alcoholic EDAs.
Additionally, the presence of surface-active and diffusion-limited EDAs influences the emergence of the CSS feature (Figure 7.36d).[6] In the presence of the alcoholic EDAs and if no EDA is added, a long-lived CSS feature occurs (positive ΔA). On the contrary, after adding the ionic EDAs, no CSS feature emerges, and only the recovery of the bulb bleach is observable in the spectral region.

[6] As the CSS feature did not emerge as a discernable feature for the batch of Pt-DRs used for the time-resolved and steady-state measurements shown in this section, a similar batch of Pt-DRs was studied (see above for detailed discussion on the NP parameter-dependent occurrence of the CSS feature and see Section A2 for sample parameters).

In line with the TA kinetics, the PL is largely quenched (Figure 7.33, **Table 7.8**, and **Table 7.9**), and the PL decay is significantly accelerated (**Figure 7.38**) in the presence of the surface-active compared to the diffusion-limited EDAs.

Table 7.8: PL quantum yields of MUA-capped, Pt-tipped CdSe/CdS DRs in water (MUA) and in the presence of different diffusion-limited EDAs (MeOH, EtOH, IPA). The quantum yields were determined in a spectrofluorometer.

Electron Donor	MUA	MeOH	EtOH	IPA
QY_{PL} (%)	3	3	3	4

Table 7.9: PL quantum yields of MUA-capped, Pt-tipped CdSe/CdS DRs in water in the presence of surface-active EDAs (Na_2SO_3, Na_2S & Na_2SO_3, KOH & IPA, KOH & MeOH). The quantum yields were determined in a spectrofluorometer.

Electron Donor	Na_2SO_3	Na_2S & Na_2SO_3	KOH & IPA	KOH & MeOH
QY_{PL} (%)	1	0	0	0

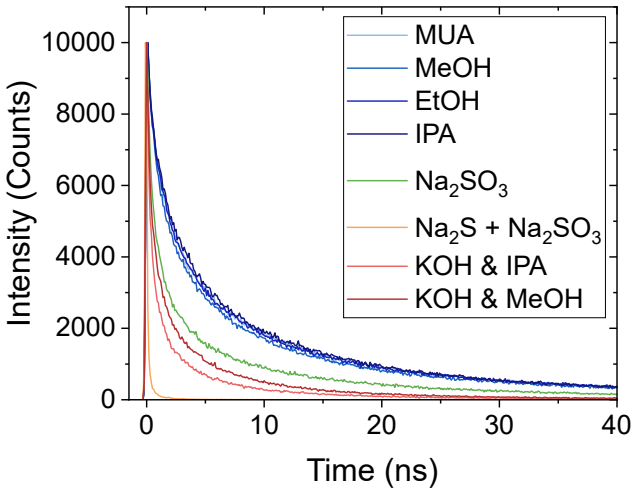

Figure 7.38: PL decay kinetics of MUA-capped, Pt-tipped CdSe/CdS DRs in water (MUA), in the presence of different EDAs (MeOH, EtOH, IPA, Na_2SO_3, Na_2S & Na_2SO_3, KOH & IPA, KOH & MeOH). The measurements were conducted at 445 nm excitation and the spectra were recorded at the wavelength of the PL maximum (see Figure 7.33 for PL peaks and position). Figure modified from Wengler-Rust *et al.*,[103] used under *Creative Commons CC-BY* license.

7.5.4 Alcoholic Electron Donating Agents

If no sacrificial EDA is present, the photoinduced holes are exclusively scavenged by the thiolate group of the MUA ligand.[7] [38;65;162;192] Interestingly, the charge carrier dynamics are not affected by the presence of the alcoholic EDAs, indicated by the unaltered TA bleach recovery kinetics (Figure 7.36b+c and see Figure A14 for long delay times) and PL decays (Figure 7.38). This finding suggests that the photogenerated holes do not transfer directly onto these EDAs but only onto the MUA ligand. Subsequently, the oxidized ligand can potentially be reduced by the alcoholic EDA (*cf.* **Figure 7.39**a). At the start of the measurement, the NPs' surface is most likely hardly accessible for the alcoholic EDAs as the MUA ligands shield it. The alkyl chains of the surface-attached MUA ligands were found to form a non-polar layer, which repels the aqueous solvent, and therefore should likewise repel the alcoholic EDAs.[34;193–195] However, continued illumination gradually degrades the ligand shell, as oxidized MUA ligands detach from the NPs' surface after forming dithiols.[34;162;166] The resulting holes in the ligand shell enable the alcoholic EDAs to access the NPs' surface and scavenge holes from the oxidized head groups of the MUA ligands in a diffusion-limited manner (*cf.* Figure 7.39a). The variations in QE_{H_2} in the presence of the different alcoholic EDAs probably result from the differences in the EDAs' redox potentials, as these determine the scavenging rate of trapped holes from the MUA ligands (-0.055 V for MeOH forming formaledhyde, -0.19 V for EtOH forming acetaldehyde, -0.28 V for IPA forming acetone).[115;196] In fact, the hole transfer may not occur *via* a two- but one-electron transfer process, creating a free radical intermediate. This radical is least reductive for MeOH, the EtOH radical is second, and the IPA radical is most reductive (-0.74 V, -0.94 V, -1.2 V vs NHE at pH 7, correlating with the pK_a value of the radicals: 10.7, 11.6, 12.2 for MeOH, EtOH, and IPA, respectively).[106;116;117;197] Therefore, the current doubling effect is least likely to occur for the MeOH and most likely for the IPA radical. This circumstance will probably contribute to the differences in QE_{H_2} in the presence of the alcoholic EDAs, as the occurrence of the current doubling effect increases the determined QE_{H_2}.
Since the hole transfer from the ligand onto the alcoholic EDA occurs outside the semiconductor domain, it is not resolved in the shell or core TA kinetics. Nevertheless, the STH feature provides indications for the occurrence of the transfer.

[7] Besides ligand oxidation, photogenerated holes can oxidize the anions in the semiconductor crystal lattice, resulting in a degradation of the semiconductor domain.[106;166] This degradation is clearly visible at the semiconductor domain of the Pt-DRs after three hours of illumination, in the absence of a sacrificial EDA (see Figure A13b). The introduction of a sacrificial EDA prevents the degradation of the semiconductor (see Figure A13c+d).

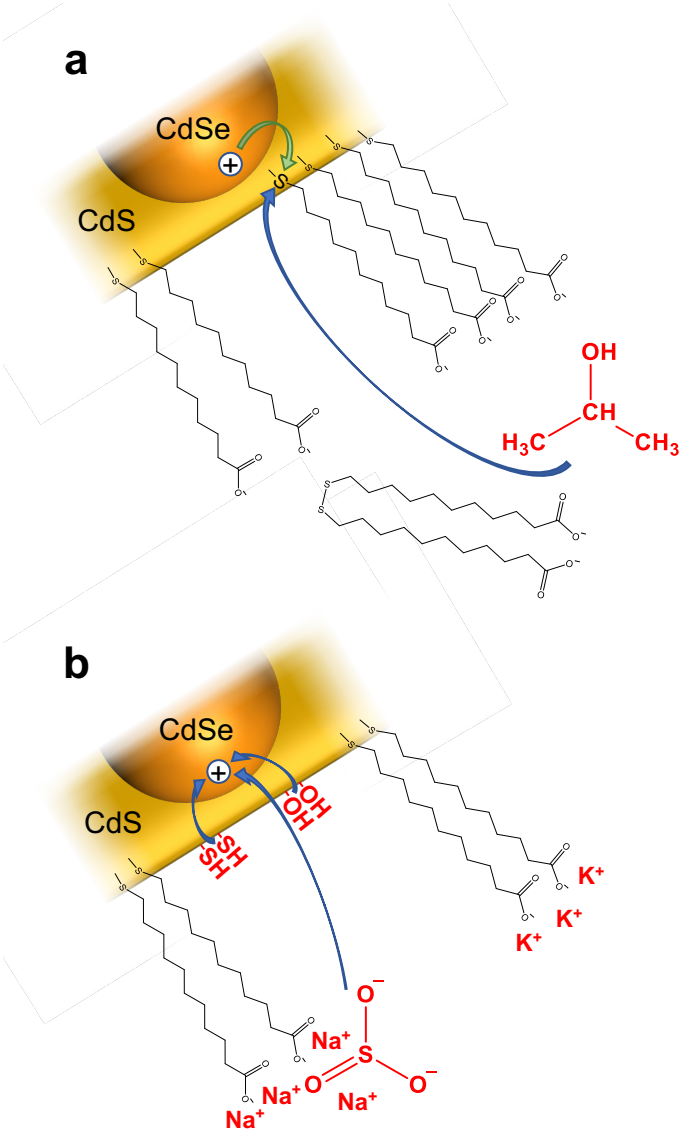

Figure 7.39: Scheme illustrating the hole transfer onto diffusion-limited (a) and surface-active (b) EDAs. The diffusion-limited, alcoholic EDAs (IPA in this example) have to penetrate through gaps in the ligand shell in order to scavenge the photogenerated holes from the oxidized thiolate groups of the MUA ligands. On the contrary, the surface-active EDAs (hydroxide, sulfide, and sulfite in this example) attach to the NP's surface or locate in the solvation shell of the NP, resulting in a much faster hole transfer compared to the diffusion-limited EDAs. The blue arrows indicate movement of the EDA and electron transfer, while the green arrow indicates hole transfer. Figure modified from Wengler-Rust *et al.*,[103] used under *Creative Commons CC-BY* license.

The STH feature seems to recover faster in the presence of the most active alcoholic EDA IPA within the first nanoseconds, suggesting consumption of the trapped charges (**Figure 7.40**). On longer time scales, both kinetics decay simi-

larly, indicating that the hole transfer onto the EDA occurs within nanoseconds. The long-lived feature probably results from holes trapped in deep trap states of large potential, exceeding the redox potential of the alcoholic EDA. However, due to the large noise level of the measurement, the trends are not clearly discernible.

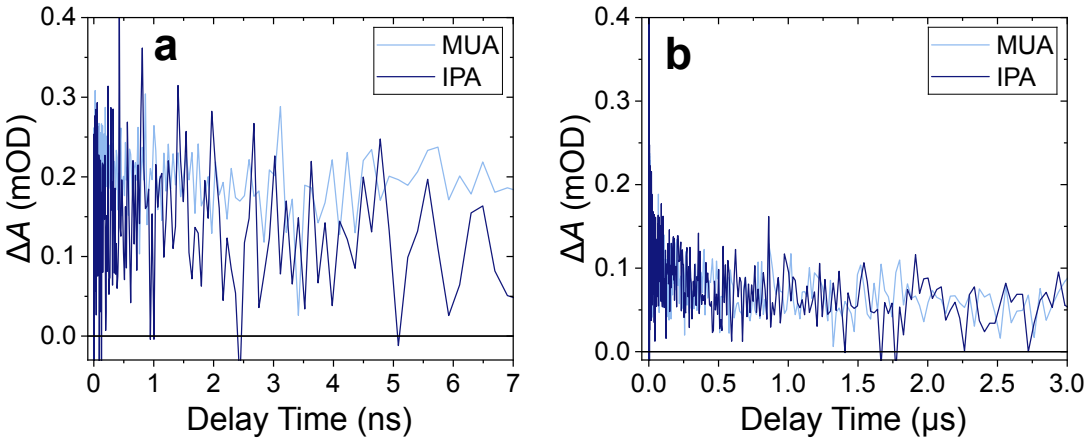

Figure 7.40: TA decay kinetics of the STH feature, averaged in the probe spectral range from 600 to 700 nm at different delay time ranges (a+b). The measurements were conducted at 400 nm excitation, using MUA-capped, Pt-tipped CdSe/CdS DRs in water (MUA) and in the presence of IPA, combining fs- and ns-TA measurements. The decay kinetics in the presence of the alcoholic EDAs MeOH and EtOH are shown in Figure A15.

7.5.5 Ionic Electron Donating Agents

The accelerated TA bleach recovery (Figure 7.36b+c) and PL decay (Figure 7.38) kinetics after introducing the ionic EDAs indicate a direct transfer of the photoinduced holes onto these EDAs. The surface activity of the ionic EDAs favors direct hole transfer. While hydroxide and sulfide attach to the NPs' surface (see above), the sulfite anions are likely to accumulate in the NPs' solvation shell (*cf.* Figure 7.39b; see below for a more detailed discussion on EDA-specific surface interactions). Additionally, the occurrence of the CSS feature confirms the differences in the hole transfer rates between the alcoholic and ionic EDAs (Figure 7.36d). In the absence of an EDA and in the presence of the alcoholic EDAs, the CSS feature emerges, indicating a long-lived charge-separated state, generated by the electrons at the Pt tip and holes in the semiconductor domain (*cf.* Figure 7.37a). In contrast, after introducing the ionic EDAs, no CSS feature occurs, which suggests accelerated hole transfer, proceeding faster than the bulb bleach recovery (*cf.* Figure 7.37b). Moreover, the PL intensity is strongly quenched in the presence of the ionic EDAs (Figure 7.33, Table 7.8, and Table 7.9), verifying the

emergence of additional non-radiative decay channels, such as direct hole transfer onto the surface-active EDAs.

Sodium Sulfite

The ions of the dissociated sodium sulfite salt are likely to localize in the NPs' solvation shell (*cf.* Figure 7.39b). In contrast to the hydroxide and sulfide anions, the sulfite anion interacts only weakly with the CdS surface of the NPs and does not bind to it.[88;198] That sulfite anions interact less strongly with the CdS surface than sulfide anions can also be deduced from the shift of the CdS flatband potential, which is significantly larger for sulfide than sulfite anions.[198] Nevertheless, if the ligand shell is partly degraded due to oxidation of the ligand, the polar sulfite anion can be expected to be located closely to the NPs' surface, favoring fast and direct hole transfer. This direct hole transfer is enabled for the sulfite anion, as its redox potential for the one-electron transfer is lower than the redox potential of the thiolate ligand (~ 0.7 V vs NHE and 0.8 V vs NHE, respectively; for comparison: the one-electron redox potential for MeOH is ~ 1.2 V).[36;38;110;112–115;162;163] Additionally, the elevated concentration of hydroxide anions after introducing the basic sodium sulfite and sulfide may favor direct hole transfer (pH = 10 for 0.1 M Na_2SO_3 and pH = 13 for 0.1 M Na_2S & Na_2SO_3).[27]

Moreover, the presence of the sulfite alters the assembly behavior of the Pt-DRs (*cf.* Figure A12c). After introducing the sulfite, the NPs do not attach tip-to-tip or agglomerate but are mostly singly dispersed and assemble in a lateral side-by-side orientation. The resulting attenuation of the antenna mechanism in the presence of sulfite might cause the unexpectedly small QE_{H_2}, which is only slightly larger than in the presence of IPA, despite direct hole transfer (Figure 7.34). The observed change in assembly behavior may be caused by the growth of the NPs' solvation shell due to the accumulation of the salt's ions (*cf.* Figure 7.28c). Furthermore, the sulfite anion might bind to the CdS crystal lattice after oxidation, forming a thiosulfate at the NPs' surface, making it gradually less accessible.

Sodium Sulfide & Sodium Sulfite

In the presence of the EDA mixture of sulfide & sulfite, the TA shell and core bleaches recover most rapidly (Figure 7.36b+c). However, the QE_{H_2} in the presence of the sulfide & sulfite mixture is significantly smaller than for the hydroxide & alcohol mixtures (Figure 7.34). Lian and coworkers stated that the attachment of the sulfide anions to the NPs' surface creates an additional channel for charge recombination *via* the Auger mechanism.[174] This additional channel would accelerate the decay kinetics but compete with hydrogen production. They argue

that the Auger mechanism is enabled by "spectator" electrons at the NPs' surface, created by the reduction of redox-active mid-gap states of the semiconductor by the sulfide anions.[174;199] However, since the sulfide anions predominantly form HS^- by hydrolysis in aqueous solution,[174;175] they are likely to bind to the NPs' surface similarly to the MUA ligand (RS^-). Hence, the NPs' surface is not necessarily charged by the attachment of the HS^- anions, but the colloidal stability is significantly reduced due to the missing alkyl chain and carboxylic head group of the ligand (*cf.* Figure 7.39b). Therefore, the acceleration of the PL and TA kinetics may instead result from fast hole trapping and scavenging by the surface-attached sulfide anions. Various additional factors may reduce the photocatalytic activity of the Pt-DRs in the presence of the EDA mixture of sulfide & sulfite. For instance, the oxidation of sulfide anions can produce oxidative disulfide anions, which were found to compete with the proton reduction at the photocathode.[175;198] However, for the mixture of sulfide & sulfite, the formation of disulfide anions is mitigated, and existing disulfides are scavenged by the sulfite anions, which form thiosulfates instead.[36;175;198] Additionally, the sulfide anions may poison the Pt photocathode by binding to its surface and impeding proton reduction.[200–204]

Potassium Hydroxide & Alcohol

In the presence of hydroxide & alcohol, the largest QE_{H_2} is obtained (Figure 7.34). While at neutral pH, the addition of MeOH achieves the smallest QE_{H_2} of all alcoholic EDAs (6.5-times smaller QE_{H_2} than IPA), the QE_{H_2} at pH 14 is larger in the presence of MeOH than IPA. This increase in QE_{H_2} may result from an enhanced concentration of alkoxides. As MeOH has a smaller pK_a value than IPA (MeOH: $pK_a = 15.3$, IPA: $pK_a = 17.1$),[205] at pH 14, the concentration of methoxide is roughly two orders of magnitude larger than the concentration of the alkoxide forming from the dissociation of IPA ($10^{-1}\,\frac{mol}{L}$ for MeOH and $10^{-3}\,\frac{mol}{L}$ for IPA, see Section A6.3 for calculation). These alkoxides are highly reductive species and may therefore function as additional EDAs.

Furthermore, the rise in QE_{H_2} with increasing pH was attributed to the high mobility of the hydroxide anion and radical.[32;34] The hydroxide radical, forming upon oxidation of the anion, functions as a redox shuttle by quickly relaying the photoinduced hole to the alcoholic EDA.[34] However, this process may also occur for a *SH or *SR radical, created upon oxidation of the sulfide anion or the thiolate group of the MUA ligand, respectively. But, as the reduction potential of hydroxide radical is significantly larger than the one of the sulfanyl and thiyl

radicals (1.9 V for hydroxide and 1.2 V for sulfanyl radical),[8] [113;114] the likelihood and resulting rate of hole transfer from the hydroxide onto the alcoholic EDA is much larger than for the oxidized MUA ligand. Furthermore, the large reduction potential of the hydroxide radical enables it to reduce nearly any agent in its vicinity in a diffusion-limited process. Thus, besides shuttling holes to the alcoholic EDA, it may also oxidize remaining MUA ligand at the surface of the NP. Consequently, this process may also contribute to the gradual degradation of the NPs' ligand shell at high pH.

As the pH affects the reduction potentials of the alcohols, it may likewise affect the occurrence of the current doubling effect.[116;117;197] The pH dependency of the reduction potentials of the EDAs follows a Nernstian behavior (-59 mV/pH), whereas the CdS CB and VB potentials increase by only -33 mV/pH.[34] Therefore, the driving force for the occurrence of the current doubling effect increases with pH. Analogously, the current doubling effect may occur for the formed alkoxides, as well as the sulfide and sulfite radicals ($^{*}S^{-}$, $^{*}SO_3^{-}$), as these are highly reductive species.[36] Thus, the current doubling effect is likely to contribute to the large QE_{H_2} in the presence of the alcohol & hydroxide mixtures and the sulfide & sulfite mixture (*cf.* Figure 7.34).

7.6 Illumination Time- and Power Density-Dependent Measurements

7.6.1 Illumination Time-Dependent Photocatalytic Activity

The time-dependent study was performed by combining steady-state hydrogen production measurements in an online reactor and cuvette setup with time-resolved and static PL spectroscopy, as well as TA spectroscopy. The online reactor setup was designed and assembled by Sebastian Hentschel (*Mews Research Group, Institut für Physikalische Chemie, Universität Hamburg*) and the hydrogen production and PL spectroscopy measurements inside the reactor were performed in collaboration with him. It was found that the hydrogen production rate is not constant during illumination but increases during the first few hours of illumination, while using IPA as an EDA. In the online reactor, the measured hydrogen concentration and the determined $QE_{H_2,online}$ increase continuously during a measurement time of four hours (**Figure 7.41**a). However, in this measurement, the increase in hydrogen production rate is superimposed with the effect of la-

[8] Note that potentials might deviate for surface-bound species.

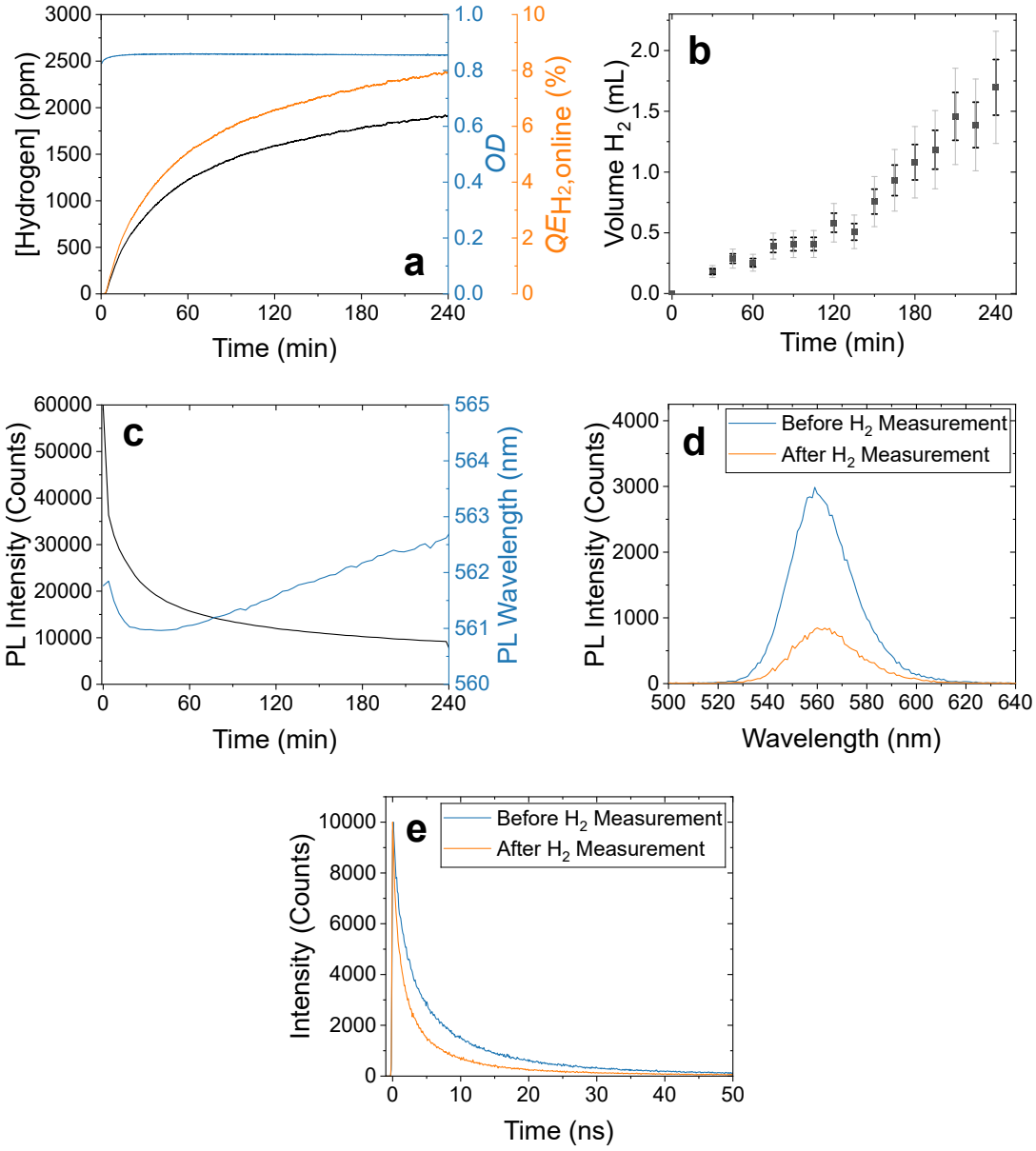

Figure 7.41: Time-dependent steady-state hydrogen production measurements conducted using the online reactor (a) and cuvette setup (b). Time-dependent PL during the measurement in the online reactor (c). Static PL spectra (d) and PL decay (e) before and after a hydrogen production measurement, at 445 nm excitation. For all displayed measurements, similar batches of MUA-capped, Pt-CdSe/CdS DRs in water were used and IPA was introduced as an EDA. The measurements in the reactor and cuvette setup were conducted at power densities of 12.2 mW cm^{-2} and 7.72 mW cm^{-2}, respectively.

tency between hydrogen evolution and detection of a constant hydrogen concentration in the reactor setup (see Section A7 for measurement and discussion on latency in the reactor setup). But, as this latency period lasts only 40 min (*cf.*

Figure A16), the increase in the hydrogen concentration and $QE_{H_2,online}$ for times >40 min can be attributed exclusively to a rise in the hydrogen production rate of the nanocatalysts. In the cuvette setup, the volume of accumulated hydrogen increases exponentially for long illumination times, which likewise indicates an increase in the hydrogen production rate (see Figure 7.41b). At the same time, the NPs' PL intensity decreases significantly, and the emission wavelength shifts during illumination (Figure 7.41c+d: maximum of PL peak shifts bathochromicaly by 2 nm after the steady-state hydrogen production measurement). Additionally, the PL decay is accelerated after the steady-state hydrogen production measurement (Figure 7.41e; τ_{ave} decreased from 8.1 to 6.4 ns; see Table A8 for fitting parameters).

Interestingly, similar trends are observable in TA spectroscopy (**Figure 7.42** and **Figure 7.43**). By recording multiple consecutive TA scans (220 s per scan and five maps were averaged, respectively), the illumination time-dependent change of the bleach features and the charge carrier dynamics were monitored. The CSS fea-

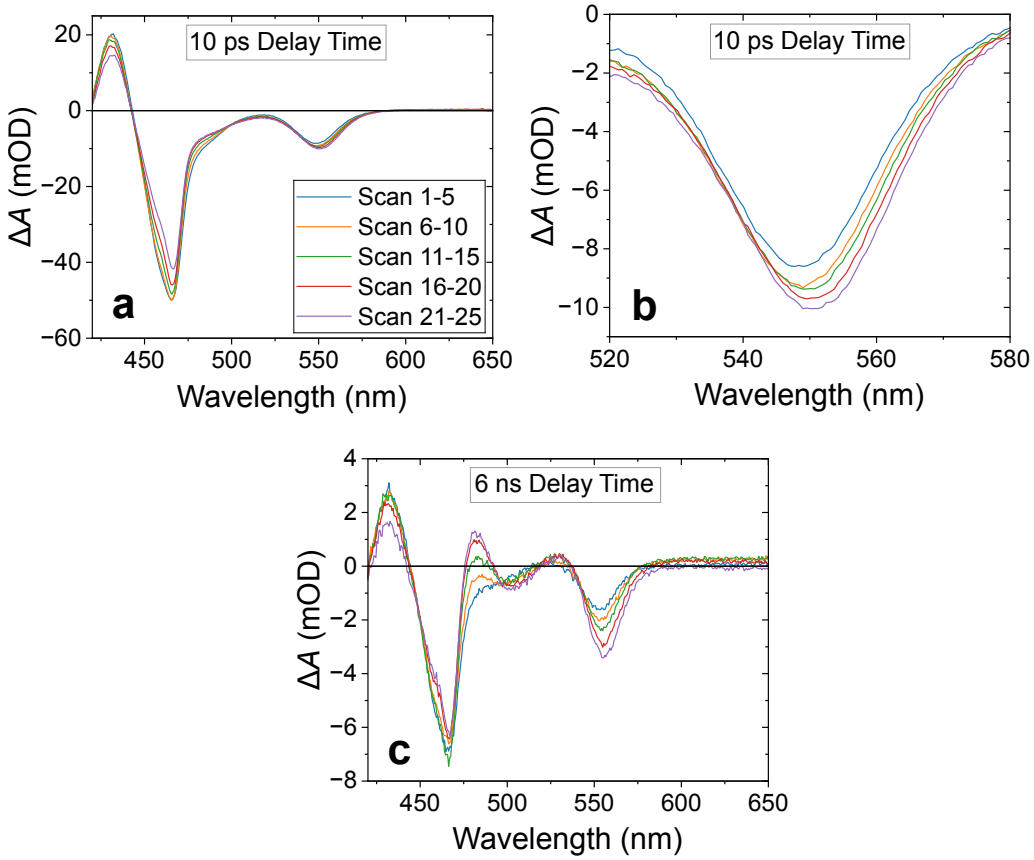

Figure 7.42: TA spectra of MUA-capped, Pt-CdSe/CdS DRs in the presence of IPA at 10 ps (a+b) and 6 ns (c) delay time, recorded in multiple consecutive scans, at 400 nm excitation. Five TA maps were averaged, respectively (see color code in (a)).

ture increases (Figure 7.42c), the CdSe core bleach rises and shifts bathochromicaly (Figure 7.42b+c and Figure 7.43b), the CdS shell bleach recovers faster (Figure 7.43e) and the core bleach gradually faster (Figure 7.43f) in later scans. These findings suggest that the charge separation becomes more efficient with increasing illumination time. The accelerated CdS bleach recovery indicates that the

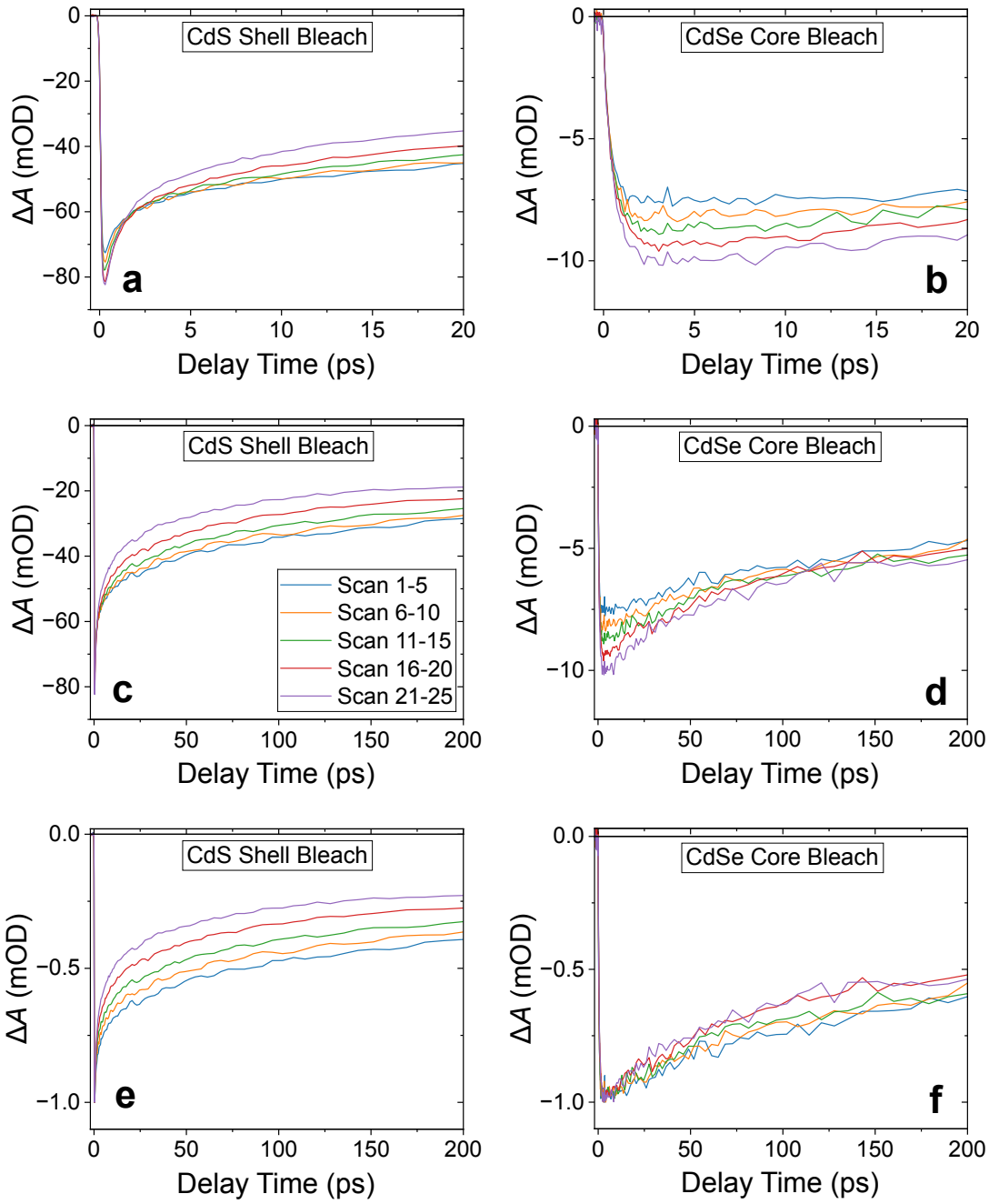

Figure 7.43: TA bleach recovery kinetics of the CdS shell (a+c+e) and the CdSe core (b+d+f) feature, non-normalized (a-d) and normalized (e+f) of MUA-capped, Pt-tipped CdSe/CdS DRs in the presence of IPA, recorded in multiple consecutive scans, at 400 nm excitation. Five TA maps were averaged, respectively (see color code in (c)).

electrons transfer into the Pt tip more quickly with increasing illumination time. The increased CSS feature shows that a growing number of spatially separated charge carriers are available for photocatalysis, which is consistent with the observed rise in the hydrogen production rate. The improved charge separation might result from the successive ligand loss by photooxidation, enabling the diffusion-limited EDA to access the surface (Figure 7.39a). At the same time, the ligand loss induces gradual agglomeration of the NPs, enabling inter-particle charge transfer (see above). As a consequence, the PL intensity is reduced, and the PL decay is accelerated. Additionally, the gradual agglomeration could account for the bathochromic shift observed in TA and PL spectroscopy. The successive rise of the core bleach indicates that more charge carriers transfer into the core over time. Additionally, annealing processes may occur at the interface of the CdSe and CdS domains. The same illumination time-dependent behavior can be observed in TA if no sacrificial EDA is added (**Figure 7.44**).

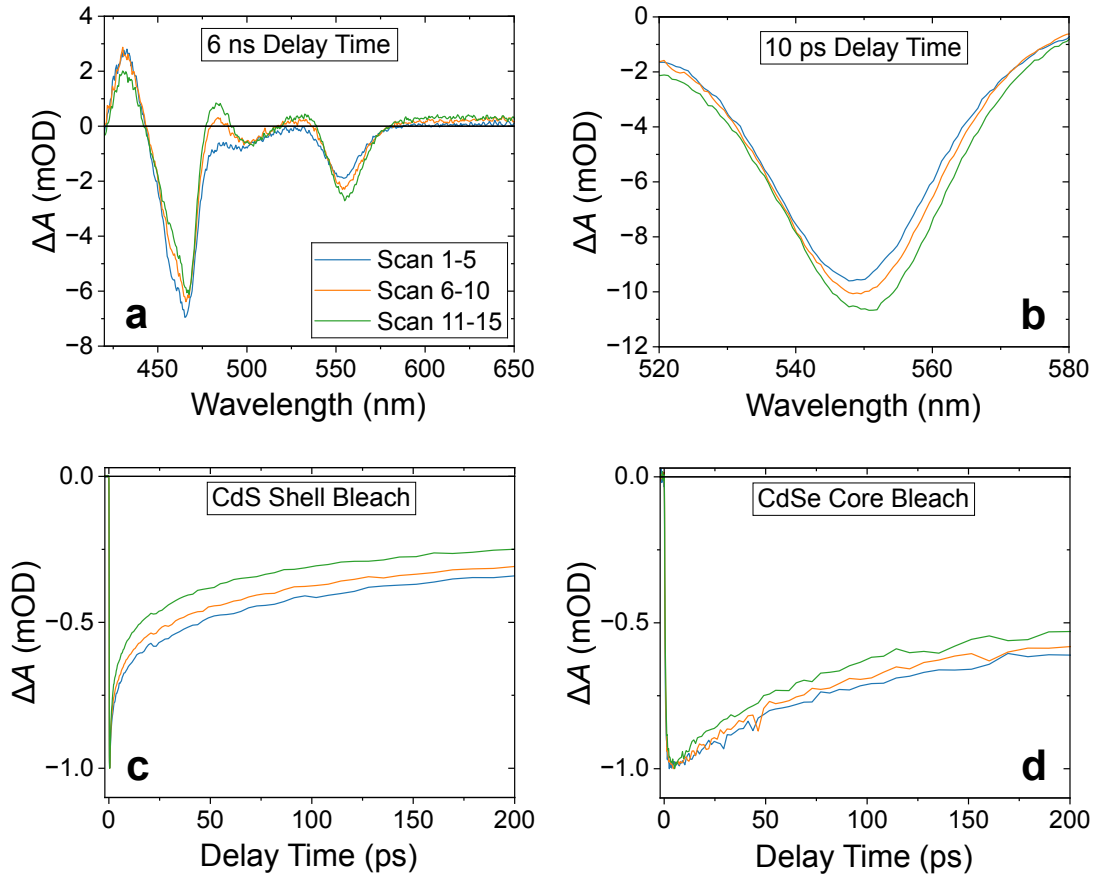

Figure 7.44: TA spectra at 6 ns (a) and 10 ps (b) delay time and normalized bleach recovery kinetics of the CdS shell (c) and CdSe core (d) feature of MUA-capped, Pt-CdSe/CdS DRs in water with no sacrificial EDA added, recorded in multiple consecutive scans, at 400 nm excitation. Five TA maps were averaged, respectively (see color code in (a)).

However, in the presence of sulfite, the NPs' illumination time-dependent TA spectra and kinetics are significantly altered (**Figure 7.45**). Independent of the illumination time, no CSS feature occurs in the presence of sulfite (Figure 7.45a), which is consistent with the findings presented in the EDA-dependent study (see Figure 7.36d). Furthermore, the initial core bleach increases slightly but does not shift bathochromicaly over time (Figure 7.45b), and the shell bleach recovery is not accelerated (Figure 7.45c). Possibly, the fast and direct hole transfer onto the sulfite diminishes MUA oxidation and therefore prevents NP agglomeration. The NP agglomeration might additionally be inhibited by the attachment of formed thiosulfate at the NPs' surface (see above). Due to the missing agglomeration, no bathochromic shift of the core bleach occurs, and the inter-particle charge transfer is impeded, resulting in a constant hydrogen production and bleach recovery rate. In line with this explanation, the steady-state hydrogen generation measurement conducted in the cuvette setup shows a linear behavior (see Figure A8e).

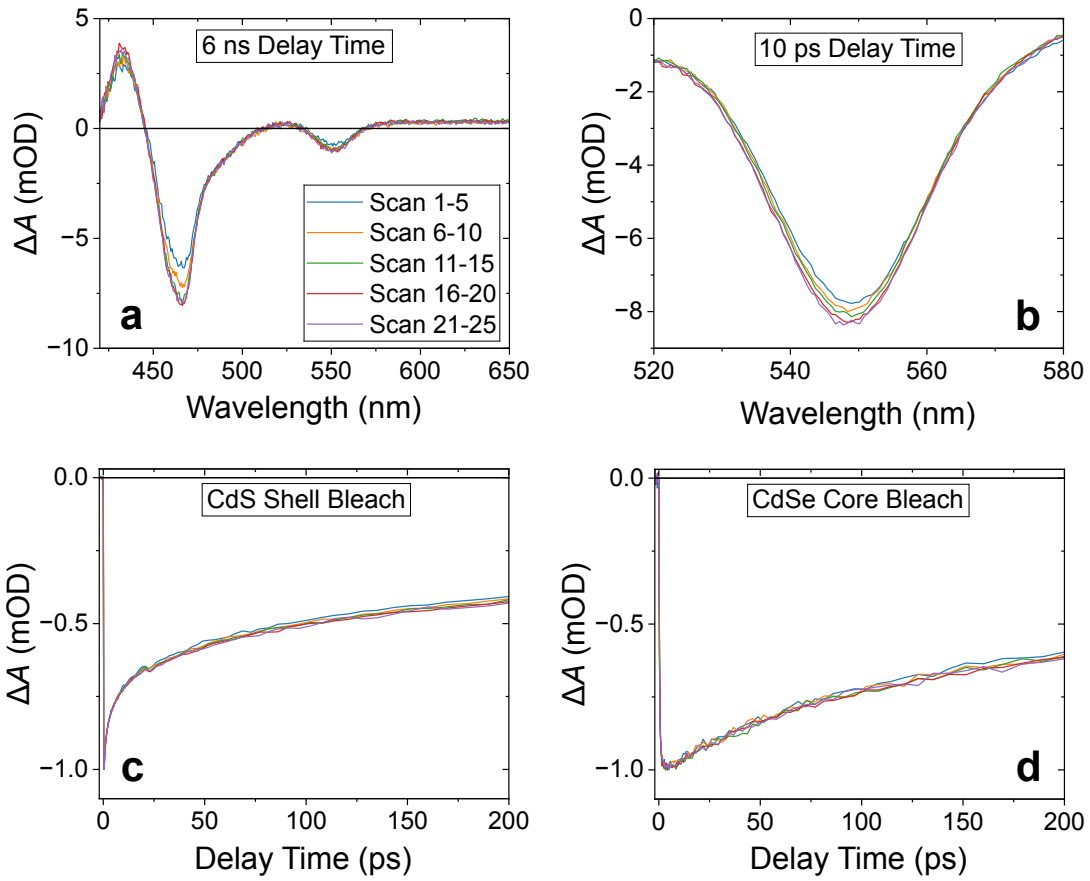

Figure 7.45: TA spectra at 6 ns (a) and 10 ps (b) delay time and normalized bleach recovery kinetics of the CdS shell (c) and CdSe core (d) feature of MUA-capped, Pt-tipped CdSe/CdS DRs in the presence of Na_2SO_3, recorded in multiple consecutive scans, at 400 nm excitation. Five maps were averaged, respectively (see color code in (a)).

7.6.2 Power Density-Dependent Photocatalytic Activity

Excitation power density-dependent measurements were partly conducted in the online reactor setup and partly in the cuvette setup. Due to the constant flow of carrier gas through the reactor setup, it allows for conveniently measuring large volumes of analyte. However, the constant gas flow impedes analyte detection at small production rates. In contrast, in the cuvette setup the produced gas can accumulate, enabling the detection of small volumes of analyte. Therefore, the online reactor and cuvette setup were used for experiments at large and small power densities, respectively.

In accordance with the illumination time-dependent studies, the determined hydrogen production rate and quantum efficiency in hydrogen production are dependent on the order in which the power density-dependent measurements are performed (**Figure 7.46** and **Figure 7.47**a+b).[9] When going from high to low densities, the hydrogen production rate decreases slower than it increases while go-

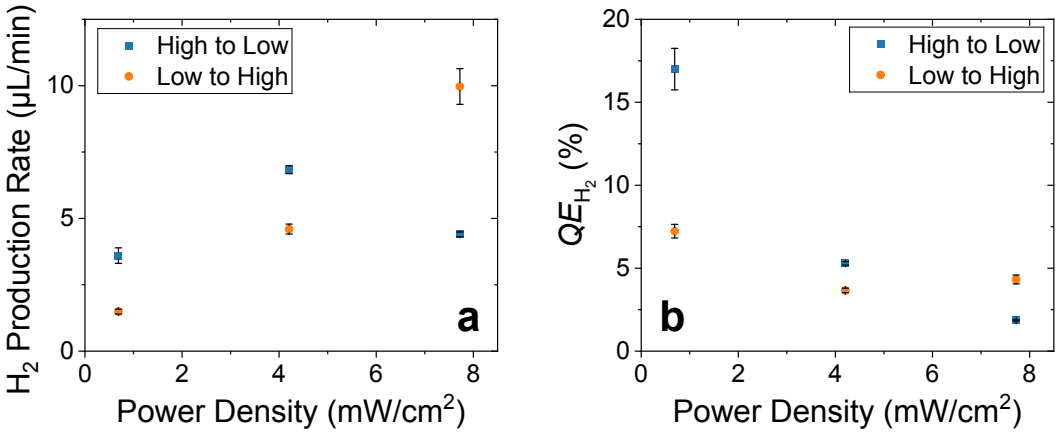

Figure 7.46: Power density-dependent hydrogen production rates (a) and quantum efficiencies in hydrogen production (b) determined by conducting steady-state hydrogen production measurements on MUA-capped, Pt-tipped CdSe/CdS DRs in the presence of IPA in the cuvette setup. The measurements were performed successively, changing the power density from high to low (blue squares) and low to high (orange circles), respectively. See Figure A18a-f for hydrogen production measurements.

[9] In Figure 7.46 two series of measurements were conducted in the cuvette setup, each consisting of three measurements of varying excitation power densities: the first series of measurements had decreasing power densities (high to low: 7.72 mW cm^{-2}, 4.21 mW cm^{-2}, 0.690 mW cm^{-2}), while the second had increasing power densities (low to high: 0.690 mW cm^{-2}, 4.21 mW cm^{-2}, 7.72 mW cm^{-2}). After each measurement, the cuvette was purged with nitrogen for 20 min. The measurements in the online reactor were conducted in two series of measurements, going from high to low (Figure 7.47a) and low to high (Figure 7.47b) power densities.

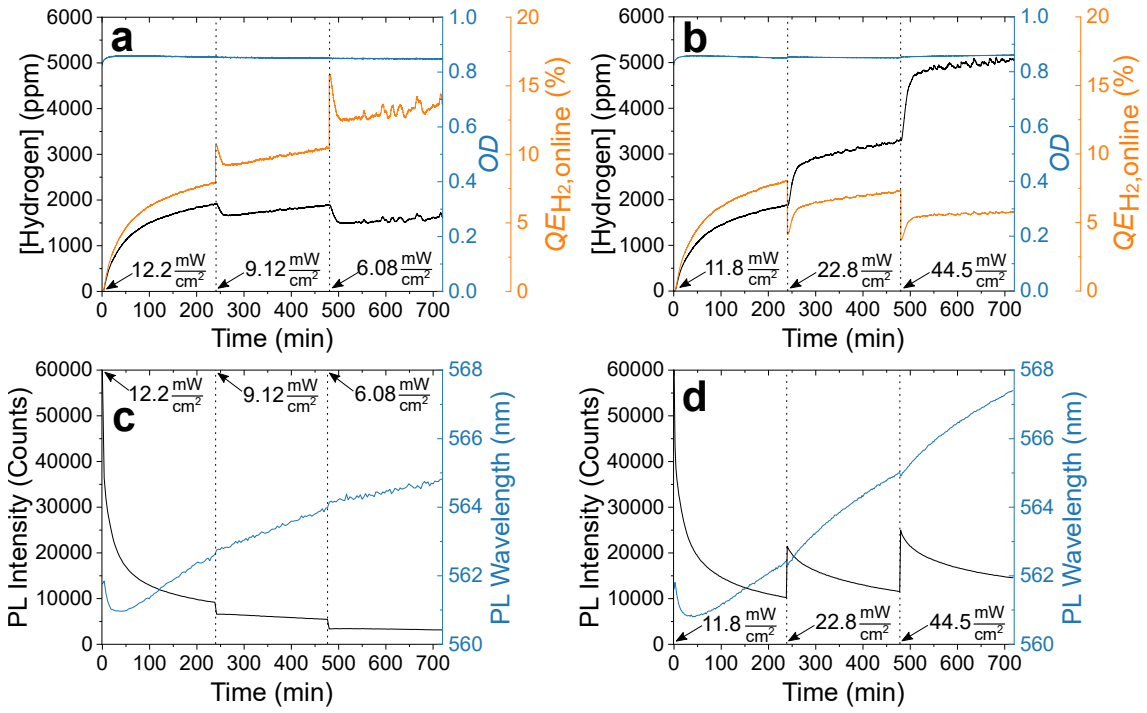

Figure 7.47: Steady-state hydrogen production measurements (a+b) and time-dependent PL measurements (c+d) of MUA-capped, Pt-tipped CdSe/CdS DRs in water in the presence of IPA, conducted in the online reactor at different power densities.

ing from low to high (Figure 7.46a and Figure 7.47a+b). Accordingly, the quantum efficiency increases faster going from high to low than it decreases while going from low to high power densities (Figure 7.46b and Figure 7.47a+b). Therefore, it can be deduced that the higher the power density, the faster the photocatalytic activity increases. This is especially evident in the second measurement at 4.21 mW cm^{-2} in Figure 7.46: both, the production rate and QE_{H_2} are higher when going from high to low than from low to high power densities. Additionally, the bathochromic shift is enhanced at larger power densities (Figure 7.47c+d). These findings support the explanation of ligand loss-induced agglomeration, which proceeds faster at larger power densities.

Combining the measurements from both setups, the power-dependent hydrogen production rate and QE_{H_2} were determined in a range from 0.241 mW cm^{-2} to 44.5 mW cm^{-2} (**Figure 7.48**; see Section A9 for details on calculation of production rates and QE_{H_2}, calibration, and error bars). The QE_{H_2} was found to increase exponentially with decreasing power density, which is in line with previous reports for large power densities (10 - 200 mW cm^{-2}).[34] The rise in QE_{H_2} probably results from a reduced charge recombination rate with decreasing power density

(*cf.* **Figure 7.49**).[34] Interestingly, the exponential trend of the QE_{H_2} continues for small power densities despite the increased time intervals between excitations of the individual NPs. As two electrons are required to form a hydrogen molecule, a photogenerated electron must live on the Pt tip of a single NP for hundreds of milliseconds before a hydrogen molecule can form (average of four absorbed photons per second per NP at 0.241 mW cm^{-2} power density; see Section A10 for calculation). However, the lifetime of the charge carriers is estimated to be only microseconds.[94;149] Therefore, the observed hydrogen generation at these small power densities indicates inter-particle charge transfer enabled by network formation.

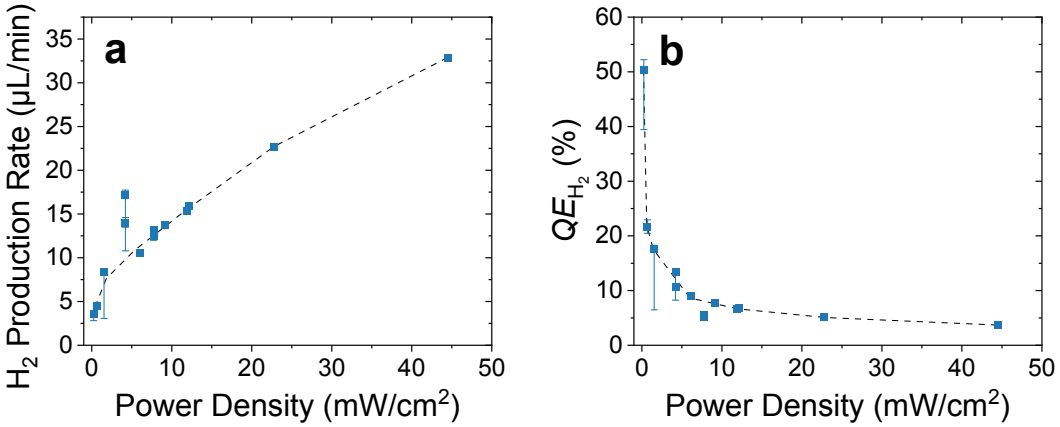

Figure 7.48: Normalized, power density-dependent hydrogen production rates (a) and quantum efficiencies in hydrogen production (b), after 2 h of illumination, determined by conducting steady-state hydrogen production measurements on MUA-capped, Pt-tipped CdSe/CdS DRs in the presence of IPA, combining measurements in the online reactor and cuvette setup. The dashed, black line is a guide to the eye, highlighting the exponential trend. As different setups and samples were used, the values in the cuvette setup were normalized to the calculated values in the reactor setup between $\sim$6 and 9 mW cm^{-2} (see Figure A17 for non-normalized data of different measurement series and Figure A18 for hydrogen production measurements).

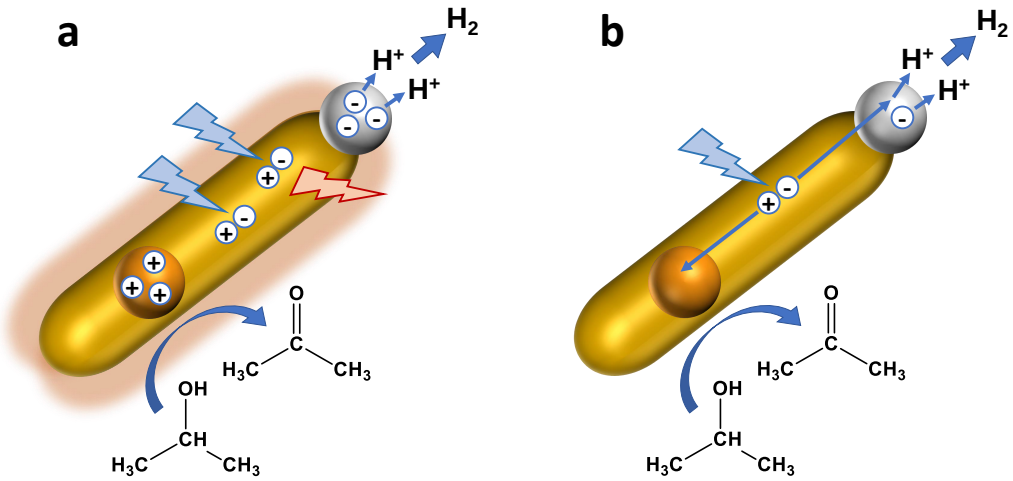

Figure 7.49: Scheme illustrating the differences in photocatalytic activity of Pt-tipped DRs at high (a) and low (b) power densities. At high power densities, greater proportion of the photogenerated charge carriers are lost to radiative and non-radiative charge recombination, which is favored by a reduced charge separation, resulting from charging of the Pt tip and CdSe core.

8 Conclusion

From correlating the charge carrier dynamics, photocatalytic activity, and colloidal stability of Pt-tipped CdSe/CdS DR nanocatalysts in the presence of different EDAs, it can be concluded that the photocatalytic activity of the nanocatalysts strongly depends on processes occurring at their surface. Conducting TA, time-resolved PL, and static spectroscopy, as well as steady-state hydrogen production, electron microscopy, and DLS measurements, it was found that EDAs interact differently with the NPs' surface and ligand shell. While the alcoholic EDAs (MeOH, EtOH, IPA) scavenge the holes diffusion-limited from the oxidized MUA ligand at the NPs' surface, the ionic EDAs (Na_2SO_3, Na_2S & Na_2SO_3, KOH & IPA, KOH & MeOH) are surface-active, which enables direct hole transfer onto the latter EDAs. Furthermore, it was revealed that the presence of the surface-active EDAs hydroxide and sulfide induces NP agglomeration. Analogously, illumination time- and power density-dependent measurements indicated the formation of NP agglomerates in the presence of alcoholic EDAs, resulting from ligand loss during solar-to-fuel conversion. The photocatalytic yield was found to increase by agglomeration, which was attributed to charge transfer between the connected NPs, resulting in improved spatial charge separation. Therefore, this study proposes a new conception of colloidal nanocatalysts, which does not regard them as isolated catalysts but rather as building blocks for assembling functional and structured catalyst networks.

Based on the presented insights, this work may encourage pursuing studies that aim to improve the photocatalytic yield. Given the revealed importance of processes occurring at the NPs' surface, modifications of the latter promise a significant improvement in the NPs' photocatalytic activity. For instance, alternative non-thiol-terminated ligands that do not trap the photogenerated holes could be used to stabilize the NPs in aqueous suspension. In the presence of these ligands, the direct hole transfer onto the EDA would not compete with a transfer onto the ligand and may therefore be resolvable *via* TA spectroscopy. Furthermore, the ligand would not degrade during the solar-to-fuel conversion process, resulting in a constant hydrogen production rate and colloidal stability of the NPs. However, the use of alternative ligands may impede network formation and reduce the sur-

face accessibility for the EDAs, causing low photocatalytic yields. Alternatively, ligands could be used that bind selectively to the metal or semiconductor domain and therefore favor the selective attachment of metal tips, forming metal domain junctions, which function as distinct reduction sites within the NP network. Another setscrew for improving the photocatalytic yield is the concentration of the introduced EDA, which should influence the assembly behavior of the nanocatalysts. Eventually, the gained insights may pave the way for large-scale applications of photocatalysts for solar-to-fuel conversion.

Bibliography

[1] Lewis, N. S.; Nocera, D. G. Powering the Planet: Chemical Challenges in Solar Energy Utilization. *Proceedings of the National Academy of Sciences* **2006**, *103*, 15729–15735.

[2] Squadrito, G.; Maggio, G.; Nicita, A. The Green Hydrogen Revolution. *Renewable Energy* **2023**, *216*, 119041.

[3] Hassan, Q.; Algburi, S.; Sameen, A. Z.; Salman, H. M.; Jaszczur, M. Green Hydrogen: A Pathway to a Sustainable Energy Future. *International Journal of Hydrogen Energy* **2024**, *50*, 310–333.

[4] Chatterjee, P.; Ambati, M. S. K.; Chakraborty, A. K.; Chakrabortty, S.; Biring, S.; Ramakrishna, S.; Wong, T. K. S.; Kumar, A.; Lawaniya, R.; Dalapati, G. K. Photovoltaic/Photo-Electrocatalysis Integration for Green Hydrogen: A Review. *Energy Conversion and Management* **2022**, *261*, 115648.

[5] Weller, H. Colloidal Semiconductor Q-Particles: Chemistry in the Transition Region Between Solid State and Molecules. *Angewandte Chemie International Edition in English* **1993**, *32*, 41–53.

[6] Weller, H. Quantized Semiconductor Particles: a Novel State of Matter for Materials Science. *Advanced Materials* **1993**, *5*, 88–95.

[7] Barhoum, A.; Makhlouf, A. S. H. *Emerging Applications of Nanoparticles and Architecture Nanostructures*; Elsevier, 2018.

[8] Ekimov, A. I. Quantum Size Effect in Three-Dimensional Microscopic Semiconductor Crystals. *Jetp Lett.* **1981**, *34*, 345.

[9] Rossetti, R.; Nakahara, S.; Brus, L. E. Quantum Size Effects in the Redox Potentials, Resonance Raman Spectra, and Electronic Spectra of CdS Crystallites in Aqueous Solution. *The Journal of Chemical Physics* **1983**, *79*, 1086–1088.

[10] Efros, A. L.; Efros, A. L. Interband Absorption of Light in a Semiconductor Sphere. *Sov. Phys. Semicond* **1982**, *16*, 772–775.

[11] Murray, C. B.; Norris, D. J.; Bawendi, M. G. Synthesis and Characterization of Nearly Monodisperse CdE (E= Sulfur, Selenium, Tellurium) Semiconductor Nanocrystallites. *Journal of the American Chemical Society* **1993**, *115*, 8706–8715.

[12] Peng, X.; Manna, L.; Yang, W.; Wickham, J.; Scher, E.; Kadavanich, A.; Alivisatos, A. P. Shape Control of CdSe Nanocrystals. *Nature* **2000**, *404*, 59–61.

[13] Alivisatos, A. P. Semiconductor Clusters, Nanocrystals, and Quantum Dots. *Science* **1996**, *271*, 933–937.

[14] Shu, Y.; Lin, X.; Qin, H.; Hu, Z.; Jin, Y.; Peng, X. Quantum Dots for Display Applications. *Angewandte Chemie* **2020**, *132*, 22496–22507.

[15] Talapin, D. V.; Lee, J.-S.; Kovalenko, M. V.; Shevchenko, E. V. Prospects of Colloidal Nanocrystals for Electronic and Optoelectronic Applications. *Chemical Reviews* **2010**, *110*, 389–458.

[16] García de Arquer, F. P.; Talapin, D. V.; Klimov, V. I.; Arakawa, Y.; Bayer, M.; Sargent, E. H. Semiconductor Quantum Dots: Technological Progress and Future Challenges. *Science* **2021**, *373*, eaaz8541.

[17] Zhou, Z.-Y.; Tian, N.; Li, J.-T.; Broadwell, I.; Sun, S.-G. Nanomaterials of High Surface Energy with Exceptional Properties in Catalysis and Energy Storage. *Chemical Society Reviews* **2011**, *40*, 4167–4185.

[18] Zaera, F. Nanostructured Materials for Applications in Heterogeneous Catalysis. *Chemical Society Reviews* **2013**, *42*, 2746–2762.

[19] Linic, S.; Christopher, P.; Ingram, D. B. Plasmonic-Metal Nanostructures for Efficient Conversion of Solar to Chemical Energy. *Nature Materials* **2011**, *10*, 911–921.

[20] McNamara, K.; Tofail, S. A. Nanoparticles in Biomedical Applications. *Advances in Physics: X* **2017**, *2*, 54–88.

[21] Liu, J.; Lau, S. K.; Varma, V. A.; Moffitt, R. A.; Caldwell, M.; Liu, T.; Young, A. N.; Petros, J. A.; Osunkoya, A. O.; Krogstad, T.; others Molecular Mapping of Tumor Heterogeneity on Clinical Tissue Specimens with Multiplexed Quantum Dots. *ACS Nano* **2010**, *4*, 2755–2765.

[22] The Nobel Prize in Chemistry 2023. https://www.nobelprize.org/prizes/chemistry/2023/summary/, Accessed: 2024-07-18.

[23] Moroz, P.; Boddy, A.; Zamkov, M. Challenges and Prospects of Photocatalytic Applications Utilizing Semiconductor Nanocrystals. *Frontiers in Chemistry* **2018**, *6*, 353.

[24] Wu, K.; Lian, T. Quantum Confined Colloidal Nanorod Heterostructures for Solar-to-Fuel Conversion. *Chemical Society Reviews* **2016**, *45*, 3781–3810.

[25] Ben-Shahar, Y.; Banin, U. Hybrid Semiconductor–Metal Nanorods as Photocatalysts. *Photoactive Semiconductor Nanocrystal Quantum Dots: Fundamentals and Applications* **2017**, 149–174.

[26] Amirav, L.; Alivisatos, A. P. Photocatalytic Hydrogen Production with Tunable Nanorod Heterostructures. *The Journal of Physical Chemistry Letters* **2010**, *1*, 1051–1054.

[27] Simon, T.; Carlson, M. T.; Stolarczyk, J. K.; Feldmann, J. Electron Transfer Rate vs Recombination Losses in Photocatalytic H_2 Generation on Pt-Decorated CdS Nanorods. *ACS Energy Letters* **2016**, *1*, 1137–1142.

[28] Nakibli, Y.; Kalisman, P.; Amirav, L. Less Is More: The Case of Metal Cocatalysts. *The Journal of Physical Chemistry Letters* **2015**, *6*, 2265–2268.

[29] Nakibli, Y.; Mazal, Y.; Dubi, Y.; Wächtler, M.; Amirav, L. Size Matters: Cocatalyst Size Effect on Charge Transfer and Photocatalytic Activity. *Nano Letters* **2018**, *18*, 357–364.

[30] Ben-Shahar, Y.; Scotognella, F.; Kriegel, I.; Moretti, L.; Cerullo, G.; Rabani, E.; Banin, U. Optimal Metal Domain Size for Photocatalysis with Hybrid Semiconductor-Metal Nanorods. *Nature Communications* **2016**, *7*, 10413.

[31] Amirav, L.; Alivisatos, A. P. Luminescence Studies of Individual Quantum Dot Photocatalysts. *Journal of the American Chemical Society* **2013**, *135*, 13049–13053.

[32] Kalisman, P.; Nakibli, Y.; Amirav, L. Perfect Photon-to-Hydrogen Conversion Efficiency. *Nano Letters* **2016**, *16*, 1776–1781.

[33] Zhu, H.; Song, N.; Lv, H.; Hill, C. L.; Lian, T. Near Unity Quantum Yield of Light-Driven Redox Mediator Reduction and Efficient H_2 Generation Using Colloidal Nanorod Heterostructures. *Journal of the American Chemical Society* **2012**, *134*, 11701–11708.

[34] Simon, T.; Bouchonville, N.; Berr, M. J.; Vaneski, A.; Adrović, A.; Volbers, D.; Wyrwich, R.; Döblinger, M.; Susha, A. S.; Rogach, A. L.; Jäckel, F.; Stolarczyk, J. K.; Feldmann, J. Redox Shuttle Mechanism Enhances Photocatalytic H_2 Generation on Ni-Decorated CdS Nanorods. *Nature Materials* **2014**, *13*, 1013–1018.

[35] Berr, M. J.; Wagner, P.; Fischbach, S.; Vaneski, A.; Schneider, J.; Susha, A. S.; Rogach, A. L.; Jäckel, F.; Feldmann, J. Hole Scavenger Redox Potentials Determine Quantum Efficiency and Stability of Pt-Decorated CdS Nanorods for Photocatalytic Hydrogen Generation. *Applied Physics Letters* **2012**, *100*, 223903.

[36] Schneider, J.; Bahnemann, D. W. Undesired Role of Sacrificial Reagents in Photocatalysis. *The Journal of Physical Chemistry Letters* **2013**, *4*, 3479–3483.

[37] Acharya, K. P.; Khnayzer, R. S.; O'Connor, T.; Diederich, G.; Kirsanova, M.; Klinkova, A.; Roth, D.; Kinder, E.; Imboden, M.; Zamkov, M. The Role of Hole Localization in Sacrificial Hydrogen Production by Semiconductor–Metal Heterostructured Nanocrystals. *Nano Letters* **2011**, *11*, 2919–2926.

[38] Wu, K.; Chen, Z.; Lv, H.; Zhu, H.; Hill, C. L.; Lian, T. Hole Removal Rate Limits Photodriven H_2 Generation Efficiency in CdS-Pt and CdSe/CdS-Pt Semiconductor Nanorod–Metal Tip Heterostructures. *Journal of the American Chemical Society* **2014**, *136*, 7708–7716.

[39] Cushing, B. L.; Kolesnichenko, V. L.; O'connor, C. J. Recent Advances in the Liquid-Phase Syntheses of Inorganic Nanoparticles. *Chemical Reviews* **2004**, *104*, 3893–3946.

[40] Jun, Y.-w.; Choi, J.-s.; Cheon, J. Shape Control of Semiconductor and Metal Oxide Nanocrystals Through Nonhydrolytic Colloidal Routes. *Angewandte Chemie International Edition* **2006**, *45*, 3414–3439.

[41] LaMer, V. K.; Dinegar, R. H. Theory, Production and Mechanism of Formation of Monodispersed Hydrosols. *Journal of the American Chemical Society* **1950**, *72*, 4847–4854.

[42] Thanh, N. T.; Maclean, N.; Mahiddine, S. Mechanisms of Nucleation and Growth of Nanoparticles in Solution. *Chemical Reviews* **2014**, *114*, 7610–7630.

[43] Cao, G. *Nanostructures & Nanomaterials: Synthesis, Properties & Applications*; Imperial College Press, 2004.

[44] Kwon, S. G.; Hyeon, T. Formation Mechanisms of Uniform Nanocrystals via Hot-Injection and Heat-Up Methods. *Small* **2011**, *7*, 2685–2702.

[45] Schulz, F.; Homolka, T.; Bastus, N. G.; Puntes, V.; Weller, H.; Vossmeyer, T. Little Adjustments Significantly Improve the Turkevich Synthesis of Gold Nanoparticles. *Langmuir* **2014**, *30*, 10779–10784.

[46] Ostwald, W. Über die vermeintliche Isomerie des roten und gelben Quecksilberoxyds und die Oberflächenspannung fester Körper. *Zeitschrift für Physikalische Chemie* **1900**, *34*, 495–503.

[47] Talapin, D. V.; Rogach, A. L.; Haase, M.; Weller, H. Evolution of an Ensemble of Nanoparticles in a Colloidal Solution: Theoretical Study. *The Journal of Physical Chemistry B* **2001**, *105*, 12278–12285.

[48] Whitehead, C. B.; Özkar, S.; Finke, R. G. LaMer's 1950 Model of Particle Formation: a Review and Critical Analysis of its Classical Nucleation and Fluctuation Theory Basis, of Competing Models and Mechanisms for Phase-Changes and Particle Formation, and Then of its Application to Silver Halide, Semiconductor, Metal, and Metal-Oxide Nanoparticles. *Materials Advances* **2021**, *2*, 186–235.

[49] Carbone, L. et al. Synthesis and Micrometer-Scale Assembly of Colloidal CdSe/CdS Nanorods Prepared by a Seeded Growth Approach. *Nano Letters* **2007**, *7*, 2942–2950.

[50] Gross, R.; Marx, A. *Festkörperphysik*; Oldenbourg Wissenschaftsverlag Verlag, 2012.

[51] Kittel, C.; McEuen, P. *Introduction to Solid State Physics*; John Wiley & Sons, 2018.

[52] West, A. R. *Solid State Chemistry and its Applications*; John Wiley & Sons, 2022.

[53] Huheey, J. E.; Keiter, E. A.; Keiter, R. L.; Medhi, O. K. *Inorganic Chemistry: Principles of Structure and Reactivity*; Pearson Education India, 2006.

[54] De Mello Donegá, C. Synthesis and Properties of Colloidal Heteronanocrystals. *Chemical Society Reviews* **2011**, *40*, 1512–1546.

[55] Fox, M. *Optical Properties of Solids*; Oxford University Press, 2010.

[56] Efros, A. L.; Brus, L. E. Nanocrystal Quantum Dots: From Discovery to Modern Development. *ACS Nano* **2021**, *15*, 6192–6210.

[57] Ekimov, A. I.; Hache, F.; Schanne-Klein, M.; Ricard, D.; Flytzanis, C.; Kudryavtsev, I.; Yazeva, T.; Rodina, A.; Efros, A. L. Absorption and Intensity-Dependent Photoluminescence Measurements on CdSe Quantum Dots: Assignment of the First Electronic Transitions. *JOSA B* **1993**, *10*, 100–107.

[58] Li, L.; Hu, J.; Yang, W.; Alivisatos, A. P. Band Gap Variation of Size-and Shape-Controlled Colloidal CdSe Quantum Rods. *Nano Letters* **2001**, *1*, 349–351.

[59] Peng, X.; Schlamp, M. C.; Kadavanich, A. V.; Alivisatos, A. P. Epitaxial Growth of Highly Luminescent CdSe/CdS Core/Shell Nanocrystals with Photostability and Electronic Accessibility. *Journal of the American Chemical Society* **1997**, *119*, 7019–7029.

[60] Brus, L. Electronic Wave Functions in Semiconductor Clusters: Experiment and Theory. *The Journal of Physical Chemistry* **1986**, *90*, 2555–2560.

[61] Wheeler, D. A.; Zhang, J. Z. Exciton Dynamics in Semiconductor Nanocrystals. *Advanced Materials* **2013**, *25*, 2878–2896.

[62] Talapin, D. V.; Nelson, J. H.; Shevchenko, E. V.; Aloni, S.; Sadtler, B.; Alivisatos, A. P. Seeded Growth of Highly Luminescent CdSe/CdS Nanoheterostructures with Rod and Tetrapod Morphologies. *Nano Letters* **2007**, *7*, 2951–2959.

[63] Diroll, B. T.; Guzelturk, B.; Po, H.; Dabard, C.; Fu, N.; Makke, L.; Lhuillier, E.; Ithurria, S. 2D II–VI Semiconductor Nanoplatelets: From Material Synthesis to Optoelectronic Integration. *Chemical Reviews* **2023**, *123*, 3543–3624.

[64] Bouet, C.; Tessier, M. D.; Ithurria, S.; Mahler, B.; Nadal, B.; Dubertret, B. Flat Colloidal Semiconductor Nanoplatelets. *Chemistry of Materials* **2013**, *25*, 1262–1271.

[65] O'Connor, T.; Panov, M. S.; Mereshchenko, A.; Tarnovsky, A. N.; Lorek, R.; Perera, D.; Diederich, G.; Lambright, S.; Moroz, P.; Zamkov, M. The Effect of the Charge-Separating Interface on Exciton Dynamics in Photocatalytic Colloidal Heteronanocrystals. *ACS Nano* **2012**, *6*, 8156–8165.

[66] Shulenberger, K. E.; Jilek, M. R.; Sherman, S. J.; Hohman, B. T.; Dukovic, G. Electronic Structure and Excited State Dynamics of Cadmium Chalcogenide Nanorods. *Chemical Reviews* **2023**, *123*, 3852–3903.

[67] Giansante, C.; Infante, I. Surface Traps in Colloidal Quantum Dots: a Combined Experimental and Theoretical Perspective. *The Journal of Physical Chemistry Letters* **2017**, *8*, 5209–5215.

[68] Houtepen, A. J.; Hens, Z.; Owen, J. S.; Infante, I. On the Origin of Surface Traps in Colloidal II–VI Semiconductor Nanocrystals. *Chemistry of Materials* **2017**, *29*, 752–761.

[69] Coropceanu, I.; Rossinelli, A.; Caram, J. R.; Freyria, F. S.; Bawendi, M. G. Slow-Injection Growth of Seeded CdSe/CdS Nanorods with Unity Fluorescence Quantum Yield and Complete Shell to Core Energy Transfer. *ACS Nano* **2016**, *10*, 3295–3301.

[70] Bryant, G. W.; Jaskolski, W. Surface Effects on Capped and Uncapped Nanocrystals. *The Journal of Physical Chemistry B* **2005**, *109*, 19650–19656.

[71] Efros, A. L. Almost Always Bright. *Nature Materials* **2008**, *7*, 612–613.

[72] Sitt, A.; Sala, F. D.; Menagen, G.; Banin, U. Multiexciton Engineering in Seeded Core/Shell Nanorods: Transfer from Type-I to Quasi-Type-II Regimes. *Nano Letters* **2009**, *9*, 3470–3476.

[73] Rainò, G.; Stöferle, T.; Moreels, I.; Gomes, R.; Kamal, J. S.; Hens, Z.; Mahrt, R. F. Probing the Wave Function Delocalization in CdSe/CdS Dot-in-Rod Nanocrystals by Time- and Temperature-Resolved Spectroscopy. *ACS Nano* **2011**, *5*, 4031–4036.

[74] Müller, J.; Lupton, J.; Lagoudakis, P.; Schindler, F.; Koeppe, R.; Rogach, A.; Feldmann, J.; Talapin, D.; Weller, H. Wave Function Engineering in Elongated Semiconductor Nanocrystals with Heterogeneous Carrier Confinement. *Nano Letters* **2005**, *5*, 2044–2049.

[75] Ben-Shahar, Y.; Stone, D.; Banin, U. Rich Landscape of Colloidal Semiconductor–Metal Hybrid Nanostructures: Synthesis, Synergetic Characteristics, and Emerging Applications. *Chemical Reviews* **2023**, *123*, 3790–3851.

[76] Grennell, A. N.; Utterback, J. K.; Pearce, O. M.; Wilker, M. B.; Dukovic, G. Relationships Between Exciton Dissociation and Slow Recombination Within ZnSe/CdS and CdSe/CdS Dot-in-Rod Heterostructures. *Nano Letters* **2017**, *17*, 3764–3774.

[77] Lakowicz, J. R. *Principles of Fluorescence Spectroscopy*; Springer, 2006.

[78] Berezin, M. Y.; Achilefu, S. Fluorescence Lifetime Measurements and Biological Imaging. *Chemical Reviews* **2010**, *110*, 2641–2684.

[79] Norris, D. J.; Bawendi, M. Measurement and Assignment of the Size-Dependent Optical Spectrum in CdSe Quantum Dots. *Physical Review B* **1996**, *53*, 16338.

[80] Atkins, P.; De Paula, J.; Keeler, J. *Atkins' Physical Chemistry*; Oxford University Press, 2023.

[81] Waiskopf, N.; Ben-Shahar, Y.; Banin, U. Photocatalytic Hybrid Semiconductor–Metal Nanoparticles; from Synergistic Properties to Emerging Applications. *Advanced Materials* **2018**, *30*, 1706697.

[82] Varghese, O. K.; Paulose, M.; LaTempa, T. J.; Grimes, C. A. High-Rate Solar Photocatalytic Conversion of CO_2 and Water Vapor to Hydrocarbon Fuels. *Nano Letters* **2009**, *9*, 731–737.

[83] Manzi, A.; Simon, T.; Sonnleitner, C.; Doblinger, M.; Wyrwich, R.; Stern, O.; Stolarczyk, J. K.; Feldmann, J. Light-Induced Cation Exchange for Copper Sulfide Based CO_2 Reduction. *Journal of the American Chemical Society* **2015**, *137*, 14007–14010.

[84] Banin, U.; Ben-Shahar, Y.; Vinokurov, K. Hybrid Semiconductor–Metal Nanoparticles: From Architecture to Function. *Chemistry of Materials* **2014**, *26*, 97–110.

[85] Van de Krol, R.; Grätzel, M. *Photoelectrochemical Hydrogen Production*; Springer, 2012.

[86] Dukovic, G.; Merkle, M. G.; Nelson, J. H.; Hughes, S. M.; Alivisatos, A. P. Photodeposition of Pt on Colloidal CdS and CdSe/CdS Semiconductor Nanostructures. *Advanced Materials* **2008**, *20*, 4306–4311.

[87] Harris, L. A.; Wilson, R. Semiconductors for Photoelectrolysis. *Annual Review of Materials Science* **1978**, *8*, 99–134.

[88] Yao, W.; Song, X.; Huang, C.; Xu, Q.; Wu, Q. Enhancing Solar Hydrogen Production via Modified Photochemical Treatment of Pt/CdS Photocatalyst. *Catalysis Today* **2013**, *199*, 42–47.

[89] Linsebigler, A. L.; Lu, G.; Yates Jr, J. T. Photocatalysis on TiO_2 Surfaces: Principles, Mechanisms, and Selected Results. *Chemical Reviews* **1995**, *95*, 735–758.

[90] Habas, S. E.; Yang, P.; Mokari, T. Selective Growth of Metal and Binary Metal Tips on CdS Nanorods. *Journal of the American Chemical Society* **2008**, *130*, 3294–3295.

[91] Menagen, G.; Macdonald, J. E.; Shemesh, Y.; Popov, I.; Banin, U. Au Growth on Semiconductor Nanorods: Photoinduced versus Thermal Growth Mechanisms. *Journal of the American Chemical Society* **2009**, *131*, 17406–17411.

[92] Nakibli, Y.; Amirav, L. Selective Growth of Ni Tips on Nanorod Photocatalysts. *Chemistry of Materials* **2016**, *28*, 4524–4527.

[93] Bala, T.; Sanyal, A.; Singh, A.; Kelly, D.; O'Sullivan, C.; Laffir, F.; Ryan, K. M. Silver Tip Formation on Colloidal CdSe Nanorods by a Facile Phase Transfer Protocol. *Journal of Materials Chemistry* **2011**, *21*, 6815–6820.

[94] Wächtler, M.; Kalisman, P.; Amirav, L. Charge-Transfer Dynamics in Nanorod Photocatalysts with Bimetallic Metal Tips. *The Journal of Physical Chemistry C* **2016**, *120*, 24491–24497.

[95] Yang, J.; Wang, D.; Han, H.; Li, C. Roles of Cocatalysts in Photocatalysis and Photoelectrocatalysis. *Accounts of Chemical Research* **2013**, *46*, 1900–1909.

[96] Sakata, T.; Kawai, T.; Hashimoto, K. Photochemical Diode Model of Pt/TiO_2 Particle and its Photocatalytic Activity. *Chemical Physics Letters* **1982**, *88*, 50–54.

[97] Wood, A.; Giersig, M.; Mulvaney, P. Fermi Level Equilibration in Quantum Dot- Metal Nanojunctions. *The Journal of Physical Chemistry B* **2001**, *105*, 8810–8815.

[98] Subramanian, V.; Wolf, E. E.; Kamat, P. V. Catalysis with TiO_2/Gold Nanocomposites. Effect of Metal Particle Size on the Fermi Level Equilibration. *Journal of the American Chemical Society* **2004**, *126*, 4943–4950.

[99] Schlenkrich, J.; Zámbó, D.; Schlosser, A.; Rusch, P.; Bigall, N. C. Revealing the Effect of Nanoscopic Design on the Charge Carrier Separation Processes in Semiconductor-Metal Nanoparticle Gel Networks. *Advanced Optical Materials* **2022**, *10*, 2101712.

[100] Choi, J. Y.; Park, W.-W.; Park, B.; Sul, S.; Kwon, O.-H.; Song, H. Optimal Length of Hybrid Metal–Semiconductor Nanorods for Photocatalytic Hydrogen Generation. *ACS Catalysis* **2021**, *11*, 13303–13311.

[101] Bridewell, V. L.; Alam, R.; Karwacki, C. J.; Kamat, P. V. CdSe/CdS Nanorod Photocatalysts: Tuning the Interfacial Charge Transfer Process Through Shell Length. *Chemistry of Materials* **2015**, *27*, 5064–5071.

[102] Diroll, B. T.; Turk, M. E.; Gogotsi, N.; Murray, C. B.; Kikkawa, J. M. Ultrafast Photoluminescence from the Core and the Shell in CdSe/CdS Dot-in-Rod Heterostructures. *ChemPhysChem* **2016**, *17*, 759–765.

[103] Wengler-Rust, S.; Staechelin, Y. U.; Lange, H.; Weller, H. Electron Donor-Specific Surface Interactions Promote the Photocatalytic Activity of Metal-Semiconductor Nanohybrids. *Small* **2024**, *20*, 2401388.

[104] Wolff, C. M.; Frischmann, P. D.; Schulze, M.; Bohn, B. J.; Wein, R.; Livadas, P.; Carlson, M. T.; Jäckel, F.; Feldmann, J.; Würthner, F.; Stolarczyk, J. K. All-in-one Visible-Light-Driven Water Splitting by Combining Nanoparticulate and Molecular Co-Catalysts on CdS Nanorods. *Nature Energy* **2018**, *3*, 862–869.

[105] Maeda, K.; Domen, K. Photocatalytic Water Splitting: Recent Progress and Future Challenges. *The Journal of Physical Chemistry Letters* **2010**, *1*, 2655–2661.

[106] Wenderich, K.; Mul, G. Methods, Mechanism, and Applications of Photodeposition in Photocatalysis: a Review. *Chemical Reviews* **2016**, *116*, 14587–14619.

[107] Wang, C.-y.; Pagel, R.; Dohrmann, J. K.; Bahnemann, D. W. Antenna Mechanism and Deaggregation Concept: Novel Mechanistic Principles for Photocatalysis. *Comptes Rendus Chimie* **2006**, *9*, 761–773.

[108] Kumaravel, V.; Imam, M. D.; Badreldin, A.; Chava, R. K.; Do, J. Y.; Kang, M.; Abdel-Wahab, A. Photocatalytic Hydrogen Production: Role of Sacrificial Reagents on the Activity of Oxide, Carbon, and Sulfide Catalysts. *Catalysts* **2019**, *9*, 276.

[109] Berr, M.; Vaneski, A.; Susha, A. S.; Rodríguez-Fernández, J.; Döblinger, M.; Jäckel, F.; Rogach, A. L.; Feldmann, J. Colloidal CdS Nanorods Decorated with Subnanometer Sized Pt Clusters for Photocatalytic Hydrogen Generation. *Applied Physics Letters* **2010**, *97*.

[110] Kandiel, T. A.; Dillert, R.; Bahnemann, D. W. Enhanced Photocatalytic Production of Molecular Hydrogen on TiO_2 Modified with Pt–Polypyrrole Nanocomposites. *Photochemical & Photobiological Sciences* **2009**, *8*, 683–690.

[111] Kaneko, M.; Nemoto, J.; Ueno, H.; Gokan, N.; Ohnuki, K.; Horikawa, M.; Saito, R.; Shibata, T. Photoelectrochemical Reaction of Biomass and Bio-Related Compounds with Nanoporous TiO_2 Film Photoanode and O_2-Reducing Cathode. *Electrochemistry Communications* **2006**, *8*, 336–340.

[112] Das, T. N.; Huie, R. E.; Neta, P. Reduction Potentials of $SO_3^{\bullet -}$, $SO_5^{\bullet -}$, and $S_4O_6^{\bullet 3-}$ Radicals in Aqueous Solution. *The Journal of Physical Chemistry A* **1999**, *103*, 3581–3588.

[113] Wardman, P. Reduction Potentials of One-Electron Couples Involving Free Radicals in Aqueous Solution. *Journal of Physical and Chemical Reference Data* **1989**, *18*, 1637–1755.

[114] Armstrong, D. A.; Huie, R. E.; Koppenol, W. H.; Lymar, S. V.; Merényi, G.; Neta, P.; Ruscic, B.; Stanbury, D. M.; Steenken, S.; Wardman, P. Standard Electrode Potentials Involving Radicals in Aqueous Solution: Inorganic Radicals (IUPAC Technical Report). *Pure and Applied Chemistry* **2015**, *87*, 1139–1150.

[115] Koppenol, W.; Rush, J. Reduction Potential of the Carbon Dioxide/Carbon Dioxide Radical Anion: a Comparison With Other C1 Radicals. *Journal of Physical Chemistry* **1987**, *91*, 4429–4430.

[116] Nakamatsu, H.; Kawai, T.; Koreeda, A.; Kawai, S. Electron-Microscopic Observation of Photodeposited Pt on TiO_2 Particles in Relation to Photocatalytic Activity. *Journal of the Chemical Society, Faraday Transactions 1: Physical Chemistry in Condensed Phases* **1986**, *82*, 527–531.

[117] Rao, P.; Hayon, E. Redox Potentials of Free Radicals. I. Simple Organic Radicals. *Journal of the American Chemical Society* **1974**, *96*, 1287–1294.

[118] Kalamaras, E.; Lianos, P. Current Doubling Effect Revisited: Current Multiplication in a PhotoFuelCell. *Journal of Electroanalytical Chemistry* **2015**, *751*, 37–42.

[119] Morrison, S.; Freund, T. Chemical Role of Holes and Electrons in ZnO Photocatalysis. *The Journal of Chemical Physics* **1967**, *47*, 1543–1551.

[120] Maeda, Y.; Fujishima, A.; Honda, K. The Investigation of Current Doubling Reactions on Semiconductor Photoelectrodes by Temperature Change Measurements. *Journal of The Electrochemical Society* **1981**, *128*, 1731.

[121] Lee, J.-s.; Kato, T.; Fujishima, A.; Honda, K. Photoelectrochemical Oxidation of Alcohols on Polycrystalline Zinc Oxide. *Bulletin of the Chemical Society of Japan* **1984**, *57*, 1179–1183.

[122] Herrasti, P.; Peter, L. Photocurrent Doubling During the Oxidation of Formic Acid at n-CdS: An Investigation by Intensity Modulated Photocurrent Spectroscopy. *Journal of Electroanalytical Chemistry and Interfacial Electrochemistry* **1991**, *305*, 241–258.

[123] Memming, R. *Electron Transfer I: Photoinduced Charge Transfer Processes at Semiconductor Electrodes and Particles*; Springer, 2005; pp 105–181.

[124] Gao, R.; Safrany, A.; Rabani, J. Fundamental Reactions in TiO_2 Nanocrystallite Aqueous Solutions Studied by Pulse Radiolysis. *Radiation Physics and Chemistry* **2002**, *65*, 599–609.

[125] Nosaka, Y.; Sasaki, H.; Norimatsu, K.; Miyama, H. Effect of Surface Compound Formation on the Photo-Induced Reaction at Polycrystalline TiO_2 Semiconductor Electrodes. *Chemical Physics Letters* **1984**, *105*, 456–458.

[126] Hykaway, N.; Sears, W.; Morisaki, H.; Morrison, S. R. Current-Doubling Reactions on Titanium Dioxide Photoanodes. *The Journal of Physical Chemistry* **1986**, *90*, 6663–6667.

[127] Wang, W.; Banerjee, S.; Jia, S.; Steigerwald, M. L.; Herman, I. P. Ligand Control of Growth, Morphology, and Capping Structure of Colloidal CdSe Nanorods. *Chemistry of Materials* **2007**, *19*, 2573–2580.

[128] Talapin, D. V.; Rogach, A. L.; Kornowski, A.; Haase, M.; Weller, H. Highly Luminescent Monodisperse CdSe and CdSe/ZnS Nanocrystals Synthesized in a Hexadecylamine- Trioctylphosphine Oxide- Trioctylphospine Mixture. *Nano Letters* **2001**, *1*, 207–211.

[129] Rogach, A. L.; Kornowski, A.; Gao, M.; Eychmüller, A.; Weller, H. Synthesis and Characterization of a Size Series of Extremely Small Thiol-Stabilized CdSe Nanocrystals. *The Journal of Physical Chemistry B* **1999**, *103*, 3065–3069.

[130] Manna, L.; Scher, E. C.; Alivisatos, A. P. Synthesis of Soluble and Processable Rod-, Arrow-, Teardrop-, and Tetrapod-Shaped CdSe Nanocrystals. *Journal of the American Chemical Society* **2000**, *122*, 12700–12706.

[131] Menagen, G.; Mocatta, D.; Salant, A.; Popov, I.; Dorfs, D.; Banin, U. Selective Gold Growth on CdSe Seeded CdS Nanorods. *Chemistry of Materials* **2008**, *20*, 6900–6902.

[132] Diroll, B. T.; Gogotsi, N.; Murray, C. B. Statistical Description of CdSe/CdS Dot-in-Rod Heterostructures Using Scanning Transmission Electron Microscopy. *Chemistry of Materials* **2016**, *28*, 3345–3351.

[133] Dimitrijevic, J.; Krapf, L.; Wolter, C.; Schmidtke, C.; Merkl, J.-P.; Jochum, T.; Kornowski, A.; Schüth, A.; Gebert, A.; Hüttmann, G.; Vossmeyer, T.; Weller, H. CdSe/CdS-Quantum Rods: Fluorescent Probes for *in vivo* Two-Photon Laser Scanning Microscopy. *Nanoscale* **2014**, *6*, 10413–10422.

[134] Peng, Z. A.; Peng, X. Mechanisms of the Shape Evolution of CdSe Nanocrystals. *Journal of the American Chemical Society* **2001**, *123*, 1389–1395.

[135] Borys, N. J.; Walter, M. J.; Huang, J.; Talapin, D. V.; Lupton, J. M. The Role of Particle Morphology in Interfacial Energy Transfer in CdSe/CdS Heterostructure Nanocrystals. *Science* **2010**, *330*, 1371–1374.

[136] Wu, K.; Rodriguez-Cordoba, W. E.; Liu, Z.; Zhu, H.; Lian, T. Beyond Band Alignment: Hole Localization Driven Formation of Three Spatially Separated Long-Lived Exciton States in CdSe/CdS Nanorods. *ACS Nano* **2013**, *7*, 7173–7185.

[137] Perkampus, H.-H. *UV-VIS Spectroscopy and its Applications*; Springer Science & Business Media, 2013.

[138] Bisht, P. B. *An Introduction to Photonics and Laser Physics with Applications*; IOP Publishing, 2022.

[139] Leatherdale, C. A.; Woo, W.-K.; Mikulec, F. V.; Bawendi, M. G. On the Absorption Cross Section of CdSe Nanocrystal Quantum Dots. *The Journal of Physical Chemistry B* **2002**, *106*, 7619–7622.

[140] O'Connor, D. *Time-Correlated Single Photon Counting*; Academic Press, 2012.

[141] Resch-Genger, U.; Grabolle, M.; Cavaliere-Jaricot, S.; Nitschke, R.; Nann, T. Quantum Dots Versus Organic Dyes as Fluorescent Labels. *Nature Methods* **2008**, *5*, 763–775.

[142] Valeur, B.; Berberan-Santos, M. N. *Molecular Fluorescence: Principles and Applications*; John Wiley & Sons, 2013.

[143] Fišerová, E.; Kubala, M. Mean Fluorescence Lifetime and its Error. *Journal of Luminescence* **2012**, *132*, 2059–2064.

[144] Omogo, B.; Gao, F.; Bajwa, P.; Kaneko, M.; Heyes, C. D. Reducing Blinking in Small Core–Multishell Quantum Dots by Carefully Balancing Confinement Potential and Induced Lattice Strain: the "Goldilocks" Effect. *ACS Nano* **2016**, *10*, 4072–4082.

[145] Zatryb, G.; Klak, M. On the Choice of Proper Average Lifetime Formula for an Ensemble of Emitters Showing Non-Single Exponential Photoluminescence Decay. *Journal of Physics: Condensed Matter* **2020**, *32*, 415902.

[146] Ariese, F.; Roy, K.; Ravi Kumar, V.; Sudeeksha, H. C.; Kayal, S.; Umapathy, S. Time-Resolved Spectroscopy: Instrumentation and Applications. *Encyclopedia of Analytical Chemistry: Applications, Theory and Instrumentation* **2006**, 1–55.

[147] Lupo, M. G.; Della Sala, F.; Carbone, L.; Zavelani-Rossi, M.; Fiore, A.; Lüer, L.; Polli, D.; Cingolani, R.; Manna, L.; Lanzani, G. Ultrafast Electron–Hole Dynamics in Core/Shell CdSe/CdS Dot/Rod Nanocrystals. *Nano Letters* **2008**, *8*, 4582–4587.

[148] Wu, K.; Zhu, H.; Liu, Z.; Rodríguez-Córdoba, W.; Lian, T. Ultrafast Charge Separation and Long-Lived Charge Separated State in Photocatalytic CdS–Pt Nanorod Heterostructures. *Journal of the American Chemical Society* **2012**, *134*, 10337–10340.

[149] Wu, K.; Zhu, H.; Lian, T. Ultrafast Exciton Dynamics and Light-Driven H_2 Evolution in Colloidal Semiconductor Nanorods and Pt-Tipped Nanorods. *Accounts of Chemical Research* **2015**, *48*, 851–859.

[150] Adel, P.; Bloh, J.; Hinrichs, D.; Kodanek, T.; Dorfs, D. Determination of all Dimensions of CdSe Seeded CdS Nanorods Solely via their UV/Vis Spectra. *Zeitschrift für Physikalische Chemie* **2017**, *231*, 93–106.

[151] Costi, R.; Saunders, A. E.; Elmalem, E.; Salant, A.; Banin, U. Visible Light-Induced Charge Retention and Photocatalysis with Hybrid CdSe–Au Nanodumbbells. *Nano Letters* **2008**, *8*, 637–641.

[152] Jasieniak, J.; Smith, L.; Van Embden, J.; Mulvaney, P.; Califano, M. Re-Examination of the Size-Dependent Absorption Properties of CdSe Quantum Dots. *The Journal of Physical Chemistry C* **2009**, *113*, 19468–19474.

[153] Rurack, K.; Spieles, M. Fluorescence Quantum Yields of a Series of Red and Near-Infrared Dyes Emitting at 600- 1000 nm. *Analytical Chemistry* **2011**, *83*, 1232–1242.

[154] Fischli, D.; Enders, F.; Boldt, K. Kinetically Driven Cadmium Chalcogenide Nanorod Growth Fed by Local Cluster Aggregates. *The Journal of Physical Chemistry C* **2020**, *124*, 12774–12783.

[155] Jiang, Z.-J.; Kelley, D. F. Role of Magic-Sized Clusters in the Synthesis of CdSe Nanorods. *ACS Nano* **2010**, *4*, 1561–1572.

[156] Kirkwood, N.; Boldt, K. Protic Additives Determine the Pathway of CdSe Nanocrystal Growth. *Nanoscale* **2018**, *10*, 18238–18248.

[157] Siegrist, T. *X-Ray Structure Analysis*; Walter de Gruyter GmbH & Co KG, 2021.

[158] Bunge, H. Influence of Texture on Powder Diffraction. *Texture, Stress, and Microstructure* **1997**, *29*, 1–26.

[159] Ulrich, F.; Zachariasen, W. XIV. Über die Kristallstruktur des α- und β-CdS, sowie des Wurtzits. *Zeitschrift für Kristallographie-Crystalline Materials* **1925**, *62*, 260–273.

[160] Swanson, H. E.; Gilfrich, N. T.; Cook, M. I. *Standard X-ray Diffraction Powder Patterns*; National Bureau of Standards Circular 539, 1957.

[161] Hull, A. W. X-Ray Crystal Analysis of Thirteen Common Metals. *Physical Review* **1921**, *17*, 571.

[162] Liu, Y.; Yang, W.; Chen, Q.; Cullen, D. A.; Xie, Z.; Lian, T. Pt Particle Size Affects Both the Charge Separation and Water Reduction Efficiencies of CdS–Pt Nanorod Photocatalysts for Light Driven H_2 Generation. *Journal of the American Chemical Society* **2022**, *144*, 2705–2715.

[163] Brown, K. A.; Wilker, M. B.; Boehm, M.; Dukovic, G.; King, P. W. Characterization of Photochemical Processes for H_2 Production by CdS Nanorod–[FeFe] Hydrogenase Complexes. *Journal of the American Chemical Society* **2012**, *134*, 5627–5636.

[164] Mohamed, N. B. H.; Haouari, M.; Zaaboub, Z.; Hassen, F.; Maaref, H.; Ouada, H. B. Effect of Surface on the Optical Structure and Thermal Properties of Organically Capped CdS Nanoparticles. *Journal of Physics and Chemistry of Solids* **2014**, *75*, 936–944.

[165] She, C.; Demortiere, A.; Shevchenko, E. V.; Pelton, M. Using Shape to Control Photoluminescence from CdSe/CdS Core/Shell Nanorods. *The Journal of Physical Chemistry Letters* **2011**, *2*, 1469–1475.

[166] Aldana, J.; Wang, Y. A.; Peng, X. Photochemical Instability of CdSe Nanocrystals Coated by Hydrophilic Thiols. *Journal of the American Chemical Society* **2001**, *123*, 8844–8850.

[167] Liu, Y.; Cullen, D. A.; Lian, T. Slow Auger Recombination of Trapped Excitons Enables Efficient Multiple Electron Transfer in CdS–Pt Nanorod Heterostructures. *Journal of the American Chemical Society* **2021**, *143*, 20264–20273.

[168] Vazquez, G.; Alvarez, E.; Cancela, A.; Navaza, J. M. Density, Viscosity, and Surface Tension of Aqueous Solutions of Sodium Sulfite and Sodium Sulfite + Sucrose from 25 to 40 °C. *Journal of Chemical and Engineering Data* **1995**, *40*, 1101–1105.

[169] Spanhel, L.; Haase, M.; Weller, H.; Henglein, A. Photochemistry of Colloidal Semiconductors. 20. Surface Modification and Stability of Strong Luminescing CdS Particles. *Journal of the American Chemical Society* **1987**, *109*, 5649–5655.

[170] Weller, H.; Haase, M.; Spanhel, L.; Henglein, A. Charge Carrier Dynamics in Colloidal Semiconductors. *Trends in Colloid and Interface Science II* **1988**, 24–26.

[171] Westmoreland, D. E.; Nap, R. J.; Arcudi, F.; Szleifer, I.; Weiss, E. A. pH-Dependent Structure of Water-Exposed Surfaces of CdSe Quantum Dots. *Chemical Communications* **2019**, *55*, 5435–5438.

[172] Boyle, T. J.; Bunge, S. D.; Alam, T. M.; Holland, G. P.; Headley, T. J.; Avilucea, G. Cadmium Amido Alkoxide and Alkoxide Precursors for the Synthesis of Nanocrystalline CdE (E= S, Se, Te). *Inorganic Chemistry* **2005**, *44*, 1309–1318.

[173] Jana, S.; Pape, T.; Mitzel, N. W. Simple Methylcadmium Alkoxides. *Zeitschrift für Naturforschung B* **2007**, *62*, 1339–1342.

[174] Zhu, H.; Song, N.; Lian, T. Charging of Quantum Dots by Sulfide Redox Electrolytes Reduces Electron Injection Efficiency in Quantum Dot Sensitized Solar Cells. *Journal of the American Chemical Society* **2013**, *135*, 11461–11464.

[175] Chakrapani, V.; Baker, D.; Kamat, P. V. Understanding the Role of the Sulfide Redox Couple (S^{2-}/S_n^{2-}) in Quantum Dot-Sensitized Solar Cells. *Journal of the American Chemical Society* **2011**, *133*, 9607–9615.

[176] Sekhar, M. C.; Santhosh, K.; Praveen Kumar, J.; Mondal, N.; Soumya, S.; Samanta, A. CdTe Quantum Dots in Ionic Liquid: Stability and Hole scavenging in the Presence of a Sulfide Salt. *The Journal of Physical Chemistry C* **2014**, *118*, 18481–18487.

[177] Chen, K. L.; Mylon, S. E.; Elimelech, M. Aggregation Kinetics of Alginate-Coated Hematite Nanoparticles in Monovalent and Divalent Electrolytes. *Environmental Science & Technology* **2006**, *40*, 1516–1523.

[178] Gregory, J. Monitoring Particle Aggregation Processes. *Advances in Colloid and Interface Science* **2009**, *147*, 109–123.

[179] Otto, F.; Sun, X.; Schulz, F.; Sanchez-Cano, C.; Feliu, N.; Westermeier, F.; Parak, W. J. X-Ray Photon Correlation Spectroscopy Towards Measuring Nanoparticle Diameters in Biological Environments Allowing for the In Situ Analysis of their Bio-Nano Interface. *Small* **2022**, *18*, 2201324.

[180] Mulvihill, M. J.; Habas, S. E.; Jen-La Plante, I.; Wan, J.; Mokari, T. Influence of Size, Shape, and Surface Coating on the Stability of Aqueous Suspensions of CdSe Nanoparticles. *Chemistry of Materials* **2010**, *22*, 5251–5257.

[181] Schlenkrich, J.; Lübkemann-Warwas, F.; Graf, R. T.; Wesemann, C.; Schoske, L.; Rosebrock, M.; Hindricks, K. D.; Behrens, P.; Bahnemann, D. W.; Dorfs, D.; Bigall, N. C. Investigation of the Photocatalytic Hydrogen Production of Semiconductor Nanocrystal-Based Hydrogels. *Small* **2023**, *19*, 2208108.

[182] Rosebrock, M.; Zámbó, D.; Rusch, P.; Pluta, D.; Steinbach, F.; Bessel, P.; Schlosser, A.; Feldhoff, A.; Hindricks, K. D.; Behrens, P.; Dorfs, D.; Bigall, N. C. Spatial Extent of Fluorescence Quenching in Mixed Semiconductor–Metal Nanoparticle Gel Networks. *Advanced Functional Materials* **2021**, *31*, 2101628.

[183] Wang, C.-y.; Böttcher, C.; Bahnemann, D. W.; Dohrmann, J. K. A Comparative Study of Nanometer Sized Fe(III)-Doped TiO_2 Photocatalysts: Synthesis, Characterization and Activity. *Journal of Materials Chemistry* **2003**, *13*, 2322–2329.

[184] Lakshminarasimhan, N.; Kim, W.; Choi, W. Effect of the Agglomerated State on the Photocatalytic Hydrogen Production with in Situ Agglomeration of Colloidal TiO_2 Nanoparticles. *The Journal of Physical Chemistry C* **2008**, *112*, 20451–20457.

[185] Wang, C.-y.; Böttcher, C.; Bahnemann, D. W.; Dohrmann, J. K. In Situ Electron Microscopy Investigation of Fe(III)-Doped TiO_2 Nanoparticles in an Aqueous Environment. *Journal of Nanoparticle Research* **2004**, *6*, 119–122.

[186] Friedmann, D.; Hansing, H.; Bahnemann, D. Primary Processes During the Photodeposition of Ag Clusters on TiO_2 Nanoparticles. *Zeitschrift für Physikalische Chemie* **2007**, *221*, 329–348.

[187] Sieland, F.; Schneider, J.; Lippmann, T.; Bahnemann, D. W. Understanding Charge Transfer Processes on Metal Oxides: a Laser-Flash-Photolysis Study. Solar Hydrogen and Nanotechnology XI. 2016; pp 21–30.

[188] Chen, Y.; Amirav, L. Shape Tunability of Copper Nanocrystals Deposited on Nanorods. *Chemical Science* **2023**, *14*, 7512.

[189] Morgan, D. P.; Kelley, D. F. What Does the Transient Absorption Spectrum of CdSe Quantum Dots Measure? *The Journal of Physical Chemistry C* **2020**, *124*, 8448–8455.

[190] Grimaldi, G.; Geuchies, J. J.; Van Der Stam, W.; Du Fossé, I.; Brynjarsson, B.; Kirkwood, N.; Kinge, S.; Siebbeles, L. D.; Houtepen, A. J. Spectroscopic Evidence for the Contribution of Holes to the Bleach of Cd-Chalcogenide Quantum Dots. *Nano Letters* **2019**, *19*, 3002–3010.

[191] Taheri, M. M.; Elbert, K. C.; Yang, S.; Diroll, B. T.; Park, J.; Murray, C. B.; Baxter, J. B. Distinguishing Electron and Hole Dynamics in Functionalized CdSe/CdS Core/Shell Quantum Dots Using Complementary Ultrafast Spectroscopies and Kinetic Modeling. *The Journal of Physical Chemistry C* **2020**, *125*, 31–41.

[192] Olshansky, J. H.; Ding, T. X.; Lee, Y. V.; Leone, S. R.; Alivisatos, A. P. Hole Transfer from Photoexcited Quantum Dots: The Relationship Between Driving Force and Rate. *Journal of the American Chemical Society* **2015**, *137*, 15567–15575.

[193] Schulz, F.; Dahl, G. T.; Besztejan, S.; Schroer, M. A.; Lehmkühler, F.; Grübel, G.; Vossmeyer, T.; Lange, H. Ligand Layer Engineering to Control Stability and Interfacial Properties of Nanoparticles. *Langmuir* **2016**, *32*, 7897–7907.

[194] Schulz, F.; Vossmeyer, T.; Bastús, N. G.; Weller, H. Effect of the Spacer Structure on the Stability of Gold Nanoparticles Functionalized with Monodentate Thiolated Poly(ethylene glycol) Ligands. *Langmuir* **2013**, *29*, 9897–9908.

[195] Schulz, F.; Friedrich, W.; Hoppe, K.; Vossmeyer, T.; Weller, H.; Lange, H. Effective PEGylation of Gold Nanorods. *Nanoscale* **2016**, *8*, 7296–7308.

[196] Haynes, W. M. *CRC Handbook of Chemistry and Physics*; CRC Press, 2014.

[197] Lilie, J.; Beck, G.; Henglein, A. Pulsradiolyse und Polarographie: Halbstufenpotentiale für die Oxydation und Reduktion von kurzlebigen organischen Radikalen an der Hg-Elektrode. *Berichte der Bunsengesellschaft für physikalische Chemie* **1971**, *75*, 458–465.

[198] Buehler, N.; Meier, K.; Reber, J. F. Photochemical Hydrogen Production with Cadmium Sulfide Suspensions. *The Journal of Physical Chemistry* **1984**, *88*, 3261–3268.

[199] Franceschetti, A.; Zunger, A. Optical Transitions in Charged CdSe Quantum Dots. *Physical Review B* **2000**, *62*, R16287.

[200] Radich, E. J.; Dwyer, R.; Kamat, P. V. Cu_2S Reduced Graphene Oxide Composite for High-Efficiency Quantum Dot Solar Cells. Overcoming the Redox Limitations of S_2^-/S_n^{2-} at the Counter Electrode. *The Journal of Physical Chemistry Letters* **2011**, *2*, 2453–2460.

[201] Loučka, T. Adsorption and Oxidation of Organic Compounds on a Platinum Electrode Partly Covered by Adsorbed Sulphur. *Journal of Electroanalytical Chemistry and Interfacial Electrochemistry* **1972**, *36*, 355–367.

[202] Chaveanghong, S.; Nakamura, T.; Takagi, Y.; Cagnon, B.; Uruga, T.; Tada, M.; Iwasawa, Y.; Yokoyama, T. Sulfur Poisoning of Pt and PtCo Anode and Cathode Catalysts in Polymer Electrolyte Fuel Cells Studied by Operando Near Ambient Pressure Hard X-Ray Photoelectron Spectroscopy. *Physical Chemistry Chemical Physics* **2021**, *23*, 3866–3873.

[203] Sethuraman, V. A.; Weidner, J. W. Analysis of Sulfur Poisoning on a PEM Fuel Cell Electrode. *Electrochimica Acta* **2010**, *55*, 5683–5694.

[204] Honkanen, M.; Huuhtanen, M.; Kärkkäinen, M.; Kanerva, T.; Lahtonen, K.; Väliheikki, A.; Kallinen, K.; Keiski, R. L.; Vippola, M. Characterization of Pt-Based Oxidation Catalyst–Deactivated Simultaneously by Sulfur and Phosphorus. *Journal of Catalysis* **2021**, *397*, 183–191.

[205] Serjeant, E. P.; Dempsey, B.; others Ionisation Constants of Organic Acids in Aqueous Solution. *IUPAC Chemical Data Series* **1979**, *23*, 160–190.

[206] Hecht, E. *Optics*; Pearson Education, 2012.

[207] Bruice, P. Y. *Organic Chemistry*; Pearson, 2017.

[208] Riedel, E.; Janiak, C. *Anorganische Chemie*; De Gruyter, 2022.

[209] Merck. Safety Data Sheets. `https://www.sigmaaldrich.com`, Accessed: 2024-08-12.

[210] Institut für Arbeitsschutz der Deutschen Gesetzlichen Unfallversicherung. List of carcinogenic, mutagenic and reprotoxic substances (CMR substances). `https://publikationen.dguv.de/widgets/pdf/download/article/4766`, Accessed: 2024-08-12.

A Appendix

A1 Nanoparticle Synthesis

A1.1 Absorbance Spectra

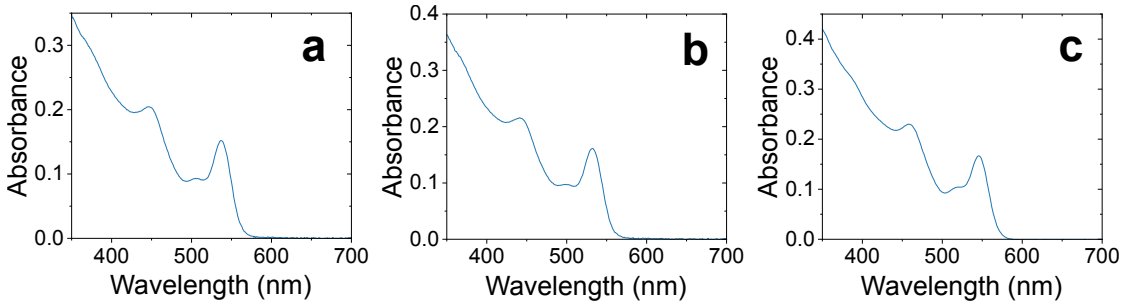

Figure A1: Static absorbance spectra of CdSe NPs of different sizes, of arbitrary concentration, with phosphonate ligands in toluene, recorded in a spectrometer with a linear beam path. The diameter of the NPs was calculated from the first excitonic peak (2.95 nm (a), 2.87 nm (b), and 3.10 nm (c); see Table 7.1 for synthesis parameters and calculated NP diameters).

A1.2 Dimensions of Synthesized CdSe/CdS Dot-in-Rods

Table A1: Dimensions, aspect ratio and volume of additional batches of CdSe/CdS DRs used in this work. The dimensions of the DRs were determined from TEM micrographs (see Figure A2f-i). An exemplary histogram showing the distribution in length and diameter of a DR batch is shown in Figure A3.

Seed Diameter (nm)	Length (nm)	Diameter (nm)	Aspect Ratio	Volume (nm^3)
2.95	34.3 ± 2.2	4.6 ± 0.4	7.5	570
2.30	36.7 ± 2.7	4.2 ± 0.3	8.7	508
2.30	29.3 ± 3.4	4.1 ± 0.4	7.1	387
2.30	28.9 ± 3.6	4.2 ± 0.4	6.9	400

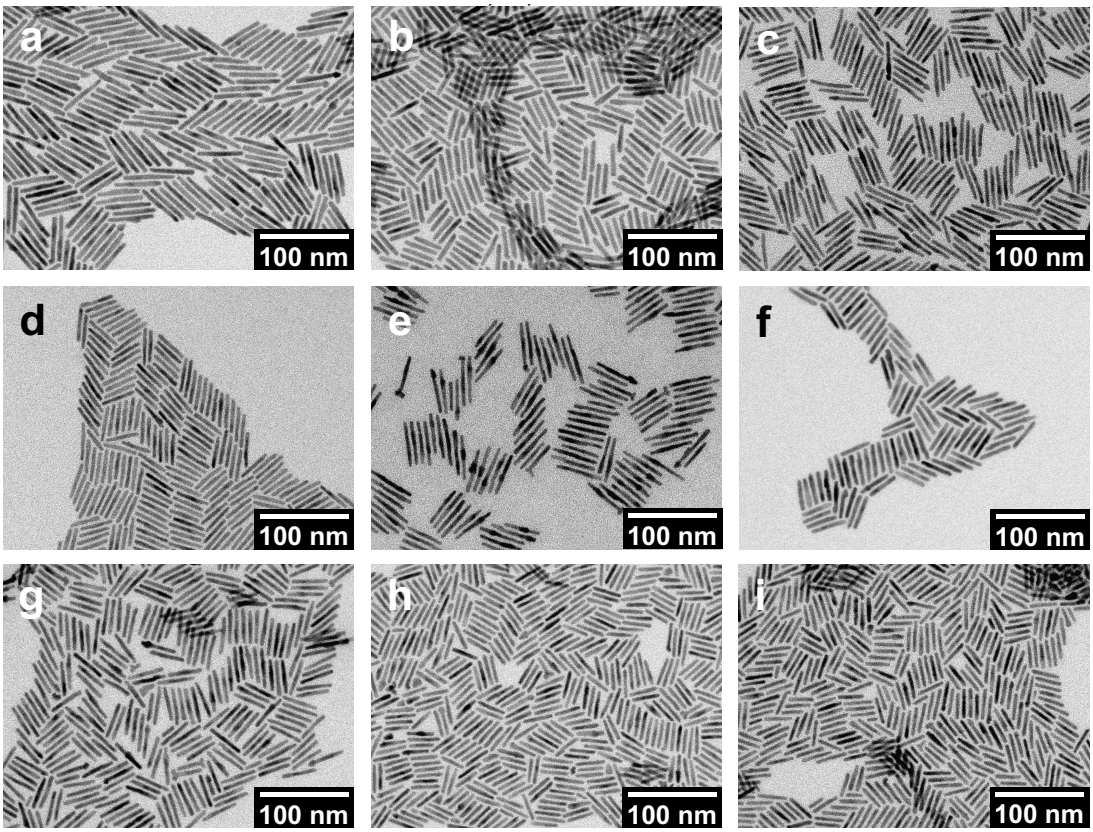

Figure A2: TEM micrographs of the different CdSe/CdS DR batches used in this work. See Table 7.2 (a-e) and Table A1 (f-i) for dimensions of the functional components of the DRs (the order of appearance in the tables and figure are identical).

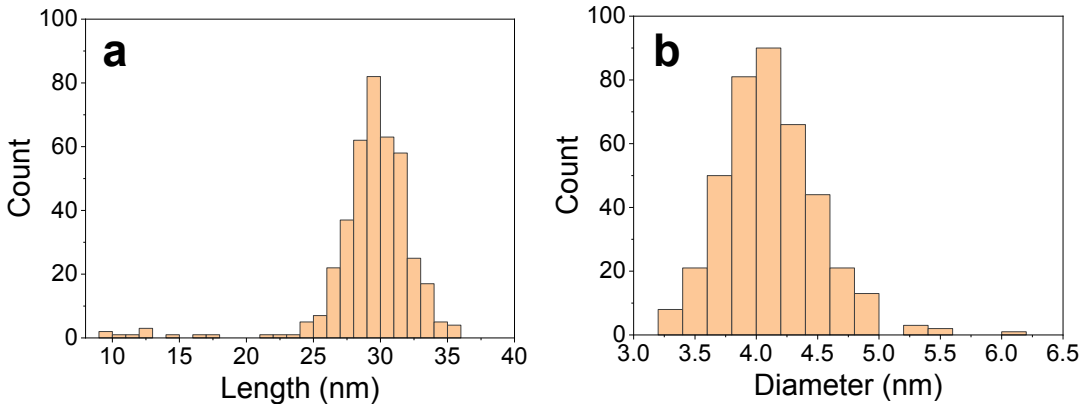

Figure A3: Histogram of the determined lengths and diameters of a batch of CdSe/CdS DRs. An average length of 29.3 ± 3.4 and diameter of 4.1 ± 0.4 was calculated (*cf.* Table A1 and Figure A2h).

A1.3 Calculation of the Dot-in-Rod Concentration

The concentration of DRs was determined from the absorbance spectrum, based on the calculations from Dorfs *et al.* (*cf.* Section 6.8).[150] Based on the DRs dimensions ($l = 36.7\,\mathrm{nm}$, $d = 4.2\,\mathrm{nm}$) the volume of an individual DR was determined

$$V = (d/2)^2 \cdot \pi \cdot l = 508\,\mathrm{nm}^3$$

and the molar extinction coefficient at 350 nm was calculated (*cf.* Equation (6.4))

$$\varepsilon = 28326.9 \cdot 508\,\mathrm{nm}^3 \frac{\mathrm{L}}{\mathrm{mol\,cm\,nm}^3} = 1.44 \cdot 10^7 \frac{\mathrm{L}}{\mathrm{mol\,cm}}.$$

Eventually, the DR concentration was derived from the sample's absorbance at 350 nm ($OD = 1.7$) using the Beer-Lambert law (see Equation (4.18)) while considering the dilution factor of the measurement (in this example: 20 µL of DR suspension in 2.4 mL solvent: $\frac{2400+20}{20} = 121$)

$$c = \frac{1.7 \cdot 121}{1.44 \cdot 10^7 \frac{\mathrm{L}}{\mathrm{mol\,cm}} \cdot 1\,\mathrm{cm}} = 14.3 \frac{\mathrm{nmol}}{\mathrm{mL}}.$$

Due to the PL of the DRs, the OD was determined in a spectrometer with a linear beam path (*cf.* Section 4.6.1 for detailed discussion on differences of OD determined in a spectrometer with a linear beam path or an integrating sphere).
As the OD of the sample above was only measured in a spectrometer with an integrating sphere, the OD that would have been measured in a linear beam path was calculated from the OD measured for a comparable sample (similar DR dimensions and QY_{PL}, labeled by subscript "ref") in both setups:
$OD_{\mathrm{DR_{ref},int}} = 0.0426$, $OD_{\mathrm{DR_{ref},lin}} = 0.690$, $OD_{\mathrm{DR,int}} = 0.118$, $QY_{\mathrm{PL;DR_{ref}}} = 45\,\%$ and $QY_{\mathrm{PL;DR}} = 40\,\%$

$$OD_{\mathrm{DR,lin}} = \frac{OD_{\mathrm{DR_{ref},lin}}}{OD_{\mathrm{DR_{ref},int}}} \cdot OD_{\mathrm{DR,int}} \cdot \frac{QY_{\mathrm{PL;DR}}}{QY_{\mathrm{PL;DR_{ref}}}} = 1.7,$$

with OD_{int} and OD_{lin} as the OD measured in a spectrometer with an integrating sphere and linear beam path, respectively.

A1.4 Pt Growth on CdSe/CdS Dot-in-Rods

Table A2: Volumes of DR suspension, amounts of Pt precursor, and resulting ratios of Pt precursor to DRs added for the precursor amount-dependent hot-injection Pt deposition on CdSe/CdS DRs discussed in Section 7.1.3 and shown in Figure 7.6.

DR Suspension (mL)	Pt Precursor (mg)	Ratio of Pt Precursor to DRs $\left(\frac{\text{mg}}{\text{nmol}}\right)$
0.3	1.44	0.34
2	25	0.88
0.15	2.88	1.3

Table A3: Reaction time-dependent proportion of bare DRs, DRs with a single Pt domain at the DRs' tip, and DRs with multiple Pt domains after Pt deposition using a hot-injection synthesis. Samples were prepared by extracting aliquots from the reaction suspension and the number of Pt domains was determined from TEM micrographs (*cf.* Figure 7.8).

Reaction Time (min)	Bare (%)	Single Tip (%)	Multiple Domains (%)
5	90	10	0
6	69	31	0
9	22	64	14
12	4	47	49

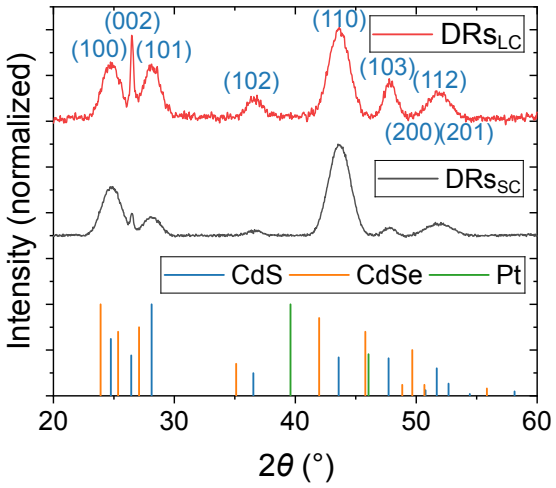

Figure A4: XRD measurement of bare CdSe/CdS DRs of different core sizes (large core (subscript "LC"): 3.1 nm, red line and small core (subscript "SC"): 2.3 nm, black line) and reference diffraction data sets (*cf.* Figure 7.10). Due to the much smaller volume fraction of the CdSe core compared to the CdS shell domain, the former is barely visible in the diffractogram, also for large cores.

A2 Charge-Separated State Feature - Pt-CdSe/CdS Dot-in-Rod Batches

The Pt-CdSe/CdS nanocatalysts used for the CSS feature study in Figure 7.20 and Figure 7.36d had a CdSe seed diameter of 2.3 nm, an average rod length of 36.7 ± 2.7 nm, and a rod diameter of 4.2 ± 0.3 nm. These DR parameters were determined by evaluating ~ 200 NPs in TEM micrographs (*cf.* Figure A2g). After Pt deposition, 71 % of the NPs had a single Pt tip, 20 % had two tips, 9 % had no tip (~ 150 Pt-DRs were evaluated in TEM micrographs - *cf.* Figure A5).

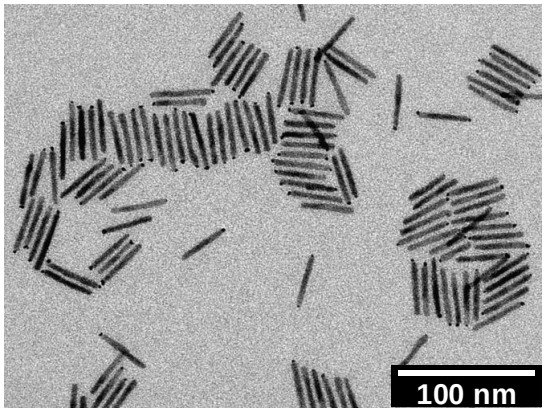

Figure A5: TEM micrograph of Pt-CdSe/CdS DRs used for the CSS measurements in Figure 7.20 and Figure 7.36d.

A3 Fitting Parameters - Transient Absorption and Photoluminescence Kinetics

Table A4: Multiexponential decay fitting parameters for PL decay of bare CdSe/CdS DRs, capped with non-polar, organic ligands in toluene and capped with MUA ligands in water.

Solvent	A_1; τ_1 (ns)	A_2; τ_2 (ns)	A_3; τ_3 (ns)
Toluene	0.895; 48.6	8.08; 15.0	1.73; 5.32
H_2O	1.84; 18.7	3.74; 5.15	37.4; 0.551

Table A5: Multiexponential decay fitting parameters for PL decay of Pt-tipped CdSe/CdS DRs, capped with non-polar, organic ligands in toluene and capped with MUA ligands in water.

Solvent	A_1; τ_1 (ns)	A_2; τ_2 (ns)	A_3; τ_3 (ns)
Toluene	1.46; 23.2	8.29; 8.17	6.63; 1.97
H_2O	2.32; 22.2	4.58; 5.74	9.28; 1.08

Table A6: Multiexponential decay fitting parameters for the PL decay kinetics of bare and Pt-tipped CdSe/CdS DRs with Pt domains of different sizes and numbers, capped with non-polar, organic ligands in toluene.

Sample	A_1; τ_1 (ns)	A_2; τ_2 (ns)	A_3; τ_3 (ns)
DRs	1.67; 39.2	9.8; 14.3	- ; -
Pt-DRs$_{Small}$	4.05; 10.5	4.74; 3.69	3.77; 0.464
Pt-DRs$_{Medium}$	3.97; 4.93	7.08; 1.45	11.9; 0.214
Pt-DRs$_{Large}$	1.63; 2.62	6.6; 0.614	17; 0.127

A4 Determining the Photoluminescence Quantum Yield Relative to Coumarin 153

The QY_{PL} of the bare and Pt-tipped DRs, with Pt domains of different sizes and numbers was calculated relative to coumarin 153. Emission spectra of coumarin 153 in ethanol and of the bare and Pt-tipped DRs, with Pt domains of different sizes and numbers in toluene, were recorded at different integration times and positions of the emission attenuator (EM-attenuator), in order to obtain an adequate signal for all measurements (Figure A6a-e). The attenuation of the emission by the position of the EM-attenuator was calibrated (Figure A6f) for calculating an attenuation factor, which was considered while calculating the integrated emission intensity and QY_{PL} (Table A7, *cf.* Equation (6.5) for formula).

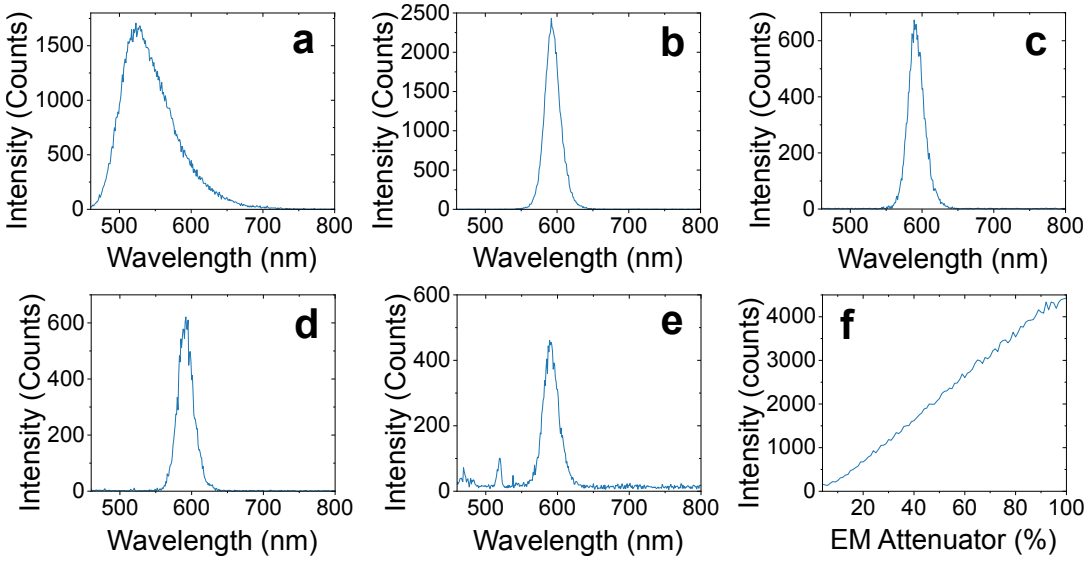

Figure A6: Static PL spectra of coumarin 153 in EtOH (a) and bare CdSe/CdS DRs (b), both at 0.1 s integration time and 10 % position of the EM-attenuator, Pt-tipped DRs, with Pt domains of different sizes and numbers: Pt-DRs$_{Small}$ at 0.1 s integration time and 20 % position of the EM-attenuator (c), Pt-DRs$_{Medium}$ at 0.1 s integration time and 60 % position of the EM-attenuator (d), Pt-DRs$_{Large}$ at 1 s integration time and 100 % position of the EM-attenuator (e), capped with non-polar ligands in toluene, all at 450 nm excitation. Transmitted intensity at different positions of the EM-attenuator at 592 nm excitation (f).

Table A7: Measured *OD*, attenuation factor, integrated emission intensity, refractive index of the solvent,[206] and calculated QY_{PL} for coumarin 153 in ethanol,[153] bare and Pt-tipped CdSe/CdS DRs, with Pt domains of different sizes and numbers, capped with organic, non-polar ligands in toluene. The attenuation factor combines the differences in integration time and position of the EM-attenuator. The integrated emission intensity is calculated from the spectra in Figure A6 and considers the attenuation factor.

Sample	*OD* at 450 nm	Attenuation Factor	Integrated Emission (Counts)	Refractive Index	QY_{PL} (%)
Coumarin 153	0.0941	1	140747	1.361	54.4
DRs	0.104	1	63827	1.494	27.3
Pt-DRs$_{Small}$	0.0939	2.75	6699	1.494	3.12
Pt-DRs$_{Medium}$	0.102	10.6	1590	1.494	0.691
Pt-DRs$_{Large}$	0.101	181	97.3	1.494	0.0425

A5 Influence of the Dimensions of the Functional Components of the Photocatalyst on the Hydrogen Evolution Efficiencies

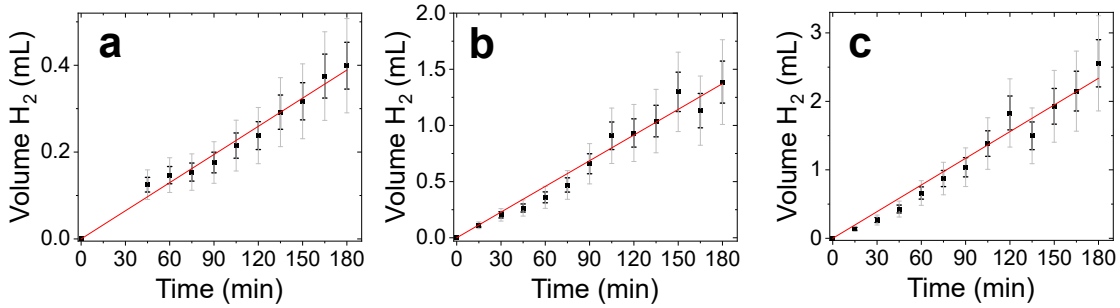

Figure A7: Steady-state hydrogen generation measurements in the cuvette setup on MUA-capped, Pt-tipped CdSe/CdS DRs of different dimensions (see Table 7.7) in water in the presence of IPA. The data was fitted linearly in order to determine a hydrogen production rate for calculating the QE_{H_2}.

A6 EDA-Dependent Steady-State Hydrogen Generation and Spectroscopic Measurements

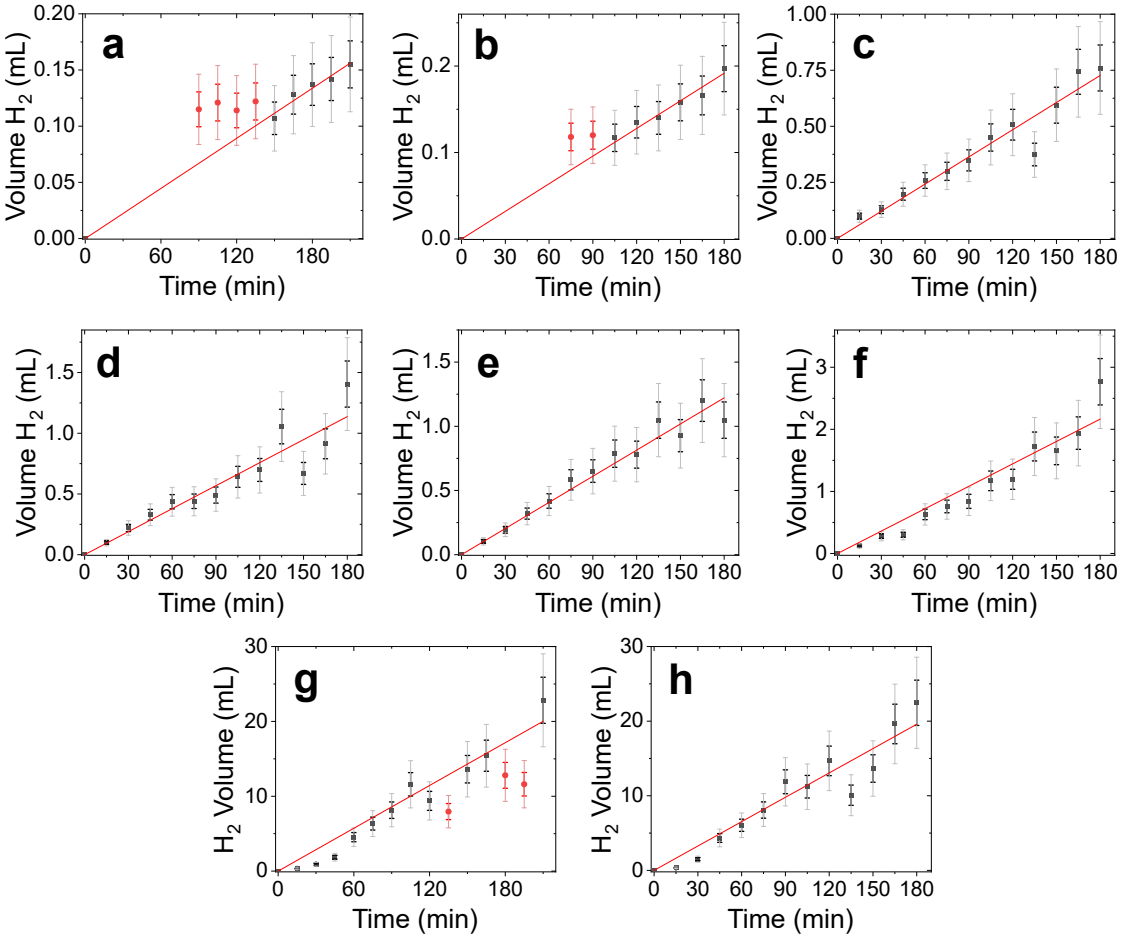

Figure A8: Steady-state hydrogen generation measurements in the cuvette setup on MUA-capped, Pt-tipped CdSe/CdS DRs in water (a) and in the presence of different sacrificial EDAs: MeOH (b), EtOH (c), IPA (d), Na_2SO_3 (e), Na_2S & Na_2SO_3 (f), KOH & IPA (g), KOH & MeOH (h). For the measurement in (a) another batch of Pt-DRs was used (see Section A6.1). The data was fitted linearly in order to determine a hydrogen production rate for calculating the QE_{H_2}. The red data points indicate measurements that were not considered during fitting, as these measurements were distorted by the detection limit of the GC (a+b) or incorrect aliquot extraction (g). The measurement time was increased to 210 min in (a+g) in order to obtain enough measurements for valid fitting.

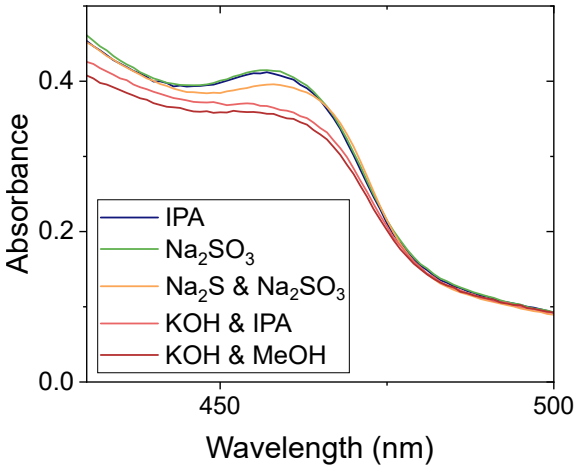

Figure A9: Static absorbance spectra of MUA-capped, Pt-tipped CdSe/CdS DRs in water, in the presence of different EDAs (IPA, Na_2SO_3, Na_2S & Na_2SO_3, KOH & IPA, KOH & MeOH). In the presence of the EDA mixture of Na_2S & Na_2SO_3 and the mixture of KOH & alcohol a bathochromic shift occurs.

A6.1 Alternative Batch of MUA-Capped, Pt-Tipped CdSe/CdS DRs for Steady-State Hydrogen Generation Measurements

For the static UV-vis spectroscopy and steady-state hydrogen production measurements on the Pt-DRs in the absence of any EDA (MUA) in Figure 7.34, an alternative batch of Pt-DRs was used, exhibiting comparable dimensions (2.30 nm core size, 28.9 ± 3.6 nm length, 4.2 ± 0.4 nm diameter), photocatalytic activity (see Figure A10a), as well as static absorbance (Figure A10b+c) to the Pt-DR sample used for the other EDAs in Figure 7.34.

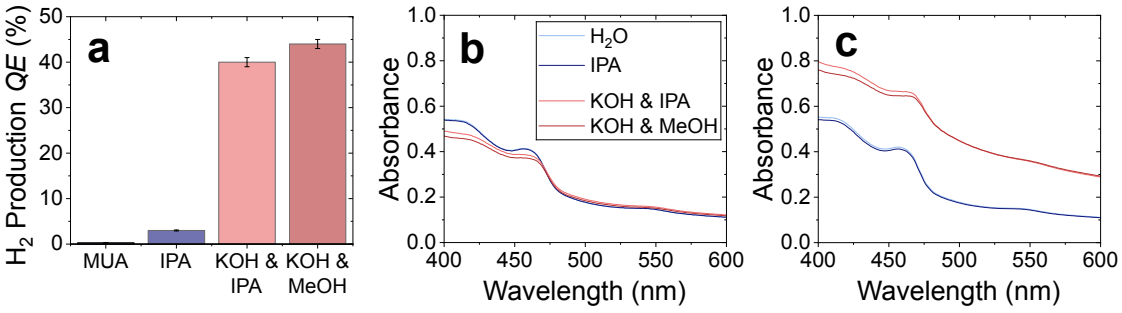

Figure A10: Quantum efficiencies in hydrogen production (a), static absorbance spectra recorded in an integrating sphere (b) and linear beam path (c) for an alternative batch of MUA-capped, Pt-tipped CdSe/CdS DRs in the presence of different EDAs (see color code in (b).

A6.2 Time-Resolved Spectroscopy and Colloidal Stability

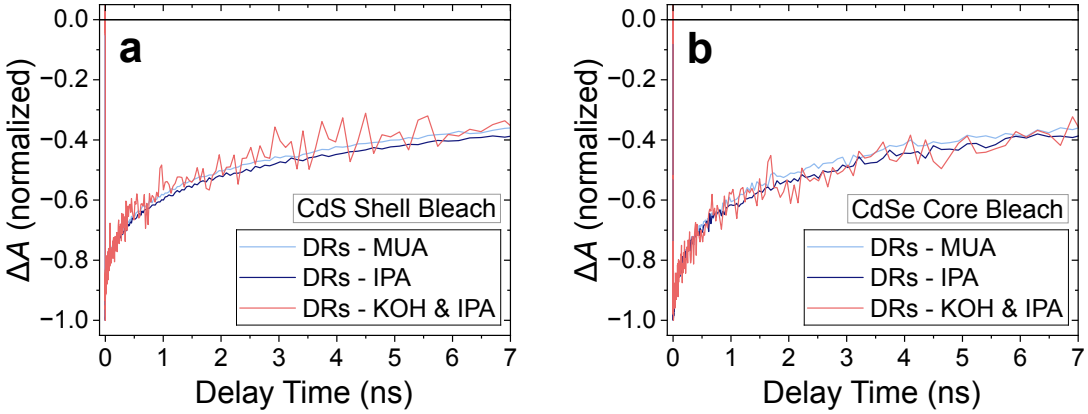

Figure A11: Normalized TA bleach recovery kinetics of bare CdSe/CdS DRs in the presence of IPA, KOH & IPA, and without any sacrificial EDA added (MUA) at the CdS shell (a) and CdSe core (b), at 400 nm excitation. Independent on the choice of EDA, the kinetics are the same. Thus, the observed EDA-dependent changes in decay kinetics for the Pt-tipped DRs (Figure 7.36b+c) apparently result from charge transfer processes in the context of photocatalytic activity of the nanohybrids.

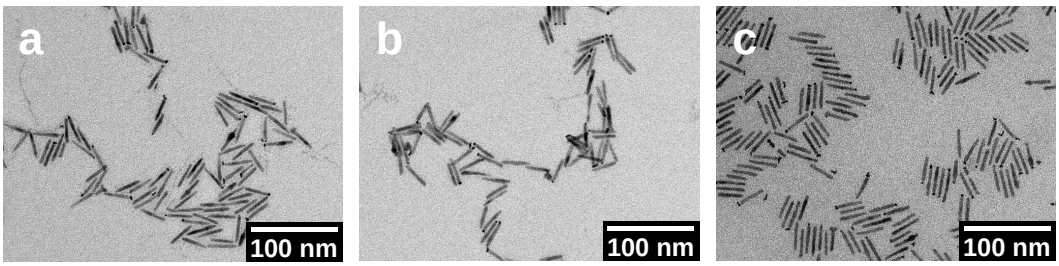

Figure A12: TEM micrographs of MUA-capped, Pt-tipped CdSe/CdS DRs in water (a) and in the presence of EtOH (b) and Na_2SO_3 (c). The DR attach tip-to-tip in water and in the presence of the alcohol, whereas they assemble laterally in the presence of the sulfide.

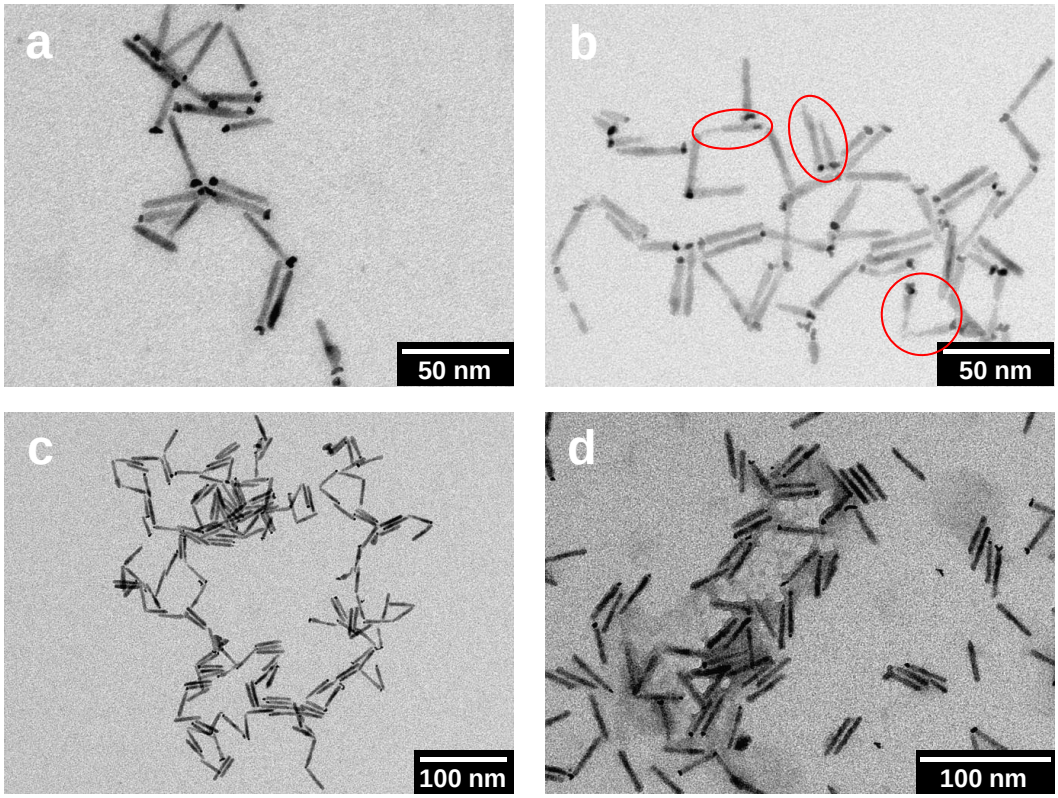

Figure A13: TEM micrographs of MUA-capped, Pt-tipped CdSe/CdS DRs before (a) and after (b) three hours of illumination without any sacrificial EDA added. Due to the absence of a sacrificial EDA, the semiconducting domain was degraded by the photogenerated holes. The red circles mark NPs where this photogenerated degradation is especially apparent. The micrographs in (c+d) show the MUA-capped, Pt-tipped CdSe/CdS DRs from Figure A12b+c in the presence of EtOH and Na_2SO_3, respectively, after three hours of illumination. No degradation of the semiconductor is observable and the NPs kept the tip-to-tip and lateral alignment, respectively.

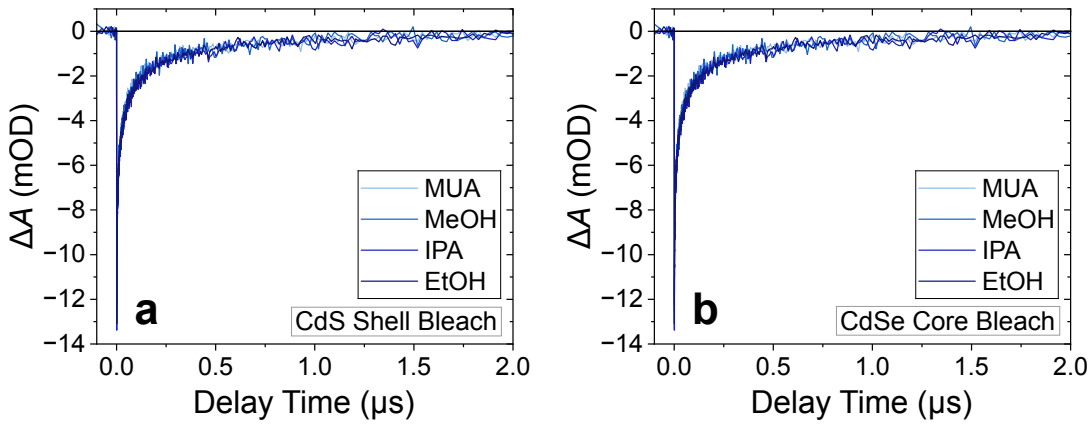

Figure A14: ns-TA bleach decay kinetics of the CdS shell (a) and CdSe core (b) feature of the MUA-capped, Pt-tipped CdSe/CdS DRs in water (MUA) and in the presence of the alcoholic EDAs (MeOH, EtOH, IPA) on long time scales, at 400 nm excitation. The kinetics are not altered by the addition of the alcoholic EDAs.

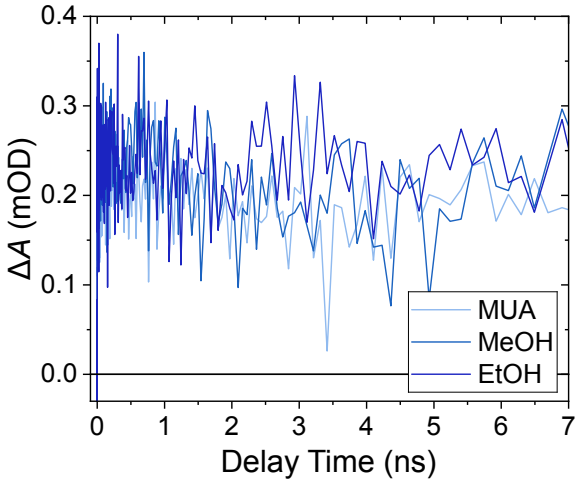

Figure A15: TA decay kinetics of the STH feature, averaged in the probe spectral range from 600 to 700 nm. The measurements were conducted at 400 nm excitation, using MUA-capped, Pt-tipped CdSe/CdS DRs in water (MUA) and in the presence of the alcoholic EDAs MeOH and EtOH, combining fs- and ns-TA measurements. The kinetics without an additional EDA (MUA) and in the presence of MeOH decay similarly, which is in accordance with the photocatalytic activity (*cf.* Figure 7.34). Unexpectedly, the kinetic in the presence of EtOH does not decay significantly faster. This is likely due to the large noise level in this spectral region.

A6.3 Dissociation of Alcoholic EDAs at Large pH

The addition of an acid (HA) to water results in the (partial) dissociation of the acid into two ions.

$$\mathrm{HA} + \mathrm{H_2O} \rightleftharpoons \mathrm{A^-} + \mathrm{H_3O^+}$$

The extent of acid dissociation is dependent on the strength of the acid, which is quantified by the associated acid dissociation constant K_a or the pK_a-value.

$$K_\mathrm{a} = \left(\frac{\left[\mathrm{A^-}\right] \cdot \left[\mathrm{H_3O^+}\right]}{[\mathrm{HA}]} \right) \tag{A.1}$$

$$\mathrm{p}K_\mathrm{a} = -\log\left(K_\mathrm{a} \cdot 1\,\frac{\mathrm{L}}{\mathrm{mol}}\right) = -\log\left(\frac{\left[\mathrm{A^-}\right] \cdot \left[\mathrm{H_3O^+}\right]}{[\mathrm{HA}]} \cdot 1\,\frac{\mathrm{L}}{\mathrm{mol}}\right) \tag{A.2}$$

The higher the K_a, or the lower the pK_a value, the stronger the acid.[207] The degree of dissociation α specifies the proportion of dissociated acid

$$\alpha = \frac{\left[\mathrm{A^-}\right]}{[\mathrm{HA}]_0}, \tag{A.3}$$

with the initial concentration of the non-dissociated acid $[\mathrm{HA}]_0$.[208] With the relation $[\mathrm{HA}]_0 = \left[\mathrm{A^-}\right] + [\mathrm{HA}]$ and Equation (A.1) the degree of dissociation can be expressed as

$$\alpha = \frac{K_\mathrm{a}}{\left[\mathrm{H_3O^+}\right] + K_\mathrm{a}} = \frac{10^{-\mathrm{p}K_\mathrm{a}\,\frac{\mathrm{mol}}{\mathrm{L}}}}{\left[\mathrm{H_3O^+}\right] + 10^{-\mathrm{p}K_\mathrm{a}\,\frac{\mathrm{mol}}{\mathrm{L}}}}. \tag{A.4}$$

Even though MeOH and IPA are weak acids, at pH 14 a fraction of the alcoholic EDAs dissociates, forming the respective alkoxide. In the case of MeOH the following equilibrium results

$$\mathrm{MeOH} + \mathrm{H_2O} \rightleftharpoons \mathrm{MeO^-} + \mathrm{H_3O^+},$$

with $\mathrm{MeO^-}$ as the methoxide anion.
The pK_a value of MeOH is 15.3,[205] and 10 vol% of MeOH were introduced, which corresponds to an initial concentration $[\mathrm{MeOH}]_0$ of 2.48 $\frac{\mathrm{mol}}{\mathrm{L}}$.

$$\alpha_\mathrm{MeOH} = 0.0477$$

$$\left[\mathrm{MeO^-}\right] = \alpha_\mathrm{MeOH} \cdot [\mathrm{MeOH}]_0 = 1.18 \cdot 10^{-1}\,\frac{\mathrm{mol}}{\mathrm{L}}$$

Analogous in the presence of IPA $\left(\mathrm{p}K_\mathrm{a} = 17.1,^{[205]}\,[\mathrm{IPA}] = 1.31\,\frac{\mathrm{mol}}{\mathrm{L}}\right)$:

$$\alpha_\mathrm{IPA} = 7.94 \cdot 10^{-4}$$

$$\left[\mathrm{IPA}^-\right] = 1.04 \cdot 10^{-3}\,\frac{\mathrm{mol}}{\mathrm{L}},$$

with $\left[\mathrm{IPA}^-\right]$ as the concentration of the IPA alkoxide. Thus, at pH 14, the concentration of alkoxides is roughly two orders of magnitude larger in the case of MeOH compared to IPA. Since these alkoxides are highly reductive and should be able to bind to the NPs surface, the QE_{H_2} is larger in the case of the hydroxide & MeOH mixture than in the IPA mixture.

A7 Latency Hydrogen Detection in the Reactor Setup

The experiment displayed in this section was performed by Sebastian Hentschel (*Mews Research Group, Institut für Physikalische Chemie, Universität Hamburg*).

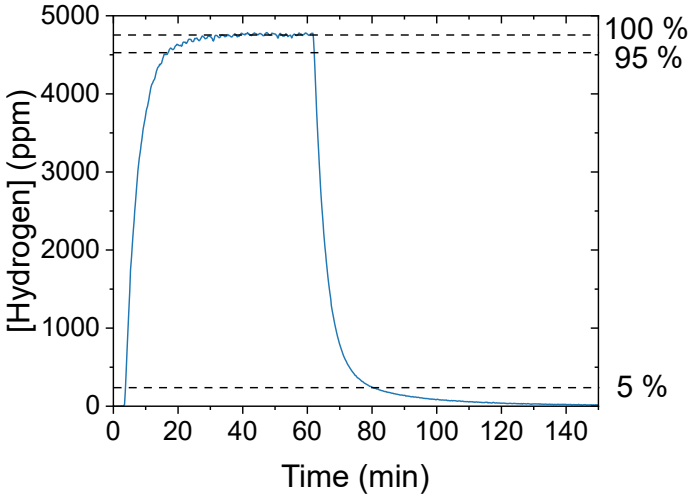

Figure A16: Hydrogen detection measurement in the reactor setup. Hydrogen gas was injected at a rate of 50 µL min^{-1} into the liquid phase inside the reactor. The injection was started at 0 min. After 60 min, the injection was stopped. The dashed lines indicate 100 %, 95 %, and 5 % of the constant value of hydrogen concentration during injection.

The latency between hydrogen production and detection of a constant hydrogen concentration in the reactor setup was characterized by injecting hydrogen gas at a constant rate (50 µL min^{-1}) into the liquid phase (159 mL water) of the reactor setup. The gas was injected from a gastight syringe using a syringe pump. The measured hydrogen concentration stabilizes at a constant value approximately

40 min after starting the hydrogen injection (Figure A16). Roughly 15 min after the start of the hydrogen injection, the measured hydrogen concentration is already at 95 % of this stable value. The injection was stopped 60 min after the start of the hydrogen injection. The hydrogen concentration recovers completely (0 ppm) after another 60 min. Roughly 20 min after stopping the injection, 95 % of the hydrogen concentration recovered.

A8 Illumination Time-Dependent Photocatalytic Activity - Fitting Parameters

Table A8: Multiexponential decay fitting parameters for the PL kinetics of MUA-capped, Pt-tipped CdSe/CdS DRs in water the presence of IPA before and after a hydrogen production measurement (see Figure 7.41e for PL kinetics).

Sample	A_1; τ_1 (ps)	A_2; τ_2 (ps)	A_3; τ_3 (ps)
Before Illumination	1.83; 14.6	4.42; 4.51	17.5; 0.813
After Illumination	1.87; 9.92	5.11; 2.61	6.19; 0.409

A9 Power Density-Dependent Photocatalytic Activity

The non-normalized QE_{H_2} data of the different measurement series in the online reactor and cuvette setup are shown in Figure A17. As discussed above, the hydrogen production rate increases over time. In order to align all production rates regarding their illumination time, the theoretical value after 2 h of illumination was calculated for all measurements in the reactor setup. The hydrogen production rate at 12 mW cm^{-2} after 2 h of illumination was extracted from the measurement. The theoretical production rates after only 2 h of illumination at 9.12 mW cm^{-2} and 6.08 mW cm^{-2}, as well as 22.8 mW cm^{-2} and 44.5 mW cm^{-2} were calculated from the factors by which the production rates varied upon changing of the power densities (*cf.* Figure A19). For each power density, the QE_{H_2} was determined from the calculated production rate and the sample's *OD*, which was determined in a spectrometer with an integrating sphere before the measurement (*cf.* Equation (6.11)). For the cuvette setup, the contribution of the illumination time was considered in the error bar (*cf.* Figure 7.48). The factor by which the hydrogen production rate increases within 2 h of illumination was determined

from the measurement in the reactor setup (Figure A20). Based on this factor, the expected illumination time-dependent increase in the hydrogen production rate was considered in the negative error. For the measurement in the cuvette setup at 4.21 mW cm^{-2}, which was measured after 2 h of illumination at a smaller and larger power density, respectively (*cf.* Figure 7.46), the average value was calculated. The power densities were calibrated using a water-filled reactor or cuvette, respectively.

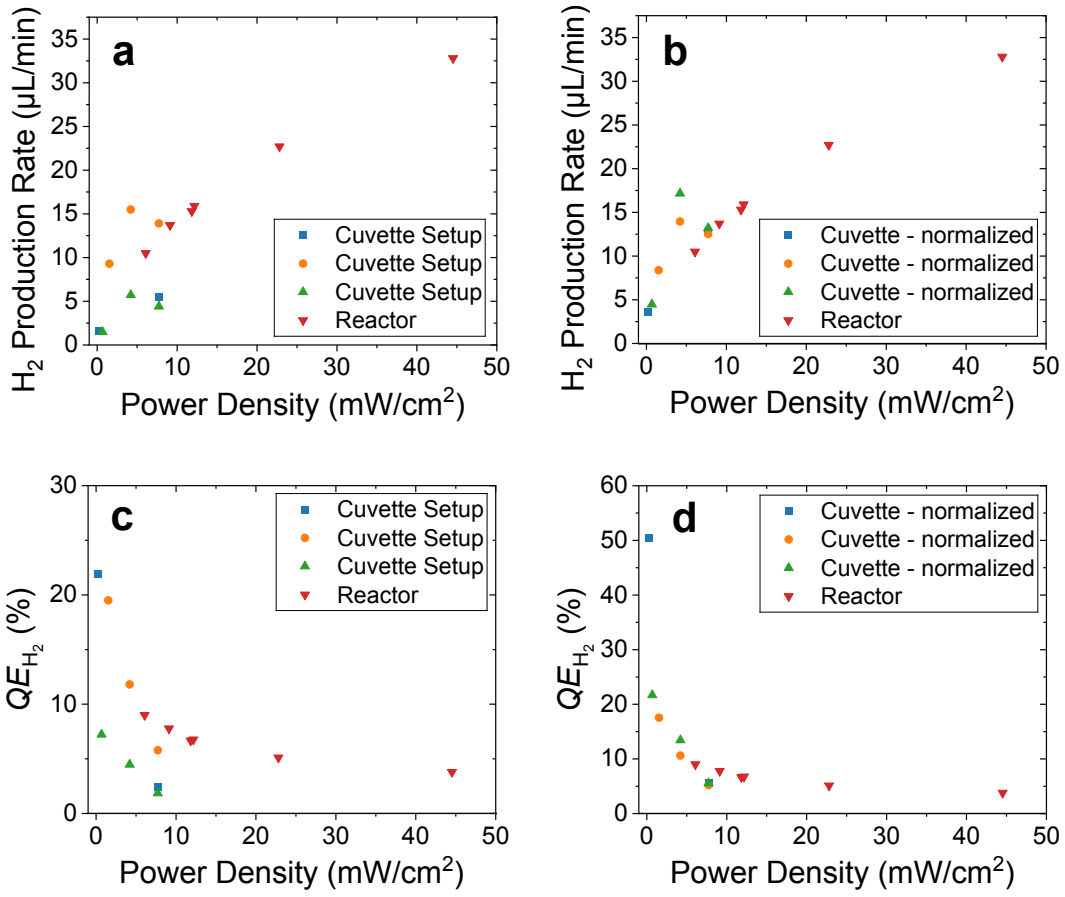

Figure A17: Non-normalized (a+c) and normalized (b+d) power density-dependent hydrogen production rates (a+b) and quantum efficiencies in hydrogen production (c+d), after 2 h of illumination, determined by conducting steady-state hydrogen production measurements on MUA-capped, Pt-tipped CdSe/CdS DRs in the presence of IPA, combining different measurement series in the online reactor and cuvette setup (see color code). In (b+d) the values in the cuvette setup were normalized to the calculated values in the reactor setup between ∼ 6 and 9 mW cm^{-2}.

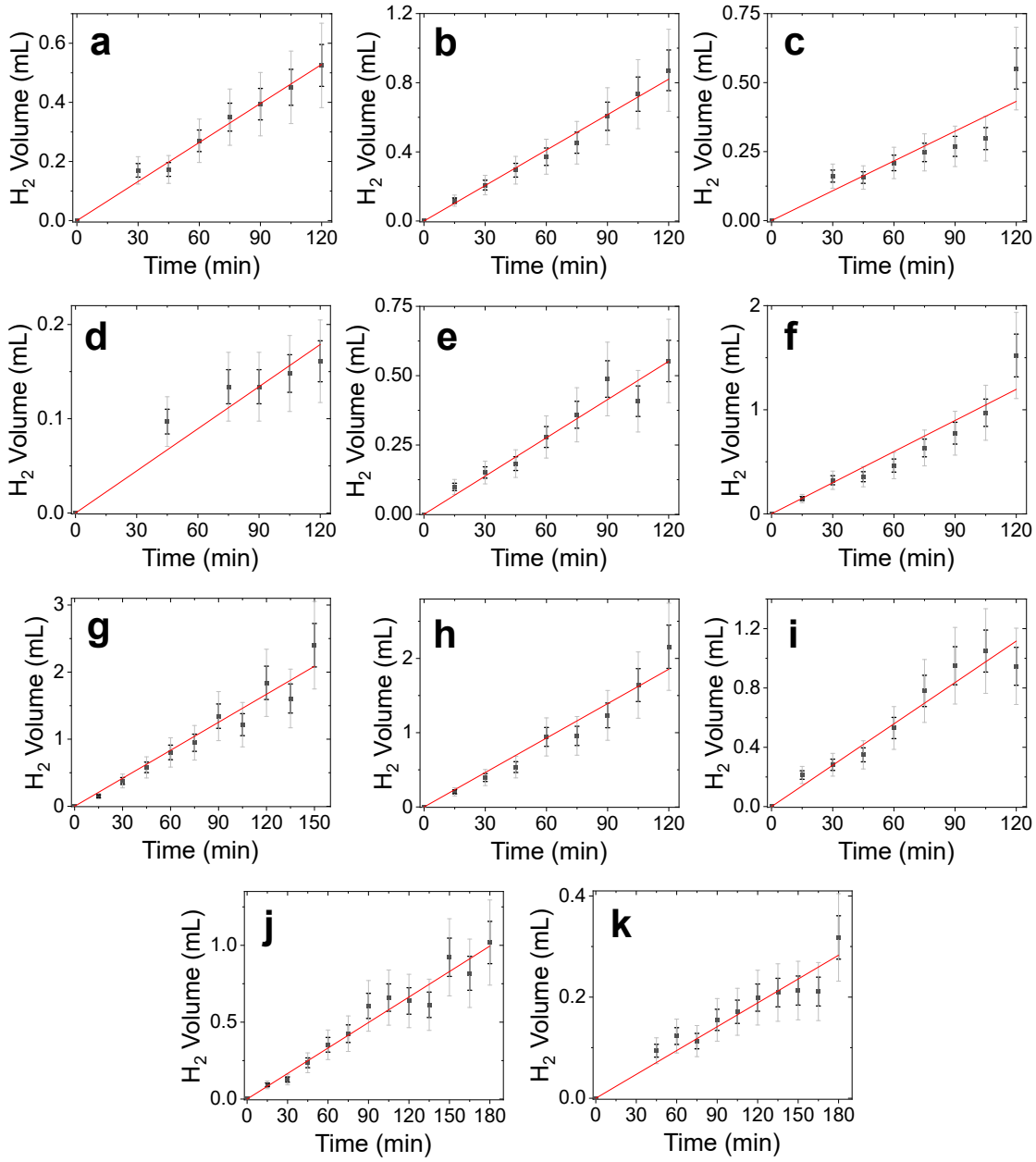

Figure A18: Steady-state hydrogen generation measurements in the cuvette setup on MUA-capped, Pt-tipped CdSe/CdS DRs in water in the presence of IPA at different excitation power densities (7.72 mW cm^{-2} (a+f+g+j), 4.21 mW cm^{-2} (b+e+h), 1.53 mW cm^{-2} (i), 0.690 mW cm^{-2} (c+d), 0.241 mW cm^{-2} (k)). The data was fitted linearly in order to determine a hydrogen production rate for calculating the QE_{H_2} (see Figure A17).

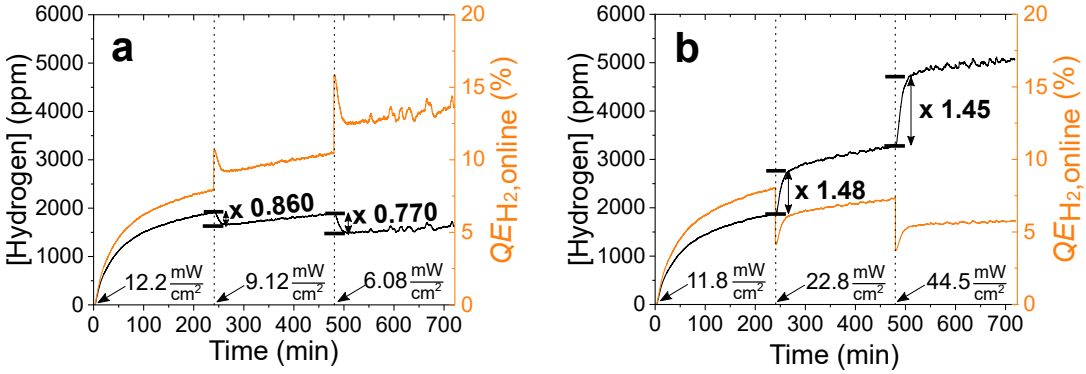

Figure A19: Factors by which the hydrogen production rates decreased and increased, respectively, upon reducing (a) and increasing (b) the power density in the power-dependent measurement in the reactor setup (see Figure 7.47 for details on measurement). The factors were calculated from the hydrogen production rates before and after change of the power density. The production rate after the change of the power density was extrapolated from the linearly increasing rate for >45 min after the change in power density.

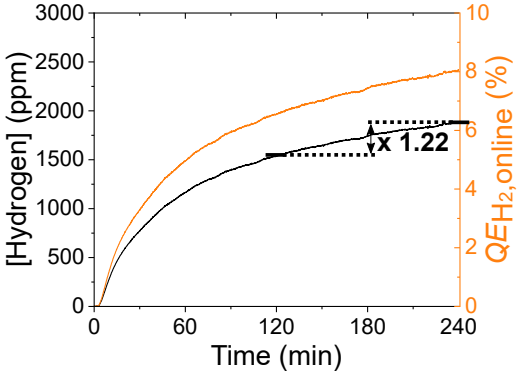

Figure A20: Calculation of the factor by which the hydrogen production rate increases within 2 h of illumination in the reactor setup (see Figure 7.47 for details on measurement). The factor was calculated from the hydrogen production rates at 120 min and 240 min of illumination time.

A10 Calculation - Absorbed Photons per Time per Nanoparticle

Experimental parameters: $H_{\mathrm{Exc}} = 0.241\,\mathrm{mW\,cm^{-2}}$, A = 14.5 cm^2, OD = 0.74, n_{NPs} = 2.5 nmol
Fraction of absorbed light Abs (see Equation (4.19))

$$Abs = 1 - 10^{-0.74} = 0.82.$$

Absorbed power density H_{Abs}

$$P_{\mathrm{Abs}} = 0.82 \cdot 0.241\,\frac{\mathrm{mW}}{\mathrm{cm^2}} = 0.20\,\frac{\mathrm{mW}}{\mathrm{cm^2}}.$$

Number of absorbed photons per time $\frac{N_{\mathrm{Photons}}}{t}$ (*cf.* Equation (6.8) and Equation (6.9))

$$\frac{N_{\mathrm{Photons}}}{t} = \frac{H_{\mathrm{Abs}} \cdot \lambda \cdot A}{h \cdot c} = 6.5 \cdot 10^{15}\,\frac{\mathrm{Photons}}{\mathrm{s}}.$$

Total number of NPs $\#_{\mathrm{NPs}}$

$$\#_{\mathrm{NPs}} = n_{\mathrm{NPs}} \cdot N_{\mathrm{A}} = 1.5 \cdot 10^{15}.$$

Number of photons absorbed by each NP per time

$$\frac{\frac{N_{\mathrm{Photons}}}{t}}{\#_{\mathrm{NPs}}} = 4.3\frac{\mathrm{Photons}}{\mathrm{s}}.$$

At an excitation power density of $\sim 0.24\,\mathrm{mW\,cm^{-2}}$ (excitation power of 3.5 mW), each NP absorbs an average of four photons per second. Analogously, at a power density of $\sim 7.9\,\mathrm{mW\,cm^{-2}}$ (115 mW), each NP absorbs approximately 140 photons per second, which corresponds to one photon absorption per NP every 7 ms.

B Safety

Table B1 lists the chemicals employed in this study including their classification according to the Globally Harmonized System of Classification and Labelling of Chemicals (GHS), as well as hazardous and precautionary statements. Table B2 lists all utilized substances classified as carcinogenic, mutagenic, or reprotoxic (CMR) by the Regulation "for Classification, Labeling and Packing" (CLP Regulation) by the *European Union* ((EG) 1272/2008).

Table B1: Used chemicals with respective GHS symbols, hazardous and precautionary statements (see Figure B1 for pictograms of GHS symbols). Safety information obtained from *Merck* safety data sheets.[209]

Substance	CAS-Number	GHS Symbol	Hazardous Statements	Precautionary Statements
Acetone	67-64-1	02, 07	225, 319, 336	210, 233, 240, 241, 242, 305+351+338
Argon	7440-37-1	04	280	410+403
Cadmium oxide	1306-19-0	06, 08, 09	330, 341, 350, 361fd, 372, 410	202, 260, 264, 271, 273, 304+340+310
Chloroform	67-66-3	06, 08	302, 315, 319, 331, 336, 351, 361d, 372, 412	201, 273, 301+312+330, 302+352, 304+340+311, 308+313
Coumarin 153	53518-18-6	-	-	-

Substance	CAS-Number	GHS Symbol	Hazardous Statements	Precautionary Statements
(1,5-Cyclooctadiene)-dimethylplatinum(II)	12266-92-1	07	315, 319, 335	261, 264, 271, 280, 302+352, 305+351+338
1,2-Dichlorobenzene	95-50-1	07, 09	302, 332, 315, 317, 319, 335, 410	273, 280, 301+312, 302+352, 304+340+312, 305+351+338
Diphenyl ether	101-84-8	07, 09	319, 410	264, 273, 280, 305+351+338, 337+313, 391
Ethanol	64-17-5	02, 07	225, 319	210, 233, 240, 241, 242, 305+351+338
1,2-Hexadecanediol	6920-24-7	-	-	-
n-Hexylphosphonic acid	4721-24-8	07	315, 319	264, 280, 302+352, 305+351+338, 332+313, 337+313
Hydrogen	1333-74-0	02, 04	220, 280	210, 377, 381, 410+403
Isopropyl alcohol	67-63-0	02, 07	225, 319, 336	210, 233, 240, 241, 242, 305+351+338
11-Mercaptoundecanoic acid	71310-21-9	07	315, 319, 335	261, 264, 271, 280, 302+352, 305+351+338
Methanol	67-56-1	02, 06, 08	225, 301+311+331, 370	210, 233, 280, 301+ 310, 303+361+353, 304+340+311
Nitrogen	7727-37-9	04	280	410+403

Substance	CAS-Number	GHS Symbol	Hazardous Statements	Precautionary Statements
Nonanoic acid	112-05-0	07	315, 319	264, 280, 302+352, 305+351+338, 332+313, 337+313
n-Octadecylphosphonic acid	4724-47-4	07	315, 319	264, 280, 302+352, 305+351+338, 332+313, 337+313
n-Octylamine	111-86-4	02, 05, 06, 09	226, 301+311, 314, 332, 335, 410	210, 273, 280, 303+361+353, 304+340+310, 305+351+338
Oleic acid	112-80-1	-	-	-
Oleylamine	112-90-3	05, 07, 08, 09	302, 304, 314, 335, 373, 410	273, 280, 301+330+331, 303+361+353, 304+340+310, 305+351+338
Platinum(II) acetylacetonate	15170-57-7	07, 08	302+312+332, 315, 319, 335, 361	280, 301+312, 302+352+312, 304+340+312, 305+351+338, 308+313
Potassium hydroxide	1310-58-3	05, 07	290, 302, 314	234, 260, 280, 301+312, 303+361+353, 305+351+338
Selenium	7782-49-2	06, 08	301+331, 373, 413	260, 264, 273, 301+310, 304+340+311, 314

Substance	CAS-Number	GHS Symbol	Hazardous Statements	Precautionary Statements
Sodium sulfide	1313-82-2	02, 05, 06, 09	251, 290, 301+311, 314, 400	235, 260, 280, 303+361+353, 304+340+310, 305+351+338
Sodium sulfite	7757-83-7	-	-	-
Sulfur	7704-34-9	07	315	264, 280, 302+352, 332+313, 362+P364
Toluene	108-88-3	02, 07, 08	225, 304, 315, 336, 361d, 373, 412	202, 210, 273, 301+310, 303+361+353, 331
Triethylamine	121-44-8	02, 05, 06	225, 302, 311+331, 314, 335	210, 280, 301+312, 303+361+353, 304+340+310, 305+351+338
Trioctylphosphine	4731-53-7	05	314	280, 303+361+353, 304+340+310, 305+351+338, 363, 405
Trioctylphosphine oxide	78-50-2	05	315, 318, 412	264, 273, 280, 302+352, 305+351+338, 332+313

Table B2: Employed CMR substances, used amounts, and classification by the CLP Regulation. The substances are classified as carcinogenic (C), mutagenic (M), harmful to the development of the unborn child (R_D), and harmful to fertility (R_F). Safety information obtained from the list of CMR substances by the "*Deutsche Gesetzliche Unfallversicherung*".[210]

Substance	CAS-Number	Amount Used	C	M	R_D	R_F
Cadmium oxide	1306-19-0	10 g	1B	2	2	2
Cadmium sulfide	1306-23-6	10 g	1B	2	2	2
Chloroform	67-66-3	5 L	2		2	
Toluene	108-88-3	20 L			2	

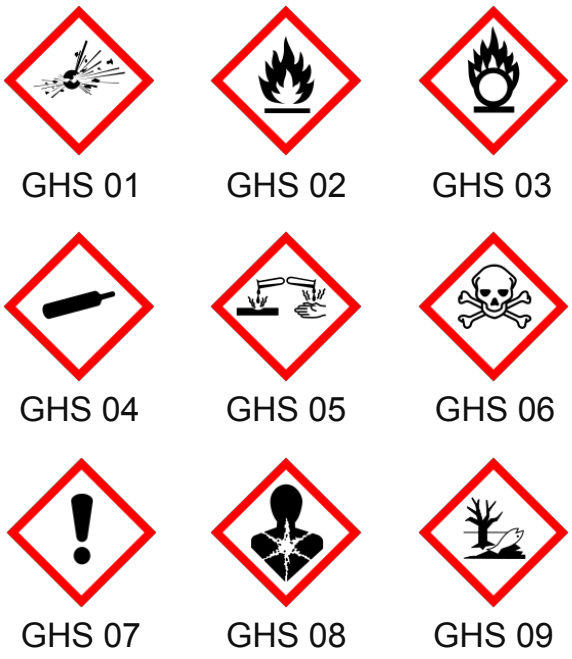

Figure B1: GHS hazard pictograms.

C Danksagung

An erster Stelle möchte ich Prof. Dr. Horst Weller für die Aufnahme in seine Arbeitsgruppe und die großartige Betreuung während meines Promotionsprojekts danken. Vielen Dank für das entgegengebrachte Vertrauen, die freundliche Unterstützung und die wertvollen wissenschaftlichen Diskussionen.
Bei Prof. Dr. Alf Mews möchte ich mich für die Übernahme des Zweitgutachtens bedanken.
Weiterhin möchte ich mich bei Yannic U. Stächelin für die produktive, kreative und freundschaftliche Zusammenarbeit an mehreren Kollaborationsprojekten, sowie für die Durchführung der zahlreichen TA Messungen bedanken. In diesem Zusammenhang möchte ich auch Prof. Dr. Holger Lange für die hilfreichen wissenschaftlichen Diskussionen und die Unterstützung bei der Veröffentlichung der Ergebnisse danken.
Mein Dank gilt außerdem Sebastian Hentschel für die Durchführung der Photokatalyse-Messungen in seinem Reaktoraufbau und die produktive Zusammenarbeit bei der Installation unserer Aufbauten.
Des Weiteren bedanke ich mich beim Graduiertenkolleg (GrK) NANOHYBRID für die finanzielle Unterstützung meiner Arbeit, Dienstreisen und Weiterbildungen, sowie bei allen Mitgliedern des GrKs für die zahlreichen spannenden Workshops, Meetings und Kollaborationen. Insbesondere möchte ich Prof. Dr. Carmen Herrmann und Dr. Tobias Vossmeyer für die Co-Betreuung meines Promotionsprojekts im Kontext des GrKs, ihre Unterstützung und hilfreichen Anregungen danken.
Außerdem möchte ich mich bei meiner Masterstudentin Julia A. Voss und bei meiner Bachelorstudentin Benedetta S. Feltrin für ihre tatkräftige und hilfreiche Arbeit im Labor bedanken.
Vielen Dank an Stefan Werner, Andrea Köppen, Ulf König, Robert Schön und Nina Schober für die Anfertigung diverser elektronenmikroskopischer Aufnahmen und Röntgendiffraktogramme.
Mein Dank gilt auch der Forschungswerkstatt der Physikalischen Chemie für die Anfertigung der Schutzkästen für den Photodepositions- und Photokatalyse-Aufbau.

Für die Durchsicht dieser Arbeit danke ich Yannic U. Stächelin, Julia I. M. Funk, Lea R. Klauke und Dr. Sebastian Graf.
Marion Manin, Corinna Flügge und Andreas Kolditz danke ich für ihre kompetente Hilfe bei organisatorischen Belangen.
Herzlich bedanken möchte ich mich außerdem bei meinen Labor- und Bürokollegen Lea, Artur, Sebastian G., Sebastian W., Finn, Julia, Felix, Elena, Agnes, Jil, Marius, Michael, Pia und Larissa mit deren Humor und Hilfsbereitschaft die Arbeit zum Vergnügen wurde. Außerdem möchte ich mich bei allen weiteren aktuellen und ehemaligen Mitgliedern des Arbeitskreises Bendix, Hauke Ha., Hauke He., Jana, Sophia, Nancy, Ahir, Christoph, Ole, Jan-Niklas, Hendrik, Svenja, Kathrin, Gregor, Maik, Clemens, Steffen, Marcus, Julian, Roger für die schöne und unterhaltsame Zeit bedanken.
Schließlich möchte ich mich ganz besonders bei meiner Mutter Waltraud und meiner Schwester Heddy, sowie meinem Vater Heiko, der unglaublich stolz gewesen wäre, für ihre unerschütterliche und liebevolle Unterstützung bedanken.
Besonderer Dank gilt außerdem meiner Freundin Steffi, die mit Liebe und Verständnis viel positive Energie in mein Leben bringt und mich motiviert, das Beste aus mir herauszuholen.

D Eidesstattliche Versicherung

Hiermit versichere ich an Eides statt, die vorliegende Dissertationsschrift selbst verfasst und keine anderen als die angegebenen Quellen und Hilfsmittel benutzt zu haben. Sofern im Zuge der Erstellung der vorliegenden Dissertationsschrift generative Künstliche Intelligenz (gKI) basierte elektronische Hilfsmittel verwendet wurden, versichere ich, dass meine eigene Leistung im Vordergrund stand und dass eine vollständige Dokumentation aller verwendeten Hilfsmittel gemäß der Guten wissenschaftlichen Praxis vorliegt. Ich trage die Verantwortung für eventuell durch die gKI generierte fehlerhafte oder verzerrte Inhalte, fehlerhafte Referenzen, Verstöße gegen das Datenschutz- und Urheberrecht oder Plagiate.

Hamburg, den 30.01.2025

Sönke Wengler-Rust